STRAIN EFFECTS ON ION CONDUCTION IN HETEROGENEOUS OXIDE ELECTROLYTES

by

Weida Shen

A dissertation submitted to the Faculty of the University of Delaware in partial fulfillment of the requirements for the degree of Doctor of Philosophy in Mechanical Engineering

Summer 2014

© 2014 Weida Shen
All Rights Reserved

UMI Number: 3642358

All rights reserved

INFORMATION TO ALL USERS
The quality of this reproduction is dependent upon the quality of the copy submitted.

In the unlikely event that the author did not send a complete manuscript
and there are missing pages, these will be noted. Also, if material had to be removed,
a note will indicate the deletion.

UMI 3642358

Published by ProQuest LLC (2014). Copyright in the Dissertation held by the Author.

Microform Edition © ProQuest LLC.
All rights reserved. This work is protected against
unauthorized copying under Title 17, United States Code

ProQuest LLC.
789 East Eisenhower Parkway
P.O. Box 1346
Ann Arbor, MI 48106 - 1346

STRAIN EFFECTS ON ION CONDUCTION IN HETEROGENEOUS OXIDE ELECTROLYTES

by

Weida Shen

Approved: _____
Suresh G. Advani, Ph.D.
Chair of the Department of Mechanical Engineering

Approved: _____
Babatunde A. Ogunnaike, Ph.D.
Dean of the College of Engineering

Approved: _____
James G. Richards, Ph.D.
Vice Provost for Graduate and Professional Education

I certify that I have read this dissertation and that in my opinion it meets the academic and professional standard required by the University as a dissertation for the degree of Doctor of Philosophy.

Signed: _____

Joshua L. Hertz, Ph.D.
Professor in charge of dissertation

I certify that I have read this dissertation and that in my opinion it meets the academic and professional standard required by the University as a dissertation for the degree of Doctor of Philosophy.

Signed: _____

Chaoying Ni, Ph.D.
Member of dissertation committee

I certify that I have read this dissertation and that in my opinion it meets the academic and professional standard required by the University as a dissertation for the degree of Doctor of Philosophy.

Signed: _____

Ajay K. Prasad, Ph.D.
Member of dissertation committee

I certify that I have read this dissertation and that in my opinion it meets the academic and professional standard required by the University as a dissertation for the degree of Doctor of Philosophy.

Signed: _____

Bingqing Wei, Ph.D.
Member of dissertation committee

ACKNOWLEDGMENTS

Time is flying. This is my third degree and I am quite sure that this will also probably be the last one in my whole life. First of all, I would like to thank my advisor Dr. Joshua Hertz for his guidance in my research. He is very positive, which has influenced me a lot. He always encourages me to be unafraid of working in a new and unfamiliar area. Moreover, he is always willing to discuss problems with me in patience.

I thankfully acknowledge my dissertation committee members, Dr. Chaoying Ni, Dr. Ajay Prasad, and Dr. Bingqing Wei for their time to review my dissertation and for their helpful suggestions given during my proposal defense.

I also would like to thank Jun Jiang for his help in the experiments. I thank Ning Ye for his great suggestions when I faced problems. I also would like to thank Philip Zandona for his help to teach me the use of the sputtering machine.

I also want to thank my colleagues, officemates and friends who gave me help and supports during my Ph.D. study: Eric Fischer, Benjamin McNealy, Harmandeep Khare, Jiaxin Ye, Zeyuan Cao, Andrew Baker, James White, Edward Bonnevie, Bo Lu, Yang Yu, Xiaochao Hu, Dong Wang, Guoliang Ding, Di Xu, Yingzhen Liang, Nan Zhou, Huarong Shen, Conglian Shen and Yifei Luo.

Lastly, I want to really thank my parents for their supports and love. I am sorry that I am so far from them. I also would like to thank my uncles, unties, and cousins for their encouragement.

TABLE OF CONTENTS

LIST OF TABLES vii
LIST OF FIGURES viii
ABSTRACT xiv

Chapter

1 INTRODUCTION 1

1.1 Motivation 1
1.2 Solid Oxide Fuel Cells 4
1.3 Technical Challenges of Solid Oxide Fuel Cells 7
1.4 Solid Oxide Ion Electrolytes 7
1.5 Nanometric Multilayers for Solid Electrolytes 13

1.5.1 Space Charge Effects on Ionic Conduction 14
1.5.2 Interfacial Strain Effects on Ionic Conduction 15

1.5.2.1 Multilayers Composed of Two Doped Conductors 15
1.5.2.2 Multilayers Composed of One Doped Conductor and One Insulator 17

1.6 Conclusions of Literature Review 23
1.7 Objectives of the Research 25

2 EXPERIMENTAL 29

2.1 Film Deposition 29
2.2 Structural and Chemical Characterization 34

2.2.1 X-ray Photoelectron Spectroscopy 34
2.2.2 Energy Dispersive X-Ray Spectrometry 34
2.2.3 Secondary Ion Mass Spectrometry 35
2.2.4 X-ray Diffraction 35
2.2.5 Transmission Electron Microscopy 35

2.3 Microscale Electrode Fabrication 36
2.4 Electrochemical Characterization 38

3 RESULTS 42

3.1 Structure Characterization of CeO_2-ZrO_2 Solid Solutions 42
3.2 Compressive Strain Effect on Oxygen Ion Conduction in CeO_2 44
3.3 Tensile Strain Effect on Oxygen Ion Conduction in ZrO_2 51
3.4 Heterogeneously Doped CeO_2 Thin Films 60
3.5 Beneficial Lattice Strain in Heterogeneously Doped CeO_2 Thin Films .. 72

4 DISCUSSION 80

4.1 Strain Effects on Oxygen Ion Conduction in Fluorite Materials 80
4.2 Space Charge Effects on Oxygen Ion Conduction in Fluorite Materials 90

4.2.1 Gouy-Chapman Model for Space Charge Distribution 91
4.2.2 Effects of Lattice Strain on Space Charge Distribution 99

5 CONCLUSIONS 106

5.1 Summary 106
5.2 Recommendations for Future Work 109

REFERENCES 112

Appendix

REPRINT PERMISSION LETTERS 120

LIST OF TABLES

Table 1 Comparison of five different types of fuel cell technologies [16, 18, 19] 4

Table 2 Configuration of the samples within each of the three sets of YDC/CZO multilayers. 46

Table 3 Configuration of the samples within each of the three sets of multilayers 52

Table 4 Configuration of four samples with net composition of $Ce_{0.95}Y_{0.05}O_{2-\delta}$. Other than the homogeneous sample A, each film consists of 10 repeated bilayers of the Y-containing layer and pure CeO_2 layer. 64

Table 5 Configuration of three different sets of heterogeneously doped CeO_2 films composed of alternating layers of RE_2O_3 and CeO_2. The total film thickness was maintained at $\approx$ 200 nm. 73

LIST OF FIGURES

Figure 1 The US energy consumption by fuel sources predicted through 2040. Reprinted from Ref. [13]. 3

Figure 2 Schematic structure of a SOFC with hydrogen used as the fuel. 6

Figure 3 Ionic conductivity of $(ZrO_2)_{1-x}(Ln_2O_3)_x$ as a function of dopant concentration at temperature of 1000 °C. "Ln" denotes the different dopant oxides. Reprinted from Ref. [32]. 11

Figure 4 Ionic conductivities of several typical oxide ion conductors as a function of the temperature. Reprinted from Ref. [42]. 13

Figure 5 The ionic conductivity of the multilayered films consisting of alternating layers of undoped BaF_2 and CaF_2 on Al_2O_3 substrates. Reprinted from Ref. [51] and [52]. 14

Figure 6 Transmission electron micrograph of CeO_2/ZrO_2 multilayer with constant dopant concentration. Reprinted from Ref. [54]. 15

Figure 7 Three different types of interfacial structures changed with the lattice mismatch. Reprinted from Ref. [57]. 17

Figure 8 Coherent-interface structure of a multilayer composed of two different materials. Reprinted and revised from Ref. [57]. 18

Figure 9 Logarithm of the maximum change of the total conductivity relative to the bulk conductivity as a function of the lattice mismatch. Reprinted from Ref. [60]. 20

Figure 10 The relative enhancement of the oxygen ion diffusivity in YSZ as a function of the tensile strain at four different temperatures. D_O^0 represents the oxygen ion diffusivity of YSZ at 400 K with zero strain. Reprinted from Ref. [61]. 22

Figure 11 The three different film structures with composition $Ce_{1-x-z}Zr_xD_zO_{2-z/2}$ surveyed by using the thin film deposition technique developed recently. (a) Thin films of $Zr_{1-z}Y_zO_{2-z/2}$ (YSZ) or $Ce_{1-z}Gd_zO_{2-z/2}$ (GDC) with heterogeneity at the film substrate and film-air interfaces, studied using different film thickness. (b) Multilayers of $Ce_{1-x}Zr_xO_2$ with either $Zr_{1-z}Y_zO_{2-z/2}$ (YSZ) or $Ce_{1-z}Y_zO_{2-z/2}$ (YDC), creating interfacial lattice mismatch strain that was adjusted by changing the component layer thickness and the Ce/Zr ratio in the $Ce_{1-x}Zr_xO_2$ layers. (c) $Ce_{1-z}Y_zO_{2-z/2}$ (YDC) thin films with dopants distributed either homogeneously or with nanometer-scale modulation of dopant distribution. At the limit, the modulated films consisted of alternating layers of pure Y_2O_3 and CeO_2. Dopant oxides, Gd_2O_3 and La_2O_3, were also studied. 26

Figure 12 A schematic structure of the sputtering machine. 29

Figure 13 Deposition rates of (a) ZrO_2, (b) CeO_2, (c) Y_2O_3, and (d) Gd_2O_3 thin films as a function of the sputtering power. Reprinted from Ref. [71]. .. 31

Figure 14 The relationship between the expected atomic ratio and the actual atomic ratio in deposition of (a) YSZ, (b) GDC, and (c) CZO. Note that EDS represents energy dispersive X-ray spectrometry and XPS denotes X-ray photoelectron spectroscopy. Reprinted from Ref. [71].... 33

Figure 15 Platinum interdigitated electrode pattern. The width and the inter-space of the electrodes were both kept at 100 μm. The total perimeter length of the electrode was $\approx$ 115 mm. 36

Figure 16 A typical impedance spectrum of a ceramic solid electrolyte fitted by an equivalent circuit composed of three R-CPE elements connected in series. Reprinted from Ref. [79]. 39

Figure 17 A schematic structure of the home-built quartz sample holder. 40

Figure 18 XRD patterns of $Ce_{1-x}Zr_xO_2$ thin films with Zr content of $0 \leqslant x \leqslant 0.65$ deposited on Al_2O_3 (0001) substrates. Note that the intensity scale is logarithmic. 43

Figure 19 Schematic diagram of the multilayered structures composed of alternating layers of YDC and CZO. 45

Figure 20 Typical θ-2θ XRD patterns of multilayers composed of (a) YDC with CZO45, (b) YDC with CZO30, and (c) YDC with CeO_2 deposited on Al_2O_3 (0001) substrates. *N* indicates the number of YDC/CZO bilayers. 47

Figure 21 (a) Impedance spectra of YDC/CZO45 multilayer with $N = 1$ at the temperatures indicated and the equivalent circuit used to fit the data (R_{YSZ} was a fixed value at each temperature), and Arrhenius plots of the electrical conductivities of the YDC layers within multilayers composed of (b) YDC/CZO45, (c) YDC/CZO30, and (d) YDC/CeO_2. The YDC thin film data came from measurements of a single layer film with thickness ≈ 195 nm. 50

Figure 22 XRD patterns of multilayered thin films composed of *N* bilayers of (a) YSZ and CeO_2, (b) YSZ and CZO30, and (c) YSZ and CZO45. The corresponding single-layer YSZ and CZO thin films deposited on Al_2O_3 (0001) with thickness of ≈ 105 nm were also included for comparison. 54

Figure 23 Impedance spectra measured in open air of YSZ/CZO45 multilayers with $N = 10$ at the temperatures indicated. Also shown is the equivalent circuit used to fit the data (R_{YSZ} was a fixed value at each temperature)..... 57

Figure 24 Arrhenius plots of the electrical conductivity of the YSZ layers in the (a) YSZ/CeO_2, (b) YSZ/CZO30, and (c) YSZ/CZO45 multilayers. Shown for comparison is the conductivity measured from a single-layer YSZ film with thickness of ≈ 105 nm. 59

Figure 25 Schematic diagram of the structures of $Ce_{0.95}Y_{0.05}O_{2-\delta}$ films with modulated composition. The Y-dopant concentration *z* in $Ce_{1-z}Y_zO_{2-z/2}$ layers was gradually increased while keeping the net Y-dopant concentration of the whole film at a constant 5% by adjusting the relative thickness ratio between CeO_2 and Y-containing layers. 60

Figure 26 XPS spectra of YDC film sputtered at 150 W/50 W for Ce/Y targets: (a) survey-scan spectrum, (b) high resolution spectrum of Ce3d, and (c) high resolution spectrum of Y3d..... 62

Figure 27 θ-2θ XRD patterns of samples of A to D grown on Al_2O_3 (0001) substrates. The asterisk indicates the substrate peak of Al_2O_3 (0006). Other peak locations were indicated by the Miller indices of the ceria lattice. Note that the intensity scale is logarithmic..... 65

Figure 28 Depth profiles of the YO^+ obtained by TOF-SIMS through the top three bilayers of samples of B, C, and D. Grey points represent the original signal with black lines providing a 50-point moving average. Note that the intensity scale is logarithmic. 66

Figure 29 (a) Bright field TEM image of a cross section of sample D. In addition to the film, the substrate and platinum electrode are visible. (b) High resolution TEM of a near-substrate portion of the film cross section. 68

Figure 30 Impedance spectra of sample D at the temperatures indicated and the equivalent circuit used to fit the data..... 69

Figure 31 (a) Arrhenius plots of electrical conductivities measured for all samples, (b) the activation energy of the $\sigma \cdot T$ product of the samples as a function of the Y-dopant concentration in the Y-containing layer. Sample D is plotted at zero dopant concentration for reasons detailed in the following sections. Also shown for reference is the activation energy of conventionally fabricated YDC samples as reported in Ref. [38], and pure Y_2O_3, as calculated from oxygen diffusion measurements reported in Ref. [98]. (c) Electrical conductivity of sample D as a function of oxygen partial pressures at temperatures of 500 °C, 550 °C, and 600°C. 72

Figure 32 Typical θ-2θ XRD patterns of heterogeneously doped CeO_2 films composed of alternating layers of CeO_2 with (a) Y_2O_3, or with (b) Gd_2O_3, or with (c) La_2O_3 on Al_2O_3 (0001) substrates. A single layer CeO_2 film with thickness of $\approx$ 105 nm was also included for comparison. 75

Figure 33 (a) Impedance spectra of a heterogeneously doped film composed of bilayers of 1 nm-thick Gd_2O_3 and 4-nm thick CeO_2 at the temperatures indicated. The equivalent circuit used to fit the data is inset. (b, c, d) Arrhenius plots of the electrical conductivity of heterogeneously doped films composed of CeO_2 with (b) Y_2O_3, (c) Gd_2O_3, or (d) La_2O_3. The symbols indicate whether the films consist of (*squares*) 10 bilayers of 1 nm RE_2O_3/19 nm CeO_2, (*circles*) 20 bilayers of 1 nm RE_2O_3/9 nm CeO_2, or (*triangles*) 40 bilayers of 1 nm RE_2O_3/4 nm CeO_2. The conductivities of single-layer $Ce_{0.90}Y_{0.10}O_{2-\delta}$ (YDC), $Ce_{0.80}Gd_{0.20}O_{2-\delta}$ (GDC), and $Ce_{0.85}La_{0.15}O_{2-\delta}$ (LDC) thin films with thicknesses of 192 nm, 173 nm, and 256 nm, respectively, were also included for comparison. 78

Figure 34 The isothermal electrical conductivity of the heterogeneously doped films composed of CeO_2 with (a) Y_2O_3, (b) Gd_2O_3, and (c) La_2O_3 as a function of the number of interfaces at three different temperatures, respectively. Note that average measurement temperatures for the three samples are given. 79

Figure 35 The two different conduction paths through the YDC or YSZ layers in YDC/CZO and YSZ/CZO multilayers. The black rectangular region represents the interfacial conduction path and the white region denotes the bulk conduction path. 81

Figure 36 Conductivity isotherms at 650 °C of the three different types of multilayers as a function of the reciprocal thickness of the YDC layers, $1/d$. The error bars represents estimated measurement uncertainty of a single sample. 83

Figure 37 Conductivity isotherms at 650 °C of (a) YSZ/CeO_2, (b) YSZ/CZO30, and (c) YSZ/CZO45 multilayers as a function of the reciprocal thickness of the YSZ layers, $1/d$. 83

Figure 38 The calculated volume and interfacial conductivities for three different multilayers as a function of temperature. The YDC thin film data comes from measurements of a single layer film with thickness $\approx$ 195 nm. Note that the open symbols represent the volume conductivity and the solid symbols denote the interfacial conductivity. 84

Figure 39 The calculated volume (bulk) and interfacial conductivities for three different types of multilayers of YSZ/CeO_2, YSZ/CZO30, and YSZ/CZO45 as a function of temperature. The YSZ thin film data comes from measurements of a single layer film with thickness of $\approx$ 105 nm. Note that the open symbols represent the volume conductivity and the solid symbols denote the interfacial conductivity 85

Figure 40 Normalized conductivity of the multilayers as a function of the lattice mismatch. Note that the y-axis scale is logarithmic. 88

Figure 41 A schematic anion superlattice structure at RE_2O_3/CeO_2 interface. Grey circles represent oxygen in the CeO_2 lattice, while black circles represent oxygen in the RE_2O_3 lattice. The open squares represent unfilled sites in RE_2O_3. The arrow indicates the movement of an oxygen ion from CeO_2 into RE_2O_3, creating an oxygen ion interstitial at the previously unfilled site in RE_2O_3 and leaving behind an oxygen vacancy in CeO_2. 91

Figure 42 The distribution of oxygen vacancies in a bilayer composed of a 19 nm-thick CeO_2 layer in contact with a 1 nm-thick Y_2O_3 layer at the temperatures indicated. 94

Figure 43 Comparison of parallel conductance of the sample composed of 1 nm-thick Y_2O_3 and 19 nm-thick CeO_2 to that of its doped layers of Y_2O, bulk of CeO_2, and space charge regions. 99

Figure 44 Activation energy of heterogeneously doped films composed of CeO_2 with Y_2O_3, Gd_2O_3, or La_2O_3 as a function of the number of interfaces 102

Figure 45 Activation energy of the $\sigma \cdot T$ product of the heterogeneously doped CeO_2 films as a function of the lattice parameter mismatch between the dopant and CeO_2. Note that the lattice mismatch is calculated based on the Equation (7) in which *a* represents the lattice parameter. The dotted line represents the activation energy of very lightly doped CeO_2 with 0.05 mol% Y_2O_3 [38]. 103

Figure 46 The conductivity per interface obtained from the slope of linear fit of the conductivity as a function of interfaces in Figure 34. 105

ABSTRACT

The high operating temperature (> 800 °C) of solid oxide fuel cells (SOFCs) is required to a large degree by insufficient low temperature oxygen ion conductivity of the electrolyte materials such as Y_2O_3-stabilized ZrO_2 (YSZ). This extremely high operating temperature decreases cell durability and increases the component cost of SOFCs. Finding means to increase the conductivity of the electrolytes and thereby decrease the operating temperature to below 500 °C plays a decisive role in wider commercialization of this clean power technology.

Thin film processing methods offer a number of means to investigate and engineer ion conduction in solid electrolytes. Numerous recent reports have been focused on the study of nanostructured multilayers or heterostructures for solid electrolytes. The driving force behind this trend is the notion that the interfaces between two oxides may have significantly altered—ideally improved—ionic transport behavior in fluorite-structured materials. In this dissertation, we take advantage of a recent developed film deposition method to systematically study the interfacial effects on oxygen ion conduction in ZrO_2-and CeO_2-based materials. This fabrication technique allows us to create mesoscale compositional heterogeneity by using films with composition $Ce_{1-x-z}Zr_xD_zO_{2-z/2}$ (D = Y, Gd, or La) where x or z can vary through the thickness of the film at the single nanometer level.

Interfacial lattice mismatch strain has been controversially suggested as a means to alter ionic conductivity in solid ion conductors. The first type of multilayered

films prepared in this dissertation was composed of $Ce_{1-x}Zr_xO_2$ (CZO) with Y_2O_3 doped CeO_2 (YDC) or with YSZ. The aim of this study was to systematically quantify the effects of biaxial compressive or tensile strains on oxygen ion conductivity in doped CeO_2 and doped ZrO_2 materials. Since the lattice parameter of CZO is highly dependent on the Ce/Zr atomic ratio, its use enables precise control of the strain magnitude in neighboring lattice planes of YDC or YSZ. The compressive strain in the YDC layers caused fairly drastic reductions in the ionic conductivity. Each 1% increase in compressive strain of the YDC yielded a 1.6-fold reduction in interfacial conductivity at 650 °C and 3-fold reduction at 450 °C. On the other hand, when decreasing the individual layer thickness form 35 nm to 5 nm, all of the YSZ/CZO multilayers with lattice mismatch ranged between +2.9% and 5.2% exhibited little change of the conductivity, with values consistently near that of bulk YSZ. X-ray diffraction results indicated that the interfacial tensile strains in YSZ layers were largely relaxed.

The interaction between dopants and oxygen vacancies is one of the major causes for the decreased conductivity at higher dopant concentration in ZrO_2- and CeO_2-based ion conductors. The second type of multilayers prepared in this dissertation was composed of alternating highly doped and undoped CeO_2 layers. At the limit, the modulated films consisted of very thin layers of pure dopant oxide (e.g., Y_2O_3, Gd_2O_3 or La_2O_3) within thicker layers of pure CeO_2. The three dopant oxides examined, Y_2O_3, Gd_2O_3 and La_2O_3, adopt the cubic bixbyite crystal structure with "pseudo-fluorite" lattice parameters that are, relative to CeO_2, smaller (Y_2O_3), larger (La_2O_3), and nearly equal (Gd_2O_3). Due to the dopant concentration gradient, vacancies created in the layers with high concentration were expected to diffuse into

the pure CeO_2 layers with low concentration, forming space charge regions at the interfaces. This study aimed to investigate the effect of vacancy trapping on the overall oxygen ion conduction in heterogeneously doped CeO_2 films, since the oxygen vacancies which trapped in the space charge regions located in the nominally pure CeO_2 layers were expected to be highly mobile. An electrostatic Gouy-Chapman model was implemented to give the distribution of the oxygen vacancies in the space charge regions of pure CeO_2 layers. Conduction was found to occur predominantly by the vacancies trapped in the CeO_2 space charge regions in films composed of pure dopant oxide and pure CeO_2 layers. Moreover, the total conductivity of these films increased with increasing lattice parameter of the dopant oxides. The Gouy-Chapman model was not sufficient to explain this behavior, since all of the dopants theoretically contributed identical interfacial oxygen vacancy concentrations. Therefore, an extended Gouy-Chapman model was proposed that considered the effects of interfacial strain on the concentration and mobility of vacancies from dopant oxides in the space charge regions.

Chapter 1

INTRODUCTION

1.1 Motivation

Since the industrial revolution in the late 18th century, the use of machines in manufacturing and transportation greatly improved working efficiency, production capacity, and quality of life. But at the same time, a large number of energy resources were consumed in order to maintain the operation of a larger number of machines. Fossil fuels, including coal, petroleum oil, and natural gas, have been recognized as one of the major sources for this large energy demand [1]. Large-scale use of fossil fuels to create energy, however, threatens both environmental sustainability and energy security.

The conversion of chemical energy from fossil fuels into useful mechanical or electrical energy is normally carried out in thermal-mechanical conversion systems (e.g., internal combustion or IC engines) via combustion processes [2]. One of the most serious issues brought by burning of fossil fuels is their large amount of emissions, such as carbon dioxide (CO_2), nitrogen oxides (NO_x), sulfur oxides (SO_x), and particular matter [3, 4]. The release of these emissions into the atmosphere can lead to severe air pollution or even long-term climate change [5-7]. The severe air pollution events that happened in London in 1952 [8] and Beijing after 2010, give humanity painful lessons about how important it is to protect the atmosphere by reducing the emissions from burning fossil fuels.

Reducing the dependence on fossil fuels is also driven by the fact that fossil fuels are non-renewable energy resources. The total storage capacity on Earth is fixed, and scientists are quite sure that fossil fuels will be depleted eventually [9]. With the rapid growth in economy and standards of living worldwide, the demand for fuels, especially for petroleum oil, is fast growing [10]. Once the demand becomes greater than the supply, the cost for energy is expected to increase significantly. Facing ever-increasing petroleum oil prices, humanity is involved in a struggle between environment protection, fuel depletion, and economic growth.

Although some alternative renewable energy resources, such as solar, wind, and biofuels, show great promise to fundamentally solve this energy challenge [11, 12], the large-scale usage of them in power generation remains difficult. Figure 1 shows the energy consumption by fuel source in the United States predicted through 2040 [13]. Fossil fuels including coal, oil, and natural gas will continue to be the dominant energy sources for the next 30 years or more. Faced with this situation, one of the most promising means to reduce emissions and slow down the depletion of fossil fuels is to efficiently utilize them by extracting more useful energy from their consumption. The energy conversion efficiency of the widely used automobile IC engines, however, is inherently limited by the Carnot efficiency and possesses an optimized value only between 20% - 30% [14].

The need for clean power technologies with higher efficiency and flexibility in fuel choice has created a great interest in fuel cells. Fuel cells are not a new technology, as they were first demonstrated by William Grove in 1839 [15]. One of the most distinguished characteristics of fuel cells is that they are capable of converting chemical energy directly into electricity through an electrochemical

reaction [16]. Unlike IC engines, there are no intermediate thermal-mechanical conversion steps that occur in the cell reaction. The operation of fuel cells is, therefore, not restricted by the inefficiency limit of the Carnot Cycle. Fuel cells often possess a substantially higher energy conversion efficiency compared to that of traditional IC engines. Another key feature of fuel cells is reduced emissions [17]. The only by-product of the main fuel cell reaction would be pure water if hydrogen (H_2) is used as fuel. The emissions of NO_x, SO_x, and particulates are completely eliminated.

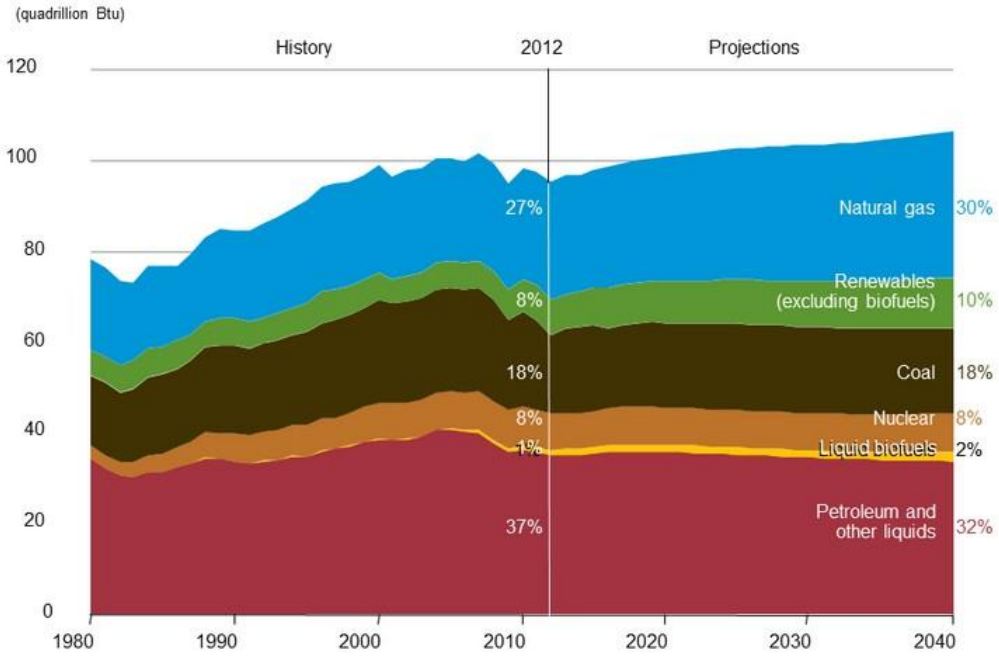

Figure 1 The US energy consumption by fuel sources predicted through 2040. Reprinted from Ref. [13].

There exist several different types of fuel cells, which are usually categorized based on the ionic species that are transported in the electrolytes [16, 18, 19]. The five major types that are currently under the most extensive development, as summarized in Table 1, include proton exchange membrane fuel cells (PEMFCs), alkaline fuel cells (AFCs), phosphoric acid fuel cells (PAFCs), molten carbonate fuel cells (MCFCs), and solid oxide fuel cells (SOFCs). Among them, SOFCs, due to their very high energy conversion efficiency and capability of being direct fed hydrocarbon fuels, has attracted much research attention. Use of SOFCs in stationary or even portable power applications can not only efficiently utilize our limited natural resources but also significantly reduce the harmful emissions.

Table 1 Comparison of five different types of fuel cell technologies [16, 18, 19].

	PEMFC	PAFC	AFC	MCFC	SOFC
Electrolyte	Polymer membrane	Liquid H_3PO_4	Liquid KOH	Molten carbonate	Ceramic
Charge carrier	H^+	H^+	OH^-	CO_3^{2-}	O^{2-}
Operating temperature	80 °C	200 °C	60-200 °C	650 °C	600-1000 °C
Fuel compatibility	H_2, methanol	H_2	H_2	H_2, CH_4	H_2, CH_4, CO
Efficiency	40-60%	35-40%	45-60%	45-60%	50-65%

1.2 Solid Oxide Fuel Cells

The SOFC is a ceramic-based fuel cell characterized by a ceramic electrolyte that can conduct oxygen ions [20]. Although an electrolyte that is capable of conducting protons could also be used in SOFCs [21], the discussion of proton-conducting SOFCs is out of the scope of this dissertation. Oxygen ion conductors were

first discovered by Nernst in 1899 [22]. At that time, Nernst found that with increased temperature, certain mixtures of oxides such as yttria (Y_2O_3) and zirconia (ZrO_2) exhibited much higher electrical conductivity compared to that of each constituent pure oxide. An optimized composition composed of 85% ZrO_2 and 15% Y_2O_3, also known as the "Nernst mass", was initially used as the filament material for lamps [23]. The ZrO_2-Y_2O_3 mixture, however, quickly lost its interest in the lamp industry after the invention of tungsten filament lamps. In 1937, Baur and Preis constructed the first SOFC using a ZrO_2-Y_2O_3 based electrolyte and the cell was successfully operated at 1000 °C [24]. Since then, the ZrO_2-Y_2O_3 composition, now known as Y_2O_3 stabilized ZrO_2 (YSZ), has been widely used as the electrolyte material for SOFCs.

The basic geometry of a SOFC is very simple, consisting of three main components: an anode, an electrolyte, and a cathode [20], as shown in Figure 2. The electrolyte, such as YSZ, is placed between the two electrodes to conduct oxygen ions. In a typical cell operation, a fuel, such as H_2, is supplied to the anode side where it is oxidized to produce electrons and hydrogen ions (H^+). Since the electrolyte is an ionic conductor, the electrons released at the anode are forced to move through the external circuit. An oxidant, such as oxygen (O_2) in the air, is supplied to the cathode side where it is reduced by gaining electrons from the anode. The generated oxygen ions (O^{2-}) are then transferred through the electrolyte from cathode to anode, forming water when they react with the H^+ ions at anode. One of the most obvious differences between conventional batteries and fuel cells is that as long as fuels and oxidants are provided to the fuel cells, electrons will be continuously released, generating electrical current in the external circuit.

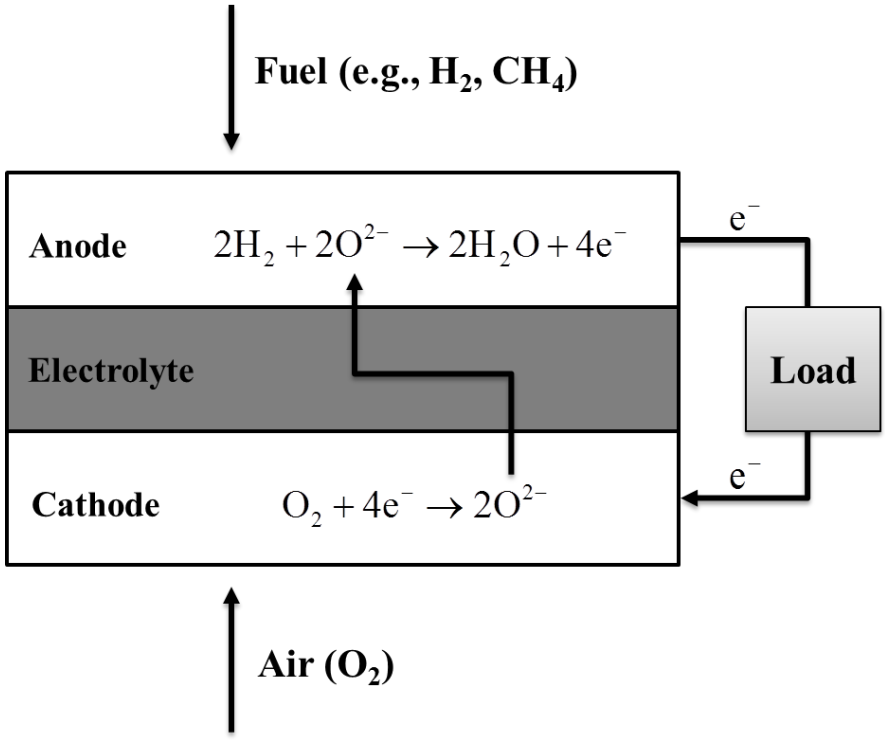

Figure 2 Schematic structure of a SOFC with hydrogen used as the fuel.

Oxygen ion conduction in the solid electrolytes is highly thermally activated [20]. Traditionally processed ceramic electrolyte, YSZ, does not achieve sufficiently high oxygen ion conductivity (≈ 0.1 S/cm) until temperatures of 800 °C to 1000 °C [18]. For this reason, current SOFCs are typically required to operate at temperatures exceeding 800 °C for sufficient performance. The high operating temperatures provide distinct advantages for SOFCs relative to the other low temperature fuel cells (e.g., PEMFCs). First, facile electrode kinetics can be achieved at high operating temperatures, allowing the use of cheaper, non-precious metals (e.g., silver, nickel), instead of platinum (Pt), for the electrode catalysts [25]. Second, at high temperatures,

hydrocarbon fuels (e.g., CO, CH_4) can now be directly fed to or "internally reformed" in fuel cells without the necessity to incorporate extra machinery or inefficiencies related to fuel reforming [26]. Third, no liquid water can accumulate at such high temperatures, relieving the issue related to water management, in particular the problem of water flooding [27]. Finally, the high-quality waste heat exhausted from the cell reaction can be reutilized in cogeneration or bottoming cycle, further increasing the energy conversion efficiency, up to 85% [28].

1.3 Technical Challenges of Solid Oxide Fuel Cells

The extremely high operating temperatures, however, also bring challenges for the development of SOFCs. The key issues include the high cost of ceramic materials for fabricating cell components and stack hardware, the durability and stability of cell components under a high operating temperature and chemically harsh environment, the method of sealing the cell to avoid gas leakage, and the extra time and equipment needed to assist the slow start up and shut down processes. In order to maintain the advantages of SOFCs operated at relatively high temperatures while also minimizing the corresponding disadvantages, finding means to decrease the operating temperatures from 1000 °C down to 500 °C plays a decisive role in wider commercialization of this clean power technology [29, 30]. An important requirement to decrease the operating temperatures of SOFCs is to increase the oxygen ion conductivity of solid oxide ion electrolytes at lower temperatures [18, 31].

1.4 Solid Oxide Ion Electrolytes

The electrolytes for SOFCs work as an oxygen ion conductor but an electron insulator. They are basically required to have sufficiently high oxygen ion

conductivity but with minimizing electron conductivity. This requirement is very important since possible electron conduction through the electrolytes can cause a "short circuit" between the two electrodes, reducing power output and overall cell efficiency [18]. Moreover, in a fuel cell, one side of the electrolyte contacts the cathode where oxidants (e.g., air) are supplied, while the other side contacts the anode where fuels (e.g., H_2) are supplied. The electrolyte, therefore, must also possess high chemical and mechanical stability in both oxidizing and reducing environment over the cell operating temperature range.

ZrO_2-based materials have been widely used as the electrolyte materials for SOFCs [18, 32, 33]. One of the most representative and best known examples is YSZ. Although YSZ only possesses moderately high ionic conductivity, it is still being widely employed in SOFC applications, mainly due to its negligible electron conductivity, high chemical stability and low cost [20]. Pure ZrO_2 adopts three polymorphs [34]. At room temperature, ZrO_2 possesses the monoclinic crystal structure, changing to a tetragonal form at 1170 °C, to a cubic fluorite structure at 2370 °C, and finally melting above 2680 °C. Of these three different structures, the symmetry and large open volume in the cubic fluorite structure make it most favorable for ion transport [35].

The addition of certain aliovalent oxides such as Y_2O_3 can not only stabilize the cubic fluorite structure of ZrO_2 down to room temperature, but also create oxygen vacancies as Zr^{4+} is substituted by the lower-valence solute cations, e.g., Y^{3+} [20]. The incorporation of Y_2O_3 dopants into ZrO_2 to form YSZ can be described by the following defect chemical reaction using Kröger –Vink notation:

$$Y_2O_3 \xrightarrow{ZrO_2} 2Y'_{Zr} + 3O_O^{\times} + V_O^{\bullet\bullet} \quad (1)$$

in which Y'_{Zr} represents a Y-atom sitting substitutionally on a Zr-site with an effective charge of -1, $V_O^{\bullet\bullet}$ represents an oxygen vacancy with an effective charge of +2, and $O_O^{\times}$ represents an oxygen atom sitting on an oxygen site with no effective charge. In order to preserve electroneutrality, the addition of one Y_2O_3 molecule into ZrO_2 induces the creation of one oxygen vacancy. Thus, increasing the dopant concentration can be used to increase the concentration of oxygen vacancies.

Oxygen ion conduction in YSZ and other cubic fluorite solid electrolytes occurs via a highly thermally activated vacancy-hopping mechanism [20]. The conductivity, σ, of an ionic material, such as YSZ, can be described as

$$\sigma = n(ez)\mu \tag{2}$$

in which n is the number density of oxygen vacancies, e is the elementary charge, z is the effective charge of the oxygen vacancy ($z = 2$), and μ is the mobility of those oxygen vacancies in YSZ [36]. The vacancy mobility can be related to its self-diffusion coefficient through the Nernst-Einstein equation as

$$\mu = \frac{(ez)D}{kT} \tag{3}$$

in which D represents the vacancy self-diffusion coefficient, k is the Boltzmann's constant, and T is the absolute temperature. The self-diffusion coefficient, D, is subjected to an Arrhenius-type temperature dependence and can be expanded to

$$D = D_0 \exp\left(-\frac{\Delta G_m}{kT}\right) \tag{4}$$

in which D_0 is a temperature-independent preexponential factor, and ΔG_m represents the free energy for migration. By substituting D from Equation (4) into Equation (3), the oxygen ion conductivity, σ, can be further written as

$$\sigma = \frac{n(ez)^2 D_0}{kT} \exp\left(-\frac{\Delta G_m}{kT}\right) \tag{5}$$

A more general and widely used form for the ionic conductivity, therefore, can now be expressed as

$$\sigma = \frac{\sigma_0}{T} \exp\left(-\frac{E_a}{kT}\right) \tag{6}$$

in which σ_0 is a temperature-independent preexponential factor with value linearly increased with the number density of oxygen vacancies, and E_a is the activation energy. By comparing Equation (6) with Equation (5), we find that E_a, at this stage, seems to be only related to the migration free energy ΔG_m.

From Equation (5), it can be seen that the conductivity of oxygen ions in solid electrolytes is linearly dependent on the concentration of oxygen vacancies. A tempting way to improve the low temperature conductivity of electrolytes is to increase the vacancy concentration by adding more dopants. Figure 3 shows the ionic conductivity of ZrO_2 as a function of dopant concentration at 1000 °C for a few relevant dopant oxides [32]. In reality, a maximum oxygen ion conductivity was obtained in all cases at $x \approx 0.1$where the dopant concentration was at the minimum level sufficient to stabilize the cubic fluorite phase of ZrO_2 at room temperature. Further increasing the dopant concentration yielded decreased conductivity. A similar nonlinear relationship between the dopant concentration and the ionic conductivity was also found in other cubic fluorite oxide-ion electrolytes, such as doped ceria (CeO_2), which also exhibits a maximum conductivity at a particularly low dopant concentration [37].

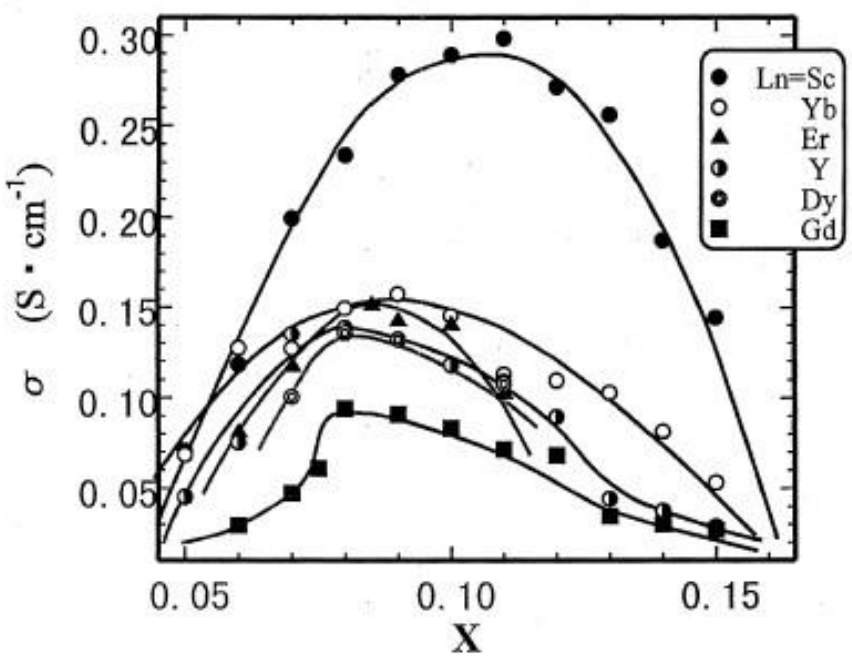

Figure 3 Ionic conductivity of $(ZrO_2)_{1-x}$ $(Ln_2O_3)_x$ as a function of dopant concentration at temperature of 1000 °C. "Ln" denotes the different dopant oxides. Reprinted from Ref. [32].

A simple model of vacancies independently hopping through the crystal lattice is not able to fully interpret the non-monotonic relationship between oxygen ion conductivity and dopant concentration. The mechanism behind this maximum conductivity at a relatively low dopant concentration is very complex. Defect association between Y'_{Zr} (or the analogous species for other dopants) and $V_O^{\cdot\cdot}$ at high dopant concentration is a widely accepted explanation for this particular conductivity behavior [36, 38-40], though vacancy-vacancy interactions have also been proposed [41]. The positively charged oxygen vacancies in defect associates, such as $(Y'_{Zr} - V_O^{\cdot\cdot})$, become trapped near the randomly distributed dopant atoms in the lattice due to both Coulombic attraction to the negatively charged dopant site as well as, at least in some

cases, local lattice strain effects caused by the different ionic radius between dopants and hosts. The association decreases oxygen vacancy mobility, leading to increased activation energy and reduced ionic conductivity. The activation energy, E_a, described in Equation (6) is, therefore, also related to the defect association between dopants and vacancies. Higher oxygen ion conductivity, therefore, cannot be achieved by simply increasing the dopant concentration.

In order to increase the oxygen ion conductivity of electrolytes used in SOFCs, one of the most direct approaches is to search for alternative materials that possess higher conductivity than that of YSZ. Figure 4 shows the electrical conductivity of several typical oxide-ion conductors as a function of the temperature [42]. Among them, some materials have been indeed demonstrated to have higher ionic conductivity compared to that of YSZ, but their application in SOFCs is still limited by various problems. A serious concern with most of these alternative materials is their structural and electrochemical stability at reduced oxygen partial pressure. For example, in Y_2O_3 doped Bi_2O_3 and Gd_2O_3 doped CeO_2, the host cations, Bi^{3+} and Ce^{4+}, can be partially reduced to Bi^{2+} or Ce^{3+} under reduced environment. This effect creates free electrons that lead to electronic conduction [42]. Since the anode side of the electrolyte always experiences low oxygen partial pressure, incorporation of them into SOFCs becomes questionable. Sc_2O_3 doped ZrO_2 possesses much higher conductivity compared to that of YSZ due to the similar ionic radius between Sc^{3+} and Zr^{4+} [32]. This material, however, is not widely utilized in SOFC applications mainly due to the prohibitive cost of Sc_2O_3 [43]. Challenge still remains in finding new materials for electrolytes to meet the requirements for SOFCs operated at intermediate temperatures.

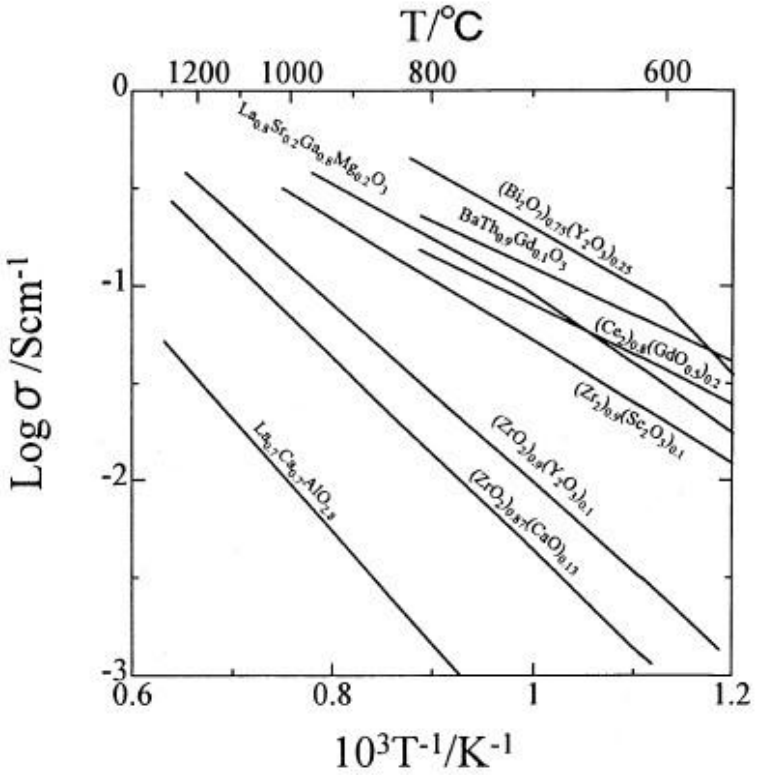

Figure 4 Ionic conductivities of several typical oxide ion conductors as a function of the temperature. Reprinted from Ref. [42].

1.5 Nanometric Multilayers for Solid Electrolytes

Recently, a number of research efforts have been directed towards the development of nanostructured multilayers or heterostructures for solid electrolytes [44-50]. Compared to the conventional bulk materials, nanostructured multilayers are characterized by a significantly increased volume fraction of heteromaterial interfaces. The interfaces, which normally possess higher defect densities (including point and/or linear defects) and lattice mismatch strain, are likely to affect—ideally to improve—the ionic transport behavior in fluorite materials.

1.5.1 Space Charge Effects on Ionic Conduction

Sata et al. published the first paper to study the interface effects on the ionic conductivity using multilayered thin films [51]. In this research, epitaxial, undoped CaF_2/BaF_2 heterostructures were fabricated by molecular beam epitaxy on Al_2O_3 substrates. By keeping the total film thickness of the multilayers constant, the authors observed a continuous increase in F^- ion conductivity as the individual layer thickness decreased from 250 nm to 8 nm (increasing the number of interfaces). This result is shown in Figure 5. The maximum F^- ion conductivity was found to be at least two orders of magnitude higher than that of either pure BaF_2 or CaF_2. This enhancement was explained by ion redistribution in space charge regions adjacent to the interfaces where F^- ions were transferred from BaF_2 to CaF_2 [52, 53]. The F^- site vacancies left in the BaF_2 layers significantly increased the total ionic conductivity as the layer thickness became comparable to the size of the space charge regions.

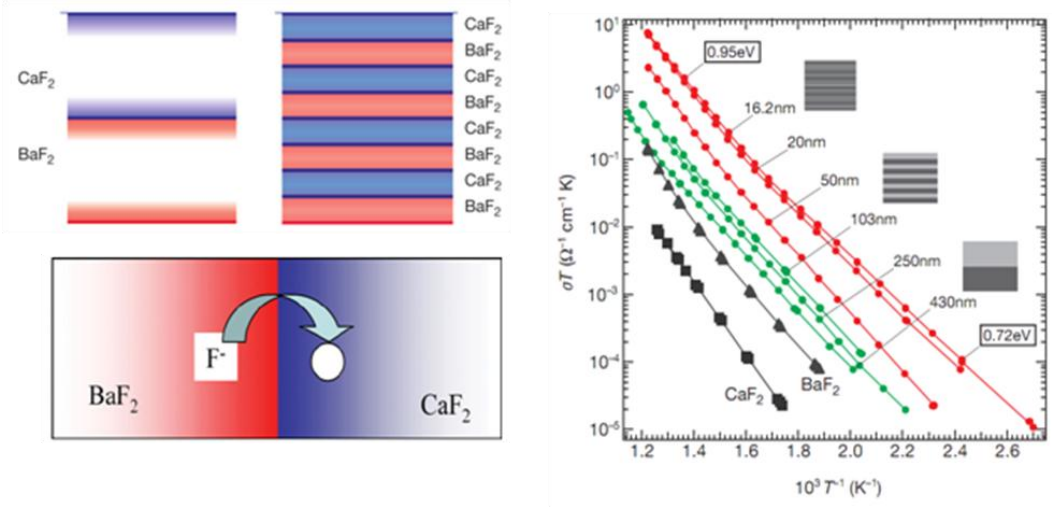

Figure 5 The ionic conductivity of the multilayered films consisting of alternating layers of undoped BaF_2 and CaF_2 on Al_2O_3 substrates. Reprinted from Ref. [51] and [52].

1.5.2 Interfacial Strain Effects on Ionic Conduction

1.5.2.1 Multilayers Composed of Two Doped Conductors

For systems involving oxygen ion conductors, past studies have typically studied multilayers containing two different doped conductors (e.g., doped ZrO_2 and doped CeO_2). Azad et al. investigated multilayered films composed of alternate layers of Gd_2O_3 doped ZrO_2 and Gd_2O_3 doped CeO_2 on Al_2O_3 (0001) substrates [54], as shown in Figure 6. The Gd-concentration was a constant of 12 at% in each constituent layer. Similar to what was found in the BaF_2/CaF_2 multilayers, the oxygen ion conductivity increased gradually when decreasing the discrete layer thickness down to 15 nm. Further decreasing the discrete layer thickness, however, resulted in a decreased ionic conductivity due to the increased interfacial roughness. The maximum conductivity was reported to be at least one order of magnitude higher than that of a polycrystalline bulk CeO_2 or a single crystal YSZ thin film.

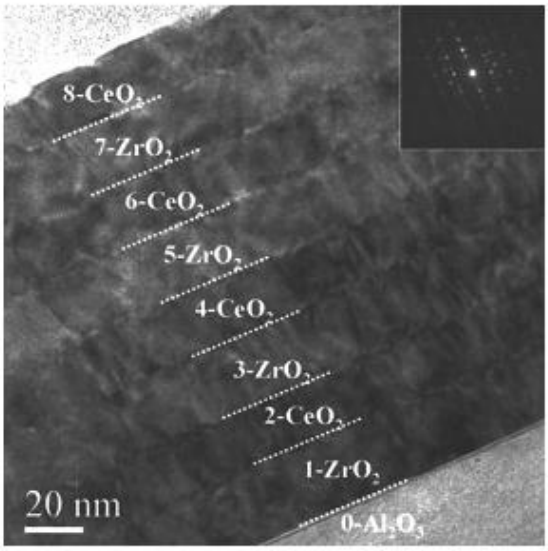

Figure 6 Transmission electron micrograph of CeO_2/ZrO_2 multilayer with constant dopant concentration. Reprinted from Ref. [54].

A similar study was also carried out by Sanna et al. using multilayered film composed of 20 mol% Sm-doped CeO_2 (SDC) and 8 mol% Y_2O_3-stabilized ZrO_2 (YSZ) [55]. Pulsed laser deposition was utilized to fabricate films with a thin $SrTiO_3$ (STO) buffer layer placed between the (001) MgO substrate and the first SDC layer. This thin buffer layer was used to adapt the large crystallographic mismatch between SDC and MgO substrate, ensuring epitaxial growth in the multilayered films. The authors investigated the influence of interfaces on the total ionic conductivity based on two different types of experiments: first, keeping the overall film thickness constant while decreasing the individual layer thickness to increase the number of interfaces; second, keeping the number of interfaces at constant while varying the individual layer thickness. The total ionic conductivity was significantly increased in both cases by almost an order of magnitude at 700 °C when the thickness of SDC/YSZ bilayers decreased to 7.7 nm. Later study by Li et al. also found a significant increase in oxygen ion conductivity by two orders of magnitude in multilayers composed of YSZ and $Gd_2Zr_2O_7$ [56].

Unlike the undoped BaF_2 and CaF_2 used in Ref. [51, 52], defect concentrations in these highly doped ZrO_2 and/or doped CeO_2 are normally very large such that the space charge regions are inconsequently small (≈ 1 Å [54]). The influence of oxygen vacancy redistribution at the interfaces on the total vacancy concentration in these films can likely be neglected. The vacancy concentration was dominantly fixed by the amount of added dopants. Instead, structural features near the interfaces such as lattice strain were envisioned as means to alter the mobility of the *existing* defects, thereby increasing the oxygen ion conductivity.

1.5.2.2 Multilayers Composed of One Doped Conductor and One Insulator

The structure of the interfaces formed between two different materials is highly dependent on their crystalline symmetry and lattice parameters. If the two constituent materials have closely related lattice symmetry but different lattice parameters, the lattice mismatch at the interface can be calculated as

$$f_{12} = \frac{a_2 - a_1}{a_1} \tag{7}$$

in which f_{12} represents the lattice mismatch of material "1" relative to the material "2" and "a" denotes the lattice parameter of these two materials. According to the degree of lattice mismatch, the interfaces can often be categorized into the following three types: coherent, semicoherent, and incoherent, as shown in Figure 7 [57].

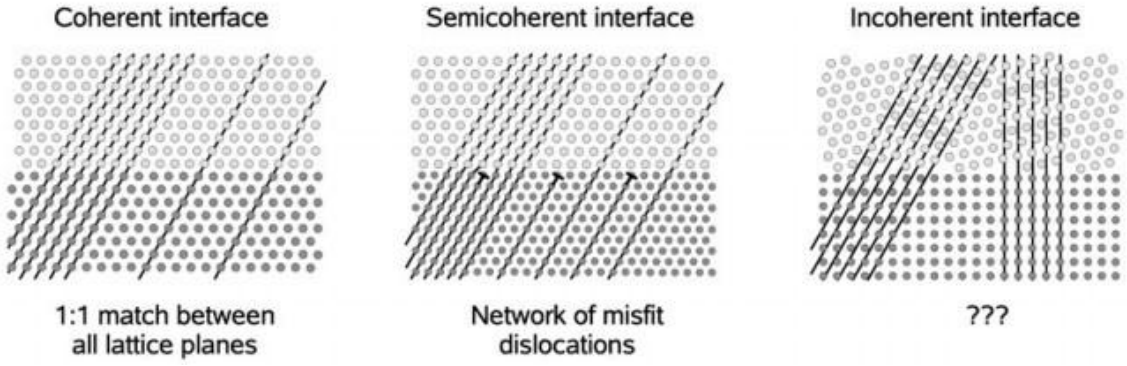

Figure 7 Three different types of interfacial structures changed with the lattice mismatch. Reprinted from Ref. [57].

Small lattice mismatch is normally required in order to fabricate atomically flat, coherent interface in which lattice mismatch is completely compensated by elastic deformation or strain. As shown in Figure 8 with a coherent interface, the material

with smaller lattice parameter will be expanded in the direction parallel to the interface, while the material with larger lattice parameter will be compressed in order to adapt the crystallographic compatibility at the interfacial region. There will be a biaxial tensile strain induced in the material with smaller lattice parameter with a corresponding biaxial compressive strain in the material with larger lattice parameter.

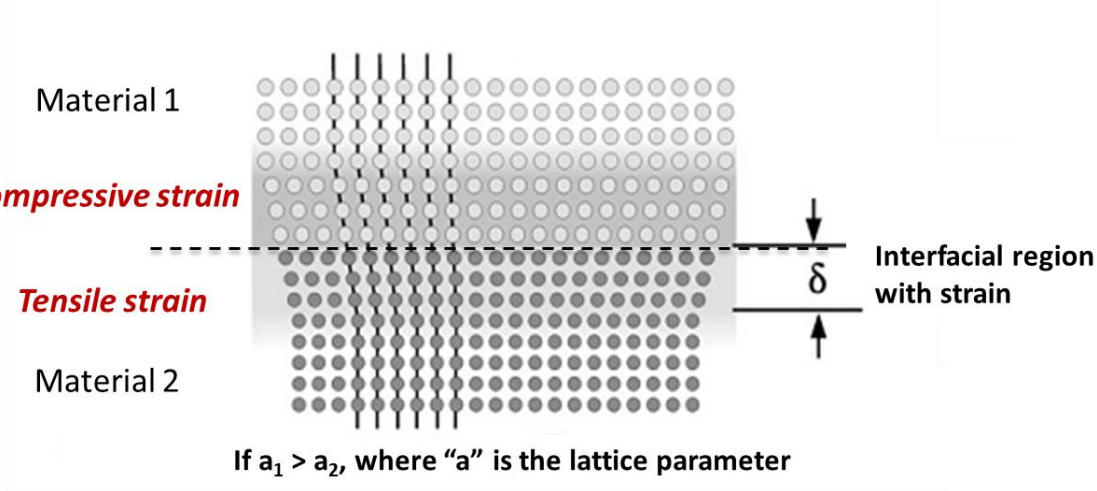

Figure 8 Coherent-interface structure of a multilayer composed of two different materials. Reprinted and revised from Ref. [57].

Once the lattice mismatch grows too large for the strain to be elastically accommodated at interface, it will be partially or completely released by the introduction of misfit dislocations and/or highly disordered interfacial irregularities, forming semicoherent or incoherent interfaces. Strain relaxation reduces the effective average strain imposed on the constituent layers. The lattice mismatch that is calculated based on the crystallite geometry, therefore, cannot be simply equivalent to the interfacial strain except for coherent interface with negligible concentration of misfit dislocations. The specific role of tensile or compressive strain in controlling the

oxygen ionic transport is difficult to discern from the reported studies with multilayers composed of two doped conductors [54-56], since the tensile strain induced in doped ZrO_2 comes with a compressive strain induced simultaneously in doped CeO_2.

Other studies constructed multilayers using an insulating phase with an oxygen ion conductor. The insulating phase is only responsible to induce tensile or compressive strains in the conductor but plays little role in the total electrical conduction parallel to the interfaces. A systematic study of the effects of lattice strains on the oxygen ion transport properties at interfaces has been reported in Ref. [57-60] with multilayers composed of 9.5 mol% YSZ and various insulating rare earth oxides (e.g., Y_2O_3, Lu_2O_3, and Sc_2O_3). Unlike the previous reported studies [54-56], only the strain state in the YSZ layers would affect the overall oxygen ion conduction. The authors found that tensile strain in the YSZ layers increased the ionic conductivity, while compressive strain decreased it, as shown in Figure 9. This finding was explained by a theoretical model based on the pressure dependence of the free energy for vacancy migration. A log-linear relationship between the interfacial conductivity of the structures and the amount of coherence strain induced in the YSZ layers was derived and described as

$$\ln \frac{\sigma_{O^{2-},\text{int}}}{\sigma_{O^{2-},vol}} \propto \Delta V_V^M f_{12} \tag{8}$$

in which $\sigma_{O^{2-},\text{int}} / \sigma_{O^{2-},vol}$ represents the ratio between the conductivity of the interface region and bulk conductivity, ΔV_V^M is the vacancy migration volume, and f_{12} denotes the lattice mismatch between an ionic conductor (1) and an insulator (2). The authors pointed out that for a vacancy-type hopping mechanism, ΔV_V^M was always positive. Thus, it could be expected that for $f_{12} > 0$ ($a_1 < a_2$ results in a tensile strain in the

ionic conductor), the interfacial conductivity would be increased; but for $f_{12} < 0$ ($a_1 > a_2$ results in a compressive strain in the ionic conductor), the interfacial conductivity would be decreased compared to that in the bulk. This finding was in good agreement with what was observed in the experiments as shown in Figure 9.

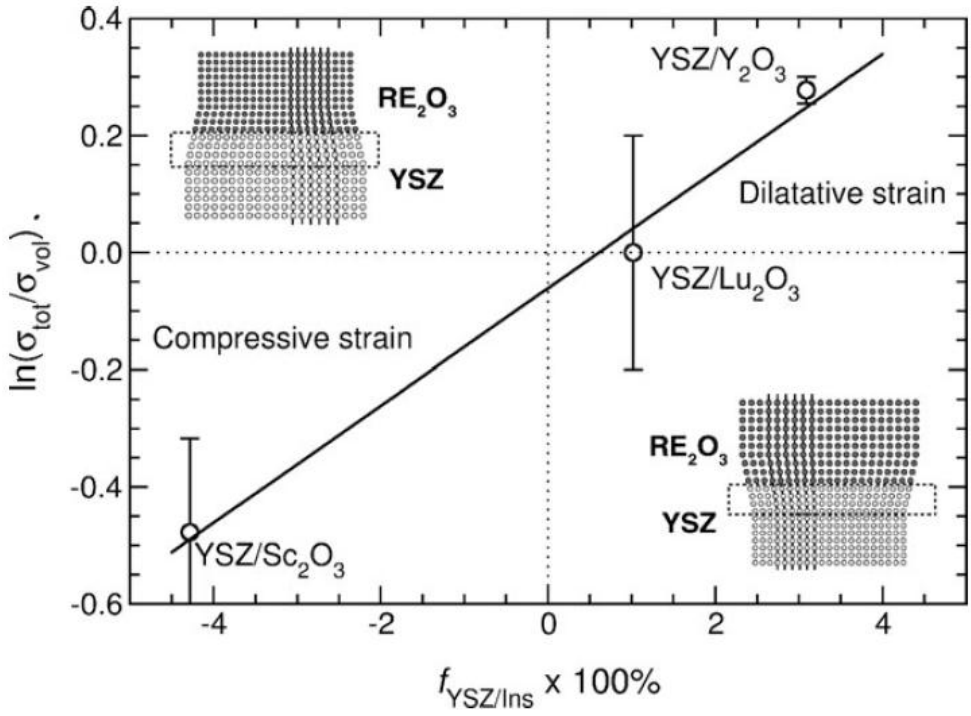

Figure 9 Logarithm of the maximum change of the total conductivity relative to the bulk conductivity as a function of the lattice mismatch. Reprinted from Ref. [60].

The effects of mechanical strains on the electrical properties of oxygen ion conductors have also been widely studied by computational simulations. Kushima et al. investigated the diffusion of oxygen ions in biaxially tensile-strained YSZ using density functional theory (DFT) and nudged elastic band (NEB) method [61]. At all

the temperatures between 400 K and 1000 K, the oxygen ion diffusivity, as shown in Figure 10, was found to be significantly increased initially, but reached a maximum value at a tensile strain of +4%. Further increasing the tensile strain, however, yielded decreased oxygen ion diffusivity due to the strain relaxation. The maximum increase in the oxygen ion diffusivity was gradually decreased from 3.8 to 2.5 orders of magnitude when the temperature increased from 400 K to 1000 K. The increased conductivity in tensile-strained YSZ was attributed to the decreased migration barrier for oxygen ions. Fronzi et al. studied the structural and electrical properties of undoped ZrO_2-CeO_2 interfaces based on the DFT calculations [62]. The authors found that tensile strain in ZrO_2 significantly decreased the intrinsic vacancy formation energy, while the compressive strain in CeO_2 significantly increased it. Buckeridge et al. found that oxygen ions in CeO_2 were more preferred to move from their ideal lattice site to the interstitial site when the material was thermally expanded [63]. The transfer of oxygen ions into the interstitials, therefore, would create more movable oxygen vacancies in the lattice. Moreover, it has been well established that the creation of a vacancy in fluorites yields an expansion of the lattice [64]. Therefore, a negative lattice strain gradient, with the insulator under compression and oxygen ion conductor under tension, may provide a driving force to transfer oxygen vacancies across the interfaces into the oxygen ion conductors. But, it should be noted that the increasing intrinsic vacancy concentration may increase the conductivity only in undoped materials. In highly doped materials, for example, YSZ, since the concentration of the defects is dominantly determined by the content of added dopants, the creation of small amount of intrinsic oxygen vacancies would probably have little impact on the overall oxygen ion conduction.

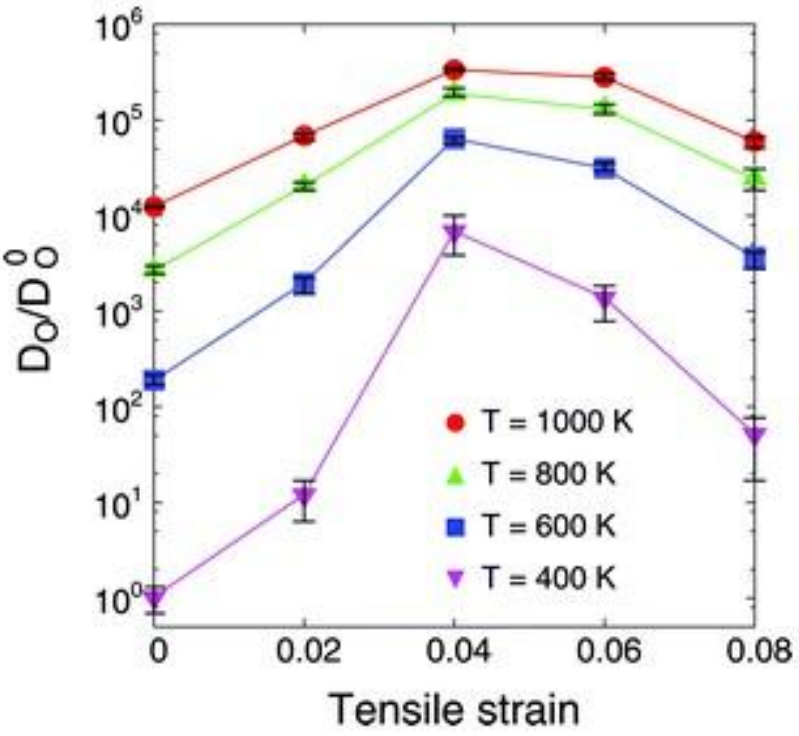

Figure 10 The relative enhancement of the oxygen ion diffusivity in YSZ as a function of the tensile strain at four different temperatures. D_O^0 represents the oxygen ion diffusivity of YSZ at 400 K with zero strain. Reprinted from Ref. [61].

The conduction behavior reported in these reported experimental and numerical works [54-61], however, has proven difficult to repeat. Garcia-Barriocanal et al. fabricated multilayers composed of 8 mol% YSZ and $SrTiO_3$ (STO) on STO substrates [65]. The YSZ layers were found to be coherently strained to STO when its thickness was decreased to 1 nm, resulting in atomically flat and dislocation-free interface structure. An extremely large tensile strain, up to ≈ 7%, was predicted to exist in the ultra-thin YSZ interface planes. The total conductivity in a multilayer with 1 nm-thick YSZ was reported to have increased by up to eight orders of magnitude.

The authors attributed this huge increase of conductivity to the large tensile strain in YSZ layers, but evidence from ongoing experiments suggested that the electronic conduction through the layers of STO probably caused the substantial increase of the total conductivity and not, as desired, purely by increased ionic conduction in YSZ layers [66-68]. A more recent study carried out by Pergolesi et al. found that tensile strain in YSZ did not affect the transport of oxygen ions in multilayers composed of YSZ and CeO_2 [69]. The authors prepared five different samples with individual layer thickness decreased from 60 nm into 5 nm, but all of them achieved almost the same activation energy and conductivity near to that of the single-layer YSZ thin film.

1.6 Conclusions of Literature Review

Thin film processing methods offer a number of means to investigate and engineer ion conduction in solid electrolytes. Nanostructured multilayers or heterostructures using different oxide-ion conducting oxides has become of great interests to study the interfacial effects. The relationship between interfacial lattice mismatch strain and ionic conductivity in solid oxide electrolytes, however, has become a very controversial topic of late.

A significant increase in oxygen ion conductivity in multilayers composed of two highly doped electrolyte layers has been observed, but the actual mechanism behind this phenomenon is still not very clear. The conductivity enhancement has been attributed to the interfacial strains increasing the oxygen vacancy mobility, with little mechanistic insight. One of the major limitations in deriving such insight is that these experiments always used two highly doped ionic conductors [54-56]. At interfaces, if there is a tensile strain induced in one material, there will be a compressive strain induced simultaneously in another one. The net effect of the interfacial strain on the

transport properties of oxygen ions in these experiments is thus difficult to deconvolute.

In order to avoid this difficulty, the studies reported in Ref. [57-60, 69, 70] investigated multilayers involving an oxide solid electrolyte composed of an ion conductor and an insulating oxide. Strain in the ion conductor was varied by using insulting oxides with different lattice parameters. The change of the total oxygen ion conductivity of the whole multilayers was dominantly determined by the strain state in the ion conductors. The experimental results, however, have been found to be still controversial. A systematic study of the effect of strain on the oxygen ion conduction behavior is still needed, but multilayered films prepared by the reported methods have a limited number of discrete strain states possible. A new appropriate insulating oxide is needed to be searched every time in order to achieve a different strain. This method, therefore, significantly increases the experiment cost and somewhat complicates the sample fabrication, since a new deposition recipe and/or target is needed for each insulating oxide.

Oxygen vacancy redistribution at the interfaces in multilayers composed of two oxygen ion conductors would exhibit little impact on the overall oxygen ion conduction due to the extremely small space charge regions. But in the multilayers composed of a doped oxygen-ion conductor and an insulator (e.g., YSZ/CeO_2 [69]), oxygen vacancies are probably able to transfer from the doped layers into the insulators, forming space charge regions at interfaces due to the defect concentration gradient. In the insulator layers, such as CeO_2, there is only a very small amount of dopant-impurities such that the effects of dopant-vacancy interaction on the vacancy mobility can likely be neglected. Oxygen vacancies which trapped in the space charge

regions of the insulator layers may move with a larger mobility. Focusing on the study of the space charge regions in such multilayers may provide another means to engineer the overall oxygen ion conduction, ideally improving the oxygen ion conductivity.

1.7 Objectives of the Research

One of the simplest ways to adjust the lattice parameters, and thereby interfacial strain, between two adjacent layers, is to spatially modulate the dopant and/or host atom concentration. We recently developed a novel thin film deposition method that allows us the creation of metal oxide thin films within a solid solution space where the cation composition is controlled at the single nanometer level [71]. A few sets of experiments enabled by this technique are summarized in Figure 11 using films of $Ce_{1-x-z}Zr_xD_zO_{2-z/2}$ (D = Y or Gd) where x or z can vary through the thickness of the film. Most plainly, the effects of the film-air and film-substrate interfaces can be studied by altering the film thickness and substrate type, as shown in Figure 11(a). Beyond this sample case, multilayers that interleave doped CeO_2 or ZrO_2 layers with undoped $Ce_{1-x}Zr_xO_2$ (CZO) layers have allowed the study of well-controlled interfacial lattice mismatch, as shown in Figure 11(b).As a final example, Figure 11(c) shows CeO_2 films with dopants confined to planar, heterogeneous locations through the thickness of a film. In this dissertation, we would only focus on the study of the last two types of heterogeneous, multilayered films.

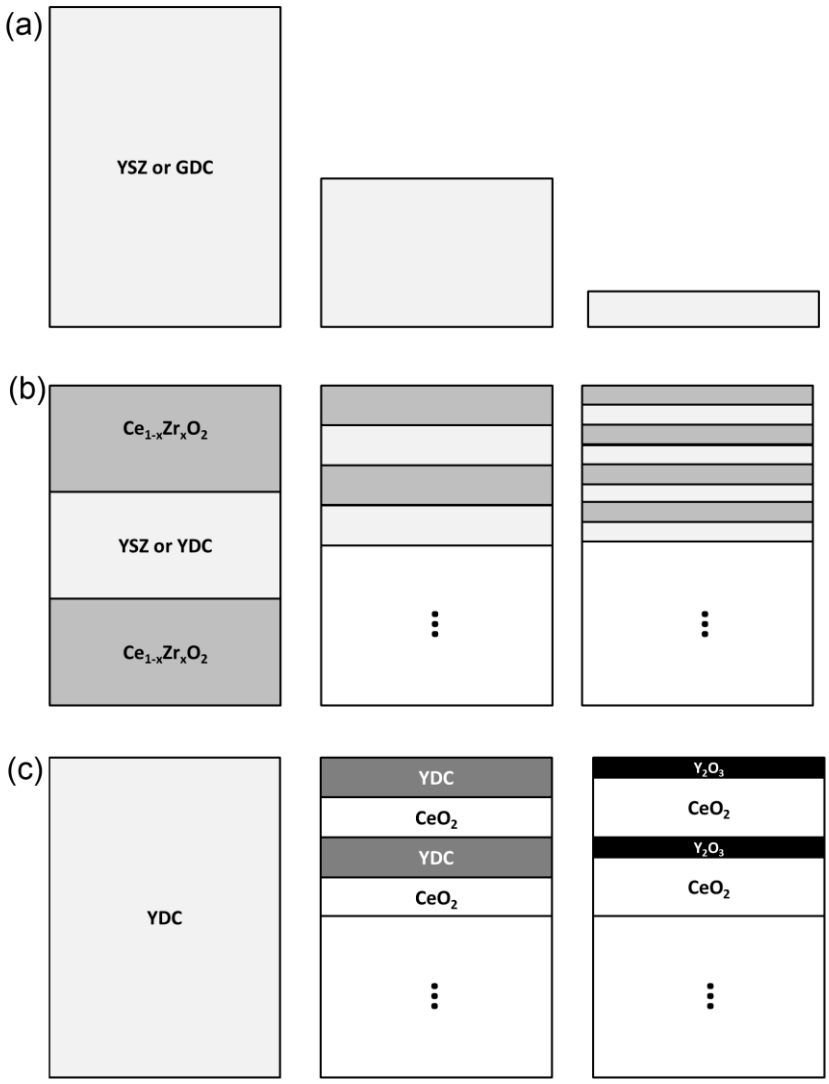

Figure 11 The three different film structures with composition $Ce_{1-x-z}Zr_xD_zO_{2-z/2}$ surveyed by using the thin film deposition technique developed recently. (a) Thin films of $Zr_{1-z}Y_zO_{2-z/2}$ (YSZ) or $Ce_{1-z}Gd_zO_{2-z/2}$ (GDC) with heterogeneity at the film substrate and film-air interfaces, studied using different film thickness. (b) Multilayers of $Ce_{1-x}Zr_xO_2$ with either $Zr_{1-z}Y_zO_{2-z/2}$ (YSZ) or $Ce_{1-z}Y_zO_{2-z/2}$ (YDC), creating interfacial lattice mismatch strain that was adjusted by changing the component layer thickness and the Ce/Zr ratio in the $Ce_{1-x}Zr_xO_2$ layers. (c) $Ce_{1-z}Y_zO_{2-z/2}$ (YDC) thin films with dopants distributed either homogeneously or with nanometer-scale modulation of dopant distribution. At the limit, the modulated films consisted of alternating layers of pure Y_2O_3 and CeO_2. Dopant oxides, Gd_2O_3 and La_2O_3, were also studied.

The use of CZO with $Zr_{1-z}Y_zO_{2-z/2}$ (YSZ) or $Ce_{1-z}Y_zO_{2-z/2}$ (YDC) to study the effects of interfacial strain on the oxygen ion conduction has many benefits compared to the previous reported studies. First, unlike the rare earth oxides used in Ref. [57-60], the lattice parameter of ZrO_2-CeO_2 solid solutions (CZO) is a strong function of the Ce/Zr atomic ratio [72]. By Vegard's law, the lattice parameter of CZO can be varied from 5.14 Å [73] for cubic ZrO_2 to 5.41 Å [74] for pure CeO_2. Construction of multilayers composed of CZO with YSZ or YDC would allow us to systematically quantify the effect of biaxial tensile or compressive strains on oxygen ion conduction by controlling the Ce/Zr atomic ratio—and thereby the lattice parameter—in CZO layers. CZO adopts cubic and/or tetragonal structures with Zr content, x, less than 0.5. The lattice parameters of cubic and tetragonal CZO ($x \leq 0.5$) are nearly the same [75], such that the X-ray diffraction patterns of these phases are very difficult to distinguish. The existence of tetragonal phase CZO does not affect its use as a means to create lattice mismatch. Another key benefit of using CZO instead of rare earth or other oxides is that the crystal structure of CZO with YSZ or YDC is very similar, which increases the likelihood of creating epitaxial, coherently-strained multilayer thin films.

Heterogeneously doped multilayers composed of alternating layers of low dopant concentration layers (e.g., concentrations down to nominally pure CeO_2) and high dopant concentration layers, as shown in Figure 11(c), have also been studied to evaluate the effects of space charge regions on the oxygen ion conduction. Due to the dopant concentration gradient, vacancies created in the layers with high concentration are expected to diffuse into pure CeO_2 layers with low concentration, forming space charge regions at the interfaces. As shown by Wang et al. [38], the mobility of oxygen vacancies in highly doped conductors was reduced from that with less dopant due to, it

is believed, the formation of defect associates between vacancies and dopants. For this reason, oxygen vacancies are expected to be highly mobile in the space charge regions located in the low dopant concentration, or nominally pure CeO_2 layers to increase the overall oxygen ion conductivity. This design is somewhat analogous to the high electron mobility transistor (HEMT), in which electrons produced in a doped AlGaAs layer are trapped into the neighboring region of undoped GaAs and then move with much higher mobility [76]. The theory of heterogeneously doped electrolyte films was developed for the first time by adjusting the net dopant content and the dopant identity. Three rare earth metal oxides included Y_2O_3, Gd_2O_3, and La_2O_3 were examined as the dopant oxides. In this type of heterogeneously doped films, we will not only control the defect concentration using space charge effects but also vary the oxygen ion mobility by strain in one multilayered structure.

Chapter 2

EXPERIMENTAL

2.1 Film Deposition

The oxide thin films were deposited in a multi-target, custom-built reactive magnetron sputtering machine (PVD Products, Wilmington, MA). A schematic diagram of the sputtering system is shown in Figure 12. Single element targets of Zr, Ce, Y, and Gd (ACI Alloys, San Jose, CA) were sputtered in an oxygen-rich environment to create oxidized films. The use of pure metal targets allows the creation of films within a wide range of compositions with significantly simplified experimental operation.

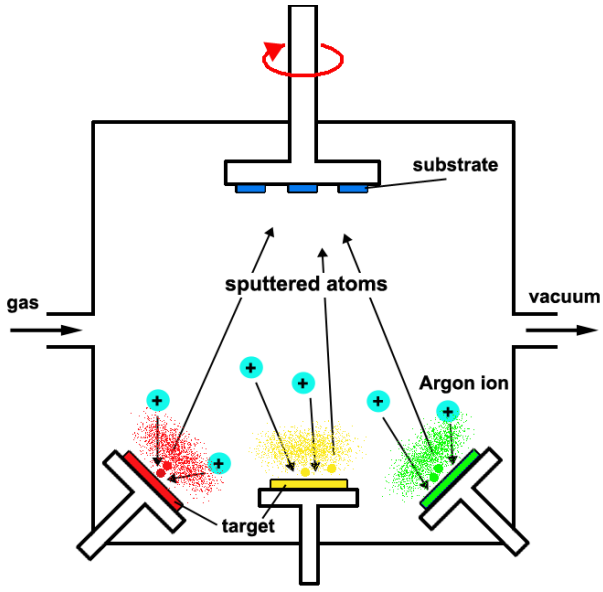

Figure 12 A schematic structure of the sputtering machine.

In the operation of a typical film deposition, the main sputtering chamber was first pumped down to a background pressure of < 1.33×10^{-5} Pa (10^{-7} Torr). After this process, the working gases of argon (Ar) and oxygen (O_2) were introduced into the sputtering chamber. The total working gas flow rate was held constant at 20 sccm with an Ar/O_2 ratio of 9:1 and a working pressure of 1.33 Pa (10 mTorr). Substrates were heated to 650 °C and rotated to create radially uniform films. The deposition rate from each target was adjusted via the sputtering power applied. RF power was used in all cases since the high resistance of an oxidized target surface may extinguish the plasma when using DC power. Single crystal Al_2O_3 (0001) substrates (10 mm × 10 mm × 0.5 mm) were used for the growth of all thin film samples. Although other substrates such as $SrTiO_3$ or Si can provide a much better crystallographic compatibility with YSZ or CeO_2-based films, electrical conduction through the substrates may confuse the interpretation of experimental results [65-68]. The initial growth experiments such as deposition rate calibration were performed on the low-cost Si substrates. The substrate composition was not expected to affect the deposition rate, and the structural and electrical properties of these calibrated films were not of direct interest.

Since the sputtering system used in this study has three RF sputtering guns, a wide range of $Ce_{1-x}Zr_xO_2$, $Zr_{1-z}D_zO_{2-z/2}$, and $Ce_{1-z}D_zO_{2-z/2}$ (D = Y, Gd, or La) films can be deposited. In order to obtain these films with any desired composition and thickness, the first step was to calibrate the deposition rate of the individual, nominally pure films of ZrO_2, CeO_2, Y_2O_3, Gd_2O_3, and La_2O_3. A sharp step between the film and the substrate plane was formed during the sputtering through a partial mask of the substrate using correction fluid. The mask was removed in an ultrasonic bath with acetone after deposition. Then, the substrate was reloaded into the sputtering chamber

and uniformly coated with another layer of reflective titanium (Ti) film over the entire step. The film thickness was obtained by measuring the corresponding step height using a commercial scanning white light interferometer (Veeco Wyko NT9100, Plainview, NY). The deposition rate for each oxide film was then calculated by dividing the total deposited film thickness by the sputtering time. Figure 13 shows the individual deposition rates of ZrO_2, CeO_2, Y_2O_3, and Gd_2O_3 films as a function of sputtering powers.

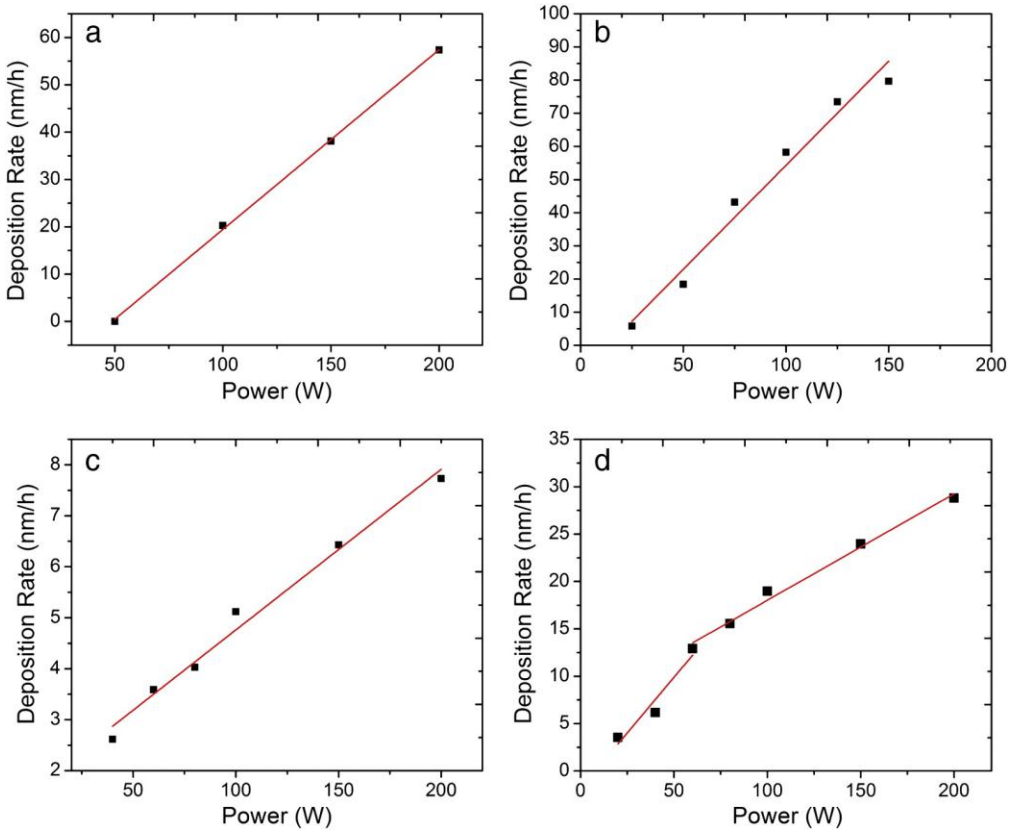

Figure 13 Deposition rates of (a) ZrO_2, (b) CeO_2, (c) Y_2O_3, and (d) Gd_2O_3 thin films as a function of the sputtering power. Reprinted from Ref. [71].

As shown in Figure 13, a very good linear relationship between sputtering power and deposition rate was found in the deposition of ZrO_2, CeO_2, and Y_2O_3 films, but for the Gd_2O_3 films, a reduced sputtering rate was consistently found at low powers. Thus, two linear fits were used to fit the deposition rates of Gd_2O_3 at low ($\leq$ 60 W) and high ($\geq$ 60 W) sputtering powers. Since the deposition rate is dependent on the atomic mass of target and binging energy of the surface target atom, even under the identical sputtering conditions, the deposition rates for different sputtering targets were vastly different. For example, a maximum deposition rate of CeO_2 was $\approx$ 83 nm/hour at 150 W, while for Y_2O_3, it was $\approx$ 9 nm/hour at 200 W. The much lower deposition rate of the dopant materials (e.g., Y_2O_3 and Gd_2O_3) relative to the hosts (e.g., ZrO_2 and CeO_2) fortunately helped to create a wide range of doped films with desired low dopant concentration.

Multi-element films ($Ce_{1-x}Zr_xO_2$, $Zr_{1-z}D_zO_{2-z/2}$, and $Ce_{1-z}D_zO_{2-z/2}$) were produced by simultaneously sputtering from multiple target materials. For example, the films of $Zr_{1-z}Y_zO_{2-z/2}$ were obtained by co-sputtering the targets of Zr and Y at the same time. The expected compositional ratios were varied by adjusting the sputtering powers of targets based on the previous deposition rate calibration results. For a film composed of two elements, the expected atomic ratio can be related to their deposition rates based on the equation:

$$Expected\ atomic\ ratio = \text{Deposition rate ratio} \times \frac{\text{Density ratio}}{\text{Molar mass ratio}} \quad (9)$$

in which reference values for the densities of the bulk oxides were used. In most cases, there existed a deviation between the expected atomic ratio derived from Equation (9) and the actual atomic ratio measured on the co-deposited films. A further calibration of the co-deposited films, therefore, was still necessary. For each deposition, both the

deposition rate and the elemental composition of the co-deposited films were quantified. Figure 14 shows the relationship between expected atomic ratio and the actual atomic ratio in the deposition of YSZ, GDC, and CZO films. By comparing the expected and measured results, the related sputtering parameters were further adjusted.

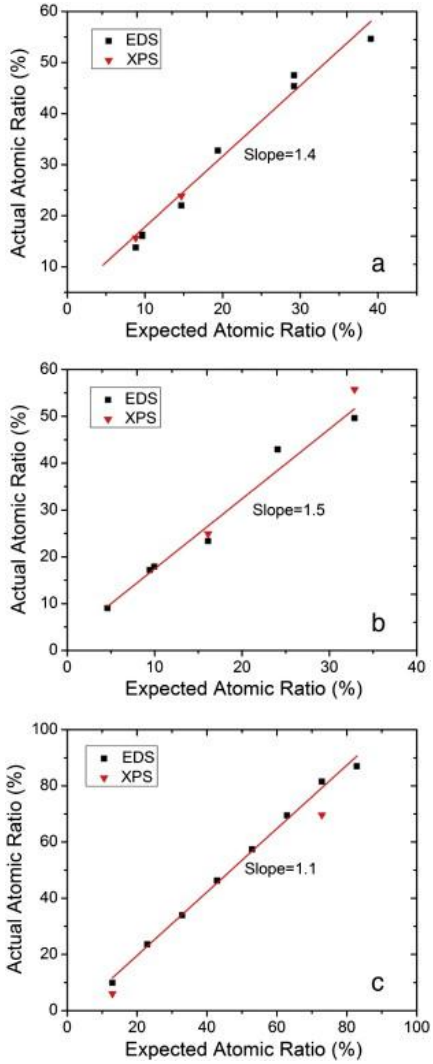

Figure 14 The relationship between the expected atomic ratio and the actual atomic ratio in deposition of (a) YSZ, (b) GDC, and (c) CZO. Note that EDS represents energy dispersive X-ray spectrometry and XPS denotes X-ray photoelectron spectroscopy. Reprinted from Ref. [71].

Multilayered thin films were deposited using the layer control module in the sputtering system. Under the identical deposition condition, different layers with different thickness and composition were sputtered sequentially using a computerized program that controlled the power applied to each target and/or the toggling of desired target shutters.

2.2 Structural and Chemical Characterization

2.2.1 X-ray Photoelectron Spectroscopy

The surface chemical compositions of the films were measured by a Perkin Elmer 5400 X-ray photoelectron spectroscopy (XPS) system with an X-ray source emitting at 1253.6 eV. XPS measurements correspond to the elemental composition of the sample surface down to at most about 5 nm [77]. A pass energy of 89.45 eV was applied in the survey scans, while for high resolution scans, it was 35.75 eV. The obtained spectra were deconvoluted using XPSPEAK 4.1 software.

2.2.2 Energy Dispersive X-Ray Spectrometry

The elemental compositions in the deposited films were also quantified by energy dispersive X-ray spectroscopy (EDX or EDS, JSM-7400F). The accelerating voltage for the measurements was kept at 9 kV. Compared to the XPS measurement, EDX generally can analyze the concentration of elements by sampling the thickness of film up to 1 μm. If the film thickness is less than 1 μm, characteristic X-rays of the elements from the substrate would also be detected. EDX has little capability of measuring the concentration of elements as a function of thickness.

2.2.3 Secondary Ion Mass Spectrometry

The depth-dependent cation compositions of the films were measured using depth-profiling time-of-flight secondary ion mass spectrometry (ToF-SIMS) on a ToF-SIMS IV system (ION-TOF GmbH; Münster, Germany). Material removal was carried out by sputtering with a Cs^+ beam at 5 kV with ion current of 20 nA over a rastered area of 500 μm × 500 μm. A 25 kV Bi^+ beam operated in a "high-current bunched mode" was applied to analyze over a central region with rastered area of 150 μm × 150 μm. The depth profile was obtained in a non-interlaced mode in which the sputtering beam operated for 1 second and then paused for 0.5 second before operating the Bi^+ analysis beam and then repeating this cycle. Since the samples are relatively nonconductive, an electron flood gun provided charge compensation.

2.2.4 X-ray Diffraction

X-ray diffraction (XRD) was performed to determine the orientations of the films and Al_2O_3 substrates by using a Philips X'Pert diffractometer with Cu Kα radiation (λ = 1.5418 Å). Typical θ-2θ geometry was utilized for all sample measurements. The XRD scan was carried out with 0.02°/step and 2 sec/step.

2.2.5 Transmission Electron Microscopy

A detailed characterization of the microstructure and defect nature of the multilayered films was performed by a transmission electron microscopy (TEM) (JEOL JEM-2010F) with 1.0 Å lattice resolution. Bright and dark field images were obtained to visualize and verify that the desired structures were created. Compared to the XRD measurements, one of the biggest challenges in TEM measurements is the sample preparation. The measured sample must be electron transparent with a thickness required at around 100 nm. Focused ion beam/scanning electron microscopy

(Zeiss AURIGA 60 FIB-SEM) was utilized to prepare the cross-sectional TEM samples.

2.3 Microscale Electrode Fabrication

Platinum interdigitated electrodes were fabricated on the top surface of the films for conductivity measurement. The electrodes, illustrated in Figure 15, were laterally spaced by 100 μm with a total perimeter length of about 115 mm.

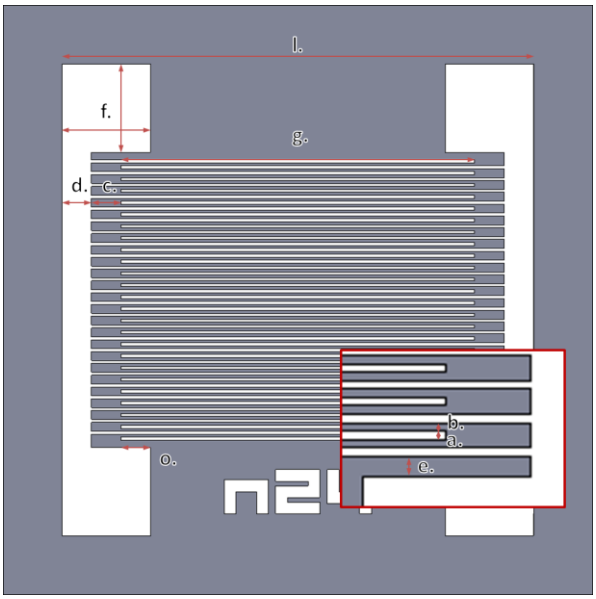

Figure 15 Platinum interdigitated electrode pattern. The width and the inter-space of the electrodes were both kept at 100 μm. The total perimeter length of the electrode was ≈ 115 mm.

Lift-off photolithography was employed to produce the interdigitated photoresist patterns. The first step was to clean the samples using acetone, isopropanol,

and deionized water. This step was very important since possible microscale dusts and/or other contaminations might cause short circuit or open circuit of the fabricated electrodes. After this, a thin layer of photoresist (AZ9260, AZ Electronic Materials) was spin-coated on the surface of the sample with a speed of 4000 rpm for 1 minute. The resultant layer thickness of the photoresist was close to 7 μm. After the spin coating, the sample was baked at 110 °C for 3 minutes in order to solidify the photoresist. Next, the sample was exposed by UV light with an intensity of 9.3 mJ/s for 40 seconds. The interdigitated photoresist pattern was obtained by soaking the sample into the solution of AZ400K (AZ Electronic Materials): H_2O (3:1) for 3 minutes. The sample was then put into the sputtering machine and deposited with a layer of Pt thin film. The power used for sputtering was 50 W and the working gas pressure was 10 mTorr (1.33 Pa) with pure Ar as the working gas. The deposited Pt thin film thickness was ≈ 200 nm. The interdigitated Pt electrode was finally formed by soaking the sample into the acetone to remove the photoresist.

Two possible issues can complicate the ability to quantify the conductivity of a thin film using electrodes placed on the top surface. The first regards the relative resistance of the current path through the film relative to the substrate, which has much lower conductivity but much greater thickness. To ensure that the film and not the substrate properties were being measured, we carried out measurement of the impedance of nominally identical electrode placed directly on bare Al_2O_3 substrate. The resistances measured were larger than those of the samples reported here by more than one order of magnitude. A second possible issue regards whether the current path proceeded through the entire thickness of the film or remained confined to the top surface layer. The lateral conduction path length between the electrodes was 100 μm,

whereas the total thickness of the films studied here was below 300 nm. Thus, current can quickly penetrate under the electrode to the entire film thickness. We have measured the electrical conductivity of multilayers composed of YSZ and CeO_2 in the following section, the conductivity was constant when decreasing the individual layer thickness, which strongly indicated that this kind of conductivity measurement is not just of the exterior layer.

2.4 Electrochemical Characterization

The electrical resistance of the deposited films was measured by electrochemical impedance spectroscopy (EIS) using a Novocontrol Alpha-A analyzer with ZG-4 interface. The total resistance in a measurement of a solid electrolyte is normally due to the charge transport through the grains and the grain boundaries, and the electrochemical reactions at the electrodes. One of the major issues related to the traditional DC measurement technique is that it generally cannot deconvolute each of these contributions to the total measured resistance. On the other hand, impedance spectroscopy is an AC measurement technique. Different charge transport processes can be deconvoluted by examining the electrical response function in the frequency domain, since each of the processes typically has a different time constant. Figure 16 shows a typical impedance spectrum of a ceramic solid electrolyte. Three different semicircles are identified. The first two semicircles located at higher frequency typically represent the impedance of charge transport through the electrolyte grains and grain boundaries, respectively. The third semicircle located at lower frequency is the impedance from electrode polarization. For nanocrystalline thin films, the two high frequency semicircles normally are overlapped and it is difficult to distinguish the ionic conduction through the grains and grain boundaries [78].

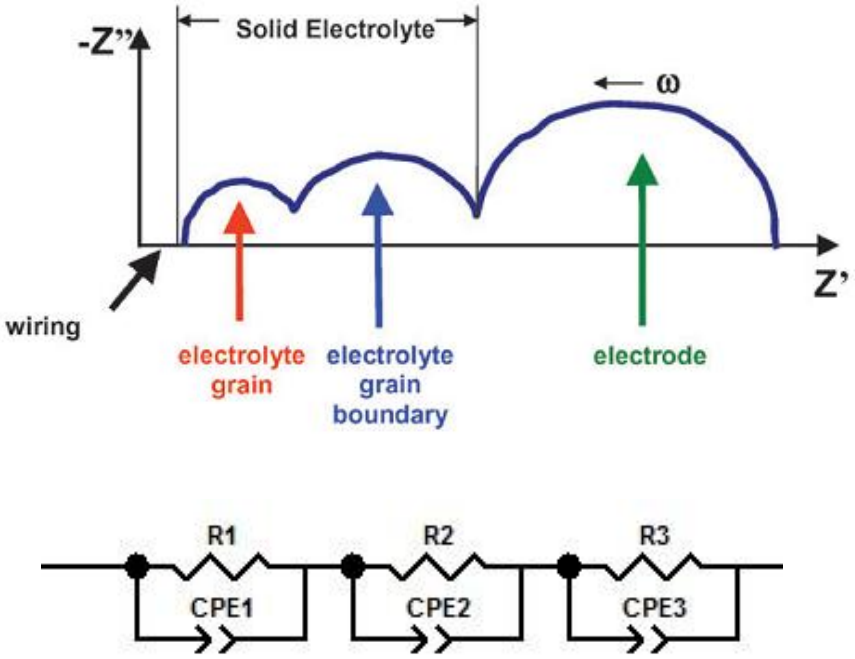

Figure 16 A typical impedance spectrum of a ceramic solid electrolyte fitted by an equivalent circuit composed of three R-CPE elements connected in series. Reprinted from Ref. [79].

The impedance measurement in this work was carried out in a Thermo Scientific Thermolyne single zone split–tube 1200 °C furnace. The sample was fixed in a home-built quartz holder, as shown in Figure 17. Pt wires were used as the connecting wires. A thermocouple was inserted into the furnace and located just below the sample holder to measure the actual sample temperature. Electrical measurements were carried out at temperatures between 300 °C and 650 °C. The signal voltage was 10 mV with no bias applied, and the frequency range was between 1 Hz and 3 MHz. An impedance spectrum was collected every 50 °C from 650 ° down to 300 °C till the

impedance value was relatively stable at each temperature measurement point. After this, the impedance data would be used to calculate the electrical conductivity of the sample. Measurements were typically performed in air, though additional measurements were performed at oxygen partial pressures between 10^{-3} atm and 1 atm using premixed Ar-O_2 mixes.

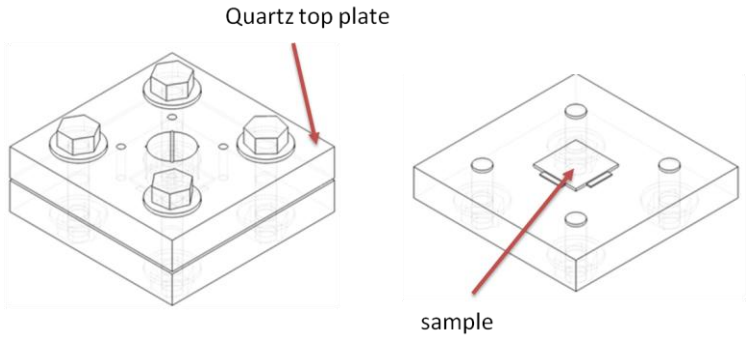

Figure 17 A schematic structure of the home-built quartz sample holder.

Equivalent circuit analysis was performed using Zview software (Version 3.3) to fit the corresponding impedance spectrum. Generally, any physical processes which give a resistance normally have some capacitive mechanism in parallel or at least a stray capacitance between the electrodes. For the impedance spectrum shown in Figure 16, three R (resistance)-CPE (constant phase element) connected in series formed the equivalent circuit to fit the corresponding spectrum. The CPE element that in the equivalent circuit is defined as

$$Z_{CPE}(\omega) = A(i\omega)^{-\alpha} \tag{10}$$

in which Z represents the impedance of CPE which depends on the frequency, ω; A is a scalar value, and α determines the response characteristic [80]. It can be seen from

the equation that when $\alpha = 0$, the CPE is reduced to an ideal resistor, an ideal capacitor when $\alpha = 1$, and an ideal inductor when $\alpha = -1$. The CPE elements have been widely used to represent the noon-ideal capacitors in the equivalent circuit with α ranged between ≈ 0.8 and ≈ 1 [81]. The capacitance corresponding to the lateral conduction through a thin film on an insulating substrate (the case in this work) is immeasurably low and is typically dwarfed by stray capacitances. On the other hand, the electrode polarization terms typically have capacitances that are larger by orders of magnitude [82]. Such large difference in capacitance allows us to clearly deconvolute the contribution from the film and the electrode polarization to the overall impedance.

The electrical conductivity of each film, σ, can be calculated according to

$$\sigma = \frac{w}{R \times (t \times d)} \tag{11}$$

where R is the resistance of the film determined from the equivalent circuit fit to the impedance data, w (= 100 μm) is the distance between each pair of the interdigitated electrode fingers, t (≈ 115 mm) is the total perimeter length of the interdigitated electrode, and d represents the thickness of the conducting film.

Chapter 3

RESULTS

3.1 Structure Characterization of CeO_2-ZrO_2 Solid Solutions

Determining the maximum concentration of Zr in $Ce_{1-x}Zr_xO_2$ (CZO) at which a phase transition from cubic to tetragonal occurs is very difficult to distinguish. A few studies have been carried out to investigate the effect of composition on the crystal structure of CZO, but the reported Zr content at which a tetragonal phase emerged varied. Kuhn et al. obtained a pure cubic phase in CZO only at a Zr content of $x \leq 0.2$ [75], while Zhang et al. identified a transition from cubic to tetragonal phase at $x = 0.3$ [83]. A single cubic phase was persistently observed by Hori et al. [84]and Fu et al. [85] at Zr content up to $x = 0.5$. Conventional ceramic-processed techniques such as sol-gel, solid-state reaction, precipitation were always used to prepare the CZO solid solutions in those studies [75, 83-85]. No literature exists that examines the influence of the Zr content on the cubic phase stability in CZO thin films with nanoscale thickness. In order to determine the range of Ce/Zr atomic ratio for CZO thin films in which a cubic phase is maintained, four different CZO films with thicknesses of ≈ 105 nm and with composition ranging from $x = 0$ to $x = 0.65$ were prepared on Al_2O_3 (0001) substrates.

The θ-2θ XRD patterns of these CZO thin films are shown in Figure 18. Films of $Ce_{0.70}Zr_{0.30}O_2$ (CZO30) and $Ce_{0.55}Zr_{0.45}O_2$ (CZO45) exhibit similar XRD peaks with that of pure CeO_2 thin film. The peak positions of (111) and (100) are shifted to the larger 2θ values, indicating smaller lattice parameters as the content of Zr was

increased. This result is expected since the atomic radius of Zr^{4+} (0.84 Å) is smaller compared to that of Ce^{4+} (0.97 Å) [85]. There are no obvious diffraction peaks that characterize the existence of tetragonal zirconia phase observed for CZO30 and CZO45, indicating that cubic phase was dominant in these films. On the other hand, two separated small peaks located at 34.3˚and 34.8˚appear in the XRD pattern of CZO65 thin film. This finding was similar to what was found in traditional processed CZO75 [84], in which the peak with $2\theta \approx 34.8^{\circ}$ was attributed to the tetragonal ZrO_2 phase. In this work, only the CZO solid solutions with Zr content $x < 0.5$ would be used.

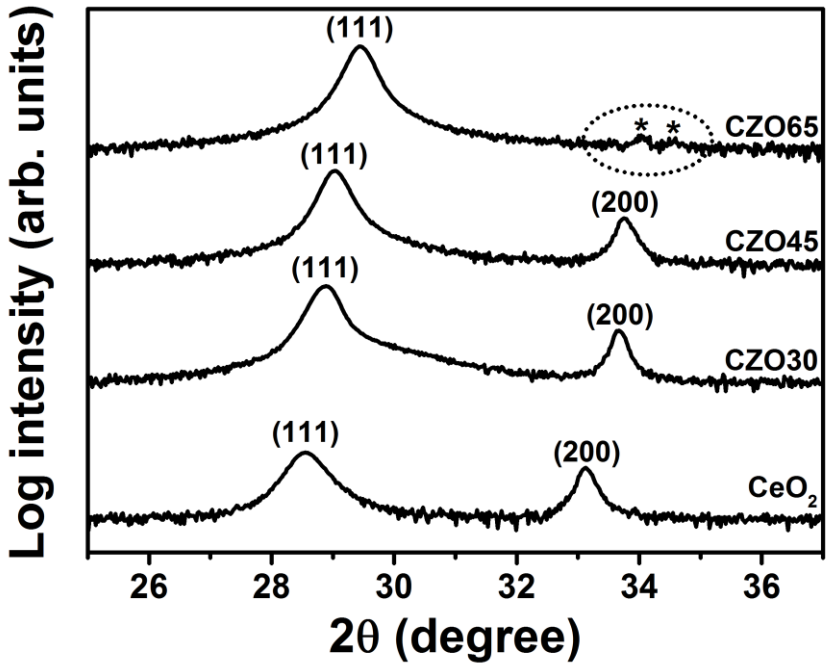

Figure 18 XRD patterns of $Ce_{1-x}Zr_xO_2$ thin films with Zr content of $0 \leq x \leq 0.65$ deposited on Al_2O_3 (0001) substrates. Note that the intensity scale is logarithmic.

3.2 Compressive Strain Effect on Oxygen Ion Conduction in CeO_2

Multilayers composed of $Ce_{0.90}Y_{0.10}O_{2-\delta}$ (YDC) and CZO were prepared in order to quantify the effect of biaxial compressive strain on oxygen ion conduction. Three different types of multilayers composed of YDC with CeO_2, with $Ce_{0.70}Zr_{0.30}O_2$ (CZO30), or with $Ce_{0.55}Zr_{0.45}O_2$ (CZO45), were prepared on Al_2O_3 (0001) substrates. Since the atomic radius of Y^{3+} is relatively similar to that of Ce^{4+} [86], the lattice parameter of YDC with low concentration of Y-dopants is nearly the same as that of pure CeO_2 (≈ 5.41 Å). A value of ≈ 5.408 Å was estimated by Hayashi et al. for $Ce_{0.90}Y_{0.10}O_{2-\delta}$ using molecular dynamics calculations [87]. The interfacial lattice mismatch between YDC and CeO_2 can thus likely be neglected.

The lattice parameter of CZO is linearly dependent on the Zr content according to the Vegard's law [72]. The lattice parameters of CZO45 and CZO30 solid solutions can be estimated as 5.29 Å and 5.33 Å, respectively if we used the lattice parameters of cubic ZrO_2 to be 5.14 Å and pure CeO_2 to be 5.41 Å. Since the lattice parameters of these CZO solid solutions were all smaller compared to that of YDC, an in-plane compressive strain was ostensibly induced in YDC layers near the interfaces in YDC/CZO multilayers. The two constituent materials YDC and CZO have very closely related lattice symmetry, so the lattice mismatch of YDC relative to CZO at the interfaces can be calculated based on the Equation (7). The interfacial lattice mismatch is approximately -2.2% for YDC/CZO45 and -1.5% for YDC/CZO30 interfaces. The negative sign indicates an in-plane compressive strain was expected to be induced in the YDC layers. If the Young's moduli of YDC and CZO are presumed to be comparable, and thus one may assume that the lattice mismatch was borne as equal parts tensile strain in the CZO layer and compressive strain in the YDC layer.

CeO_2-based materials often exhibit polycrystalline structure on Al_2O_3 due to the large lattice mismatch between substrate and film [88, 89]. On the other hand, YSZ thin films have been reported to exhibit (111) texture and nearly epitaxial growth on c-plane Al_2O_3 (0001) substrates [90]. In order to obtain highly textured multilayered films in this work, a 5 nm-thick YSZ buffer layer was placed on the Al_2O_3 substrates. The layered structure of the multilayers can be described as

$$Al_2O_3\text{—YSZ (5 nm-thick)—CZO—(YDC—CZO)} \times N$$

in which N represents the number of YDC/CZO bilayers. The total film thickness above the 5 nm-thick YSZ layer was constant at 105 nm, as illustrated in Figure 19, decreasing the individual layer thickness as needed to increase N. From Figure 19, we can also see that each YDC layer was sandwiched between two CZO layers, ensuring that only the YDC/CZO interfaces (and not a substrate or air interface) would affect the measured oxygen ion conductivity. For each of the three sets of multilayers, several different samples were prepared, as described in Table 2.

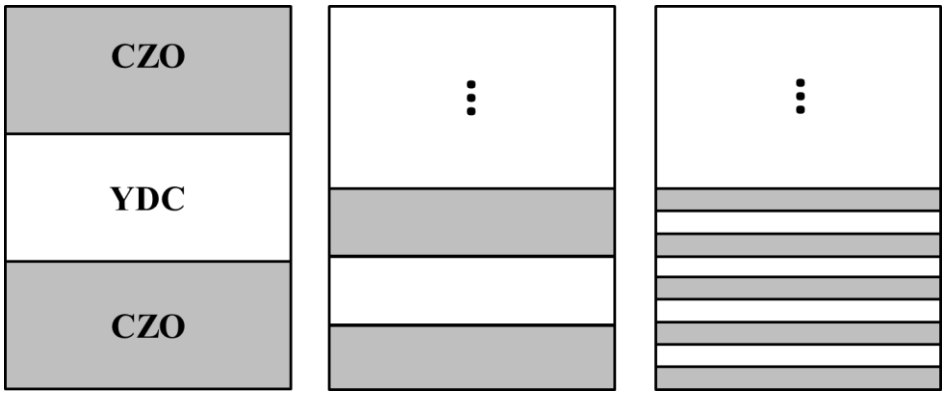

Figure 19 Schematic diagram of the multilayered structures composed of alternating layers of YDC and CZO.

Table 2 Configuration of the samples within each of the three sets of YDC/CZO multilayers.

Sample	CZO layer thickness (nm)	YDC layer thickness (nm)	Number of bilayers (N)	YDC/CZO45	YDC/CZO30	YDC/CeO_2
N = 1	35	35	1	√	√	√
N = 2	21	21	2	√		
N = 3	15	15	3	√	√	√
N = 7	7	7	7	√		
N = 10	5	5	10	√	√	√

Figure 20(a) shows the θ-2θ XRD patterns of YDC/CZO45 multilayers. All of the multilayers display only (111) texture. For $N = 1$, two separate peaks corresponding to the reflections from (111) planes of YDC and CZO45 were identified. The (111) diffraction peak of YDC is located at lower 2θ because of its larger lattice parameter compared to that of CZO45. As the number of bilayers was increased, the two peaks of (111) YDC and (111) CZO45 began to overlap, resulting in the superlattice patterns for $N = 3$ and $N = 7$. The superlattice patterns are composed of an average structure peak SL_0 surrounded by two first-order satellite peaks, SL_{-1} and SL_{+1}. For $N = 10$, where the YDC and CZO layers were 5 nm thick, the diffraction pattern consists almost entirely of a single peak at $2\theta \approx 28.5°$, indicating that the film has largely adopted a single out-of-plane lattice parameter of ≈ 5.43 Å. Thus, the lattice mismatch in this structure has effectively biaxially compressed the YDC (and dilated the CZO). The XRD pattern of YDC/CZO30, as shown in Figure 20(b), also exhibits superlattice effects subsiding to a single peak when the number of bilayers was increased. Figure 20(c) shows the XRD patterns of YDC/CeO_2 multilayers. Due

to the similarity of the lattice parameters of YDC and CeO_2, it was hard to distinguish any peak separation of the (111) diffraction planes.

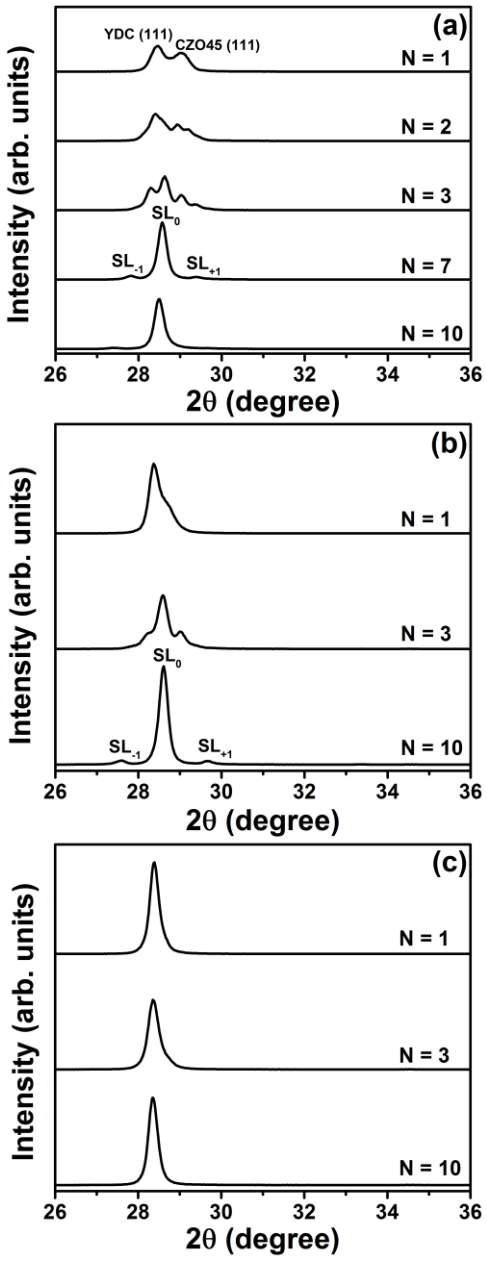

Figure 20 Typical θ-2θ XRD patterns of multilayers composed of (a) YDC with CZO45, (b) YDC with CZO30, and (c) YDC with CeO_2 deposited on Al_2O_3 (0001) substrates. *N* indicates the number of YDC/CZO bilayers.

The appearance of sharp, well-defined satellite peaks indicates the formation of high-quality interfaces between the adjacent layers [55]. The locations of the satellites peaks in XRD patterns can be used to calculate the bilayer thickness according to

$$\Lambda = \frac{\lambda_{Cu}}{\sin\theta_{+1} - \sin\theta_{-1}} \tag{12}$$

in which Λ represents the thickness of a bilayer, λ_{Cu} is the wavelength of Cu Kα radiation (1.5418 Å), θ_{+1} and θ_{-1} are the angular positions of satellite peaks SL_{+1} and SL_{-1}, respectively [55]. The bilayer thickness of YDC/CZO45 and YDC/CZO30 multilayers for $N = 10$ were calculated from the peak locations to be 8.3 nm and 8.8 nm, respectively, similar to the 9.9 nm and 9.7 nm calculated from the total film thickness as measured by an optical interferometer.

The impedance spectra of all the multilayers exhibited two main features composed of two semicircles located at high and low frequencies, as shown in Figure 21(a). The equivalent circuit inset in the figure was used to fit the corresponding impedance spectrum at each temperature. The equivalent capacitance of the constant phase element for the high frequency semicircle, CPE1, was of order 10^{-11} F, while a much larger equivalent capacitance value of $> 10^{-7}$ F was obtained for that of the low frequency semicircle, CPE2. Such large difference in capacitance allowed clear determination that the high frequency semicircle was due to the ionic conduction through the electrolyte, while the low frequency semicircle was due to electrode polarization. The R_{YSZ} element represents the electrical resistance of the 5 nm-thick YSZ buffer layer which calculated based on the electrode geometry and the conductivity value obtained from Ref. [90] for a 100-nm thick YSZ film with the same dopant concentration. The value of R_{YSZ} was always at least one order of magnitude

larger than that of R1. Resistance R1, therefore, represents the electrical resistance of the electrolyte eliminating the small contribution from the YSZ buffer layer.

The electrical conductivity of pure CeO_2 at 650 °C is normally of order 10^{-3} S/cm [91], which is at least one order of magnitude less compared to that of YDC thin films. By adding ZrO_2 into CeO_2 to form CZO solid solution, the conductivity is further decreased due to reduced vacancy mobility [92]. The contribution from the parallel CZO layers to the total electrical conductivity of the multilayers discussed here was negligible, with a parallel resistance that was, like the YSZ buffer layer, always at least one order of magnitude larger than that of the YDC layers. The total electrical conductivity of the multilayers was calculated based on the resistance R1 and the total thickness of the YDC layers within the multilayer based on Equation (11).

Figure 21(b) shows the Arrhenius plots of the electrical conductivity measured for YDC/CZO45 multilayers in air. The conductivity of a single-layer YDC thin film (195 nm-thick) was also included for comparison. The out-of-plane lattice parameter for this single-layer YDC thin film was calculated to be about 5.409 Å based on the (111) XRD diffraction peak. This value is similar to what was found by Hayashi et al. for bulk YDC with the same Y-dopant concentration [87]. The YDC single-layer film was fully relaxed due to the relatively large thickness. Any possible strain effect caused by the lattice mismatch with the substrate can be safely excluded. From Figure 21(b), it can be seen that the electrical conductivity of YDC/CZO45 multilayers monotonically decreased by almost one order of magnitude as the number of bilayers increased from $N = 1$ to 10. At the same time, the activation energy increased from 0.84 eV to 0.95 eV.

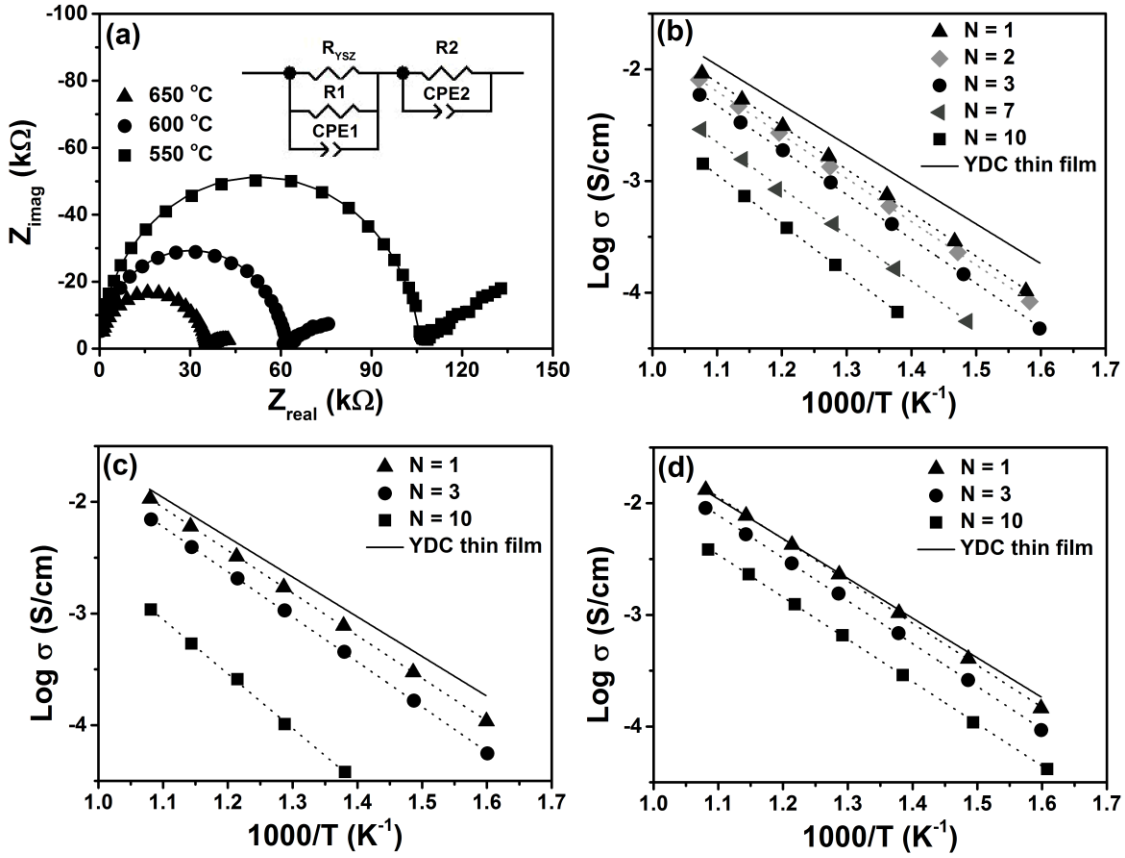

Figure 21 (a) Impedance spectra of YDC/CZO45 multilayer with $N = 1$ at the temperatures indicated and the equivalent circuit used to fit the data (R_{YSZ} was a fixed value at each temperature), and Arrhenius plots of the electrical conductivities of the YDC layers within multilayers composed of (b) YDC/CZO45, (c) YDC/CZO30, and (d) YDC/CeO_2. The YDC thin film data came from measurements of a single layer film with thickness ≈ 195 nm.

Figure 21(c) show similar trends of reduced electrical conductivity with increasing number of bilayers for the YDC/CZO30. In general, the conductivity of the YDC decreased as the interfacial density and/or the lattice mismatch increased. The

lone exception to this rule is that for $N = 10$, with individual layer thickness of ≈ 5 nm, the conductivity of the YDC/CZO30 was slightly smaller compared to that of YDC/CZO45. The electrical conductivity of the YDC/CeO_2 multilayers, as shown in Figure 21(d), decreased as the number of bilayers increased, despite near-zero strain in the multilayers. The mechanism of this effect was either interfacial roughness or substrate-related effects. At $N = 10$, the layers were only 5 nm thick, and thus even 1 nm interfacial roughness could lead to significant current constriction at the thinnest areas. Alternatively, this slight decrease in conductivity may be due to the $N = 3$ and $N = 10$ multilayers placing more YDC layers in closer proximity to the YSZ buffer layer and substrate beneath. The YSZ buffer layer or the Al_2O_3 substrate, which possess smaller lattice parameters than that of YDC, may also compressively strain the YDC layers which stayed close to them.

3.3 Tensile Strain Effect on Oxygen Ion Conduction in ZrO_2

The second type of multilayers composed of 9 mol% YSZ and CZO have been fabricated to study the ability to create tensile strain in YSZ-based multilayers. Here, we used highly analogous experimentation to that of the YDC/CZO multilayers to examine if CZO could be used to create increased ionic conductivity via biaxial tension in neighboring YSZ layers.

Similarly, three different sets of multilayers composed of 9 mol% YSZ with CeO_2, CZO30, or with CZO45, were prepared on Al_2O_3 (0001) substrates. The lattice parameters of CZO30 and CZO45 solid solutions were estimated previously as 5.33Å and 5.29 Å, respectively. Since the lattice parameters of all these CZO solid solutions are all larger compared to that of YSZ (≈ 5.14 Å), an in-plane tensile strain was thus ostensibly induced in YSZ layers near the interfaces in YSZ/CZO multilayers. Based

on the Equation (7), the lattice mismatch of YSZ relative to CZO is approximately +5.2% for YSZ/CeO_2, +3.7% for YSZ/CZO30, and +2.9% for YSZ/CZO45 multilayers. The positive sign indicates an in-plane tensile strain was expected to be induced in the YSZ layers. Based on reported measurements of YSZ and Gd_2O_3 doped CeO_2 [93], the Young's moduli of YSZ and CZO are presumed to be comparable, and thus one may also assume that the lattice mismatch was borne as equal parts compressive strain in the CZO layers and tensile strain in the YSZ layers.

A 5 nm-thick YSZ was also deposited first as a buffer layer in order to create highly textured multilayers. The structure of the multilayered films can be described as

$$Al_2O_3\text{—YSZ (5 nm-thick)—CZO—(YSZ—CZO)} \times N$$

in which N represents the number of YSZ/CZO bilayers. The total film thickness above the 5 nm-thick YSZ layer, similar to Figure 19, was also constant at 105 nm, decreasing the individual layer thicknesses as needed to increase N. For each of the three sets of multilayers, three different samples were prepared, as described in Table 3. Single-layer YSZ, CeO_2, CZO45, and CZO30 thin films with thickness of ≈ 105 nm were also prepared on Al_2O_3 (0001) substrates for comparison.

Table 3 Configuration of the samples within each of the three sets of multilayers.

Sample	CZO layer thickness (nm)	YSZ layer thickness (nm)	Number of bilayers (N)
N =1	35	35	1
N = 3	15	15	3
N = 10	5	5	10

Figure 22(a) shows the XRD patterns of the YSZ/CeO_2 multilayers on Al_2O_3 (0001) substrates. Single-layer YSZ and CeO_2 thin films with thickness of ≈ 105 nm were included for comparison. The single layer CeO_2 thin film exhibits both (111) and (100) orientations, but the single layer YSZ film and all of the YSZ/CeO_2 multilayers (which had the YSZ buffer layer) are highly textured along the (111) direction. The out-of-plane lattice parameters of YSZ and CeO_2 single-layer films calculated from the (111) diffraction locations were 5.21 Å and 5.41 Å, respectively. The lattice parameter of the CeO_2 thin film was almost the same as that of the bulk value, indicating that the film was fully relaxed on the Al_2O_3 substrate. For the single-layer YSZ thin film, the out-of-plane lattice parameter, however, exceeded the bulk value of 5.14 Å, an effect noted previously [90].

For $N = 1$, the multilayer exhibits two separate diffraction peaks representing the diffraction planes of YSZ (111) and CeO_2 (111). The peak locations correspond to out-of-plane lattice parameters of 5.20 Å for YSZ and 5.45 Å for CeO_2. These values represent a very slight reduction in lattice parameter for YSZ (111) and slight dilation for CeO_2 (111). Since these are out-of-plane lattice parameters, this result is consistent with a small' in-plane tensile strain in YSZ and compressive strain in the CeO_2. As the individual layer thickness decreased to 15 nm for the N =3 multilayer, the peak locations did not significantly shift compared to the locations of $N = 1$. A superlattice pattern composed of an average structural peak SL_0 surrounded by two first-order satellite peaks SL_{-1} and SL_{+1} was observed for $N = 10$. The average lattice parameter based on the SL_0 peak was calculated to be 5.33 Å, which is in agreement with the average value of the out-of-plane lattice parameters of YSZ (5.20 Å) and CeO_2 (5.45 Å).

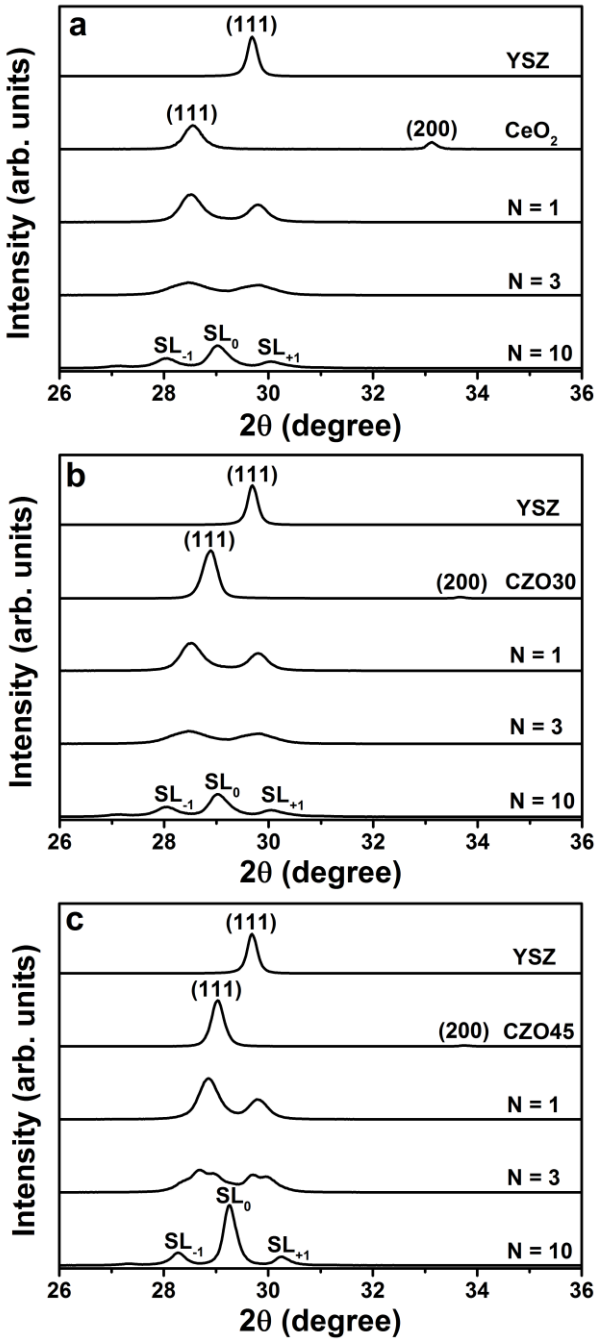

Figure 22 XRD patterns of multilayered thin films composed of *N* bilayers of (a) YSZ and CeO_2, (b) YSZ and CZO30, and (c) YSZ and CZO45. The corresponding single-layer YSZ and CZO thin films deposited on Al_2O_3 (0001) with thickness of ≈ 105 nm were also included for comparison.

Figure 22(b) shows the XRD patterns of the YSZ/CZO30 multilayers. Similar to what was found in the YSZ/CeO_2 multilayers, the multilayer films exhibit (111) texture and transit from two distinct peaks to a superlattice pattern as the individual layer thicknesses decreased to 5 nm. For both the $N = 1$ and $N = 3$ multilayers, the out-of-plane lattice parameters were calculated to be 5.19 Å for YSZ and 5.42 Å for CZO30 (which was an increase from 5.35 Å for the CZO30 single layer film). These values again represent little effective mismatch strain created in the YSZ. For the $N = 10$ multilayer, the average lattice parameter based on the SL_0 peak was calculated to be 5.33 Å, which is again similar to the average value (≈5.31 Å) of the out-of-plane lattice parameters of YSZ and CZO30.

The XRD patterns of the multilayers composed of YSZ and CZO45 is shown in Figure 22(c). For $N = 1$, the out-of-plane lattice parameter for YSZ was calculated to 5.19 Å, the same as that in YSZ/CZO30 multilayer. The lattice parameter of CZO45 in the multilayer film was 5.35 Å, an increase from 5.32 Å as a single-layer film. The two peaks start to transition to a superlattice pattern for the $N = 3$ multilayer. In this sample, the lattice parameter based on the CZO45 peak increased to 5.38 Å, but the value for YSZ remained 5.19 Å. A strong superlattice pattern was found for the $N = 10$ multilayer. The average lattice parameter calculated based on the SL_0 peak was 5.29 Å, which is again similar to the computed average of the lattice parameters of the constituent layers, YSZ and CZO45.

As mentioned before, the appearance of clear and sharp satellite peaks indicates the formation of high-quality, well-defined interfaces between the constituent layers [55]. Nevertheless, the intensity of the SL_0 peak of the YSZ/CeO_2 and the YSZ/CZO30 N=10 multilayers was smaller than that of the corresponding

YSZ/CZO45 multilayer, indicating slightly rougher or otherwise less ideal interfaces where the lattice mismatch is larger. Based on the Equation 12, the bilayer thicknesses of the $N = 10$ multilayers composed of YSZ with CeO_2, CZO30, and CZO45 were calculated to be 8.7 nm, 9.1 nm and 9.2 nm, respectively. These values were very close to the values of 10.4 nm, 10.7 nm, and 10.4 nm calculated from the total film thickness as measured by interferometry and the known number of constituent layers.

The work on multilayers of YDC and CZO found that as the individual layer thickness decreased, a superlattice diffraction pattern appeared and then, upon further thickness reduction to 5 nm, almost gave way to a single, sharp, very high-intensity peak. This indicated that the whole multilayer could be characterized by a single lattice parameter and that the layers were effectively straining each other. Here, two distinct peaks remained for the N=3 multilayers, and a superlattice pattern remained with satellite peaks clearly identified for the N=10 multilayers. These results gave clear indication that two distinct lattice parameters remained even for the thinnest individual layer thickness of 5 nm.

The out-of-plane lattice parameters of the YSZ across all three sets of multilayers were very similar to that of the single-layer film. This finding seems to indicate that the interfacial strains in YSZ layers were largely or fully relaxed. At the same time, the out-of-plane lattice parameters of the CZO slightly increased from the single layer films to the N =1 and N =3 multilayers, indicating an average in-plane compressive strain of roughly -1% existed in the CZO near the interfaces.

Figure 23 shows impedance spectra, from a YSZ/CZO45 (N = 10) multilayer at three different temperatures. The value of R_{YSZ} was fixed at each temperature and calculated based on the electrode geometry and conductivities obtained from a single

layer YSZ thin film (≈ 105 nm). Resistance R_{YSZ} was always at least one order of magnitude greater than R1. The equivalent capacitance of the constant phase element for the high frequency semicircle, CPE1, was also found to be of order 10^{-11} F. The equivalent capacitance value of CPE2 for the low frequency semicircle was at least four orders of magnitude larger, which is much too large to be due to conduction between the electrodes. This result clearly indicates that resistance R1 was due to conduction through the film, while R2 was due to electrode polarization. Due to the small conductivity of the CZO solid solutions, the overall conductivity of the multilayers here was also calculated based on the total thickness of YSZ within the multilayer.

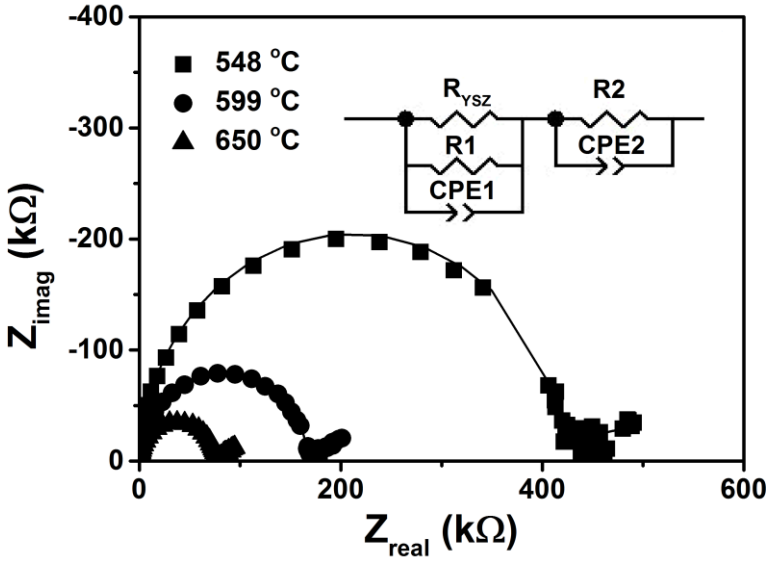

Figure 23 Impedance spectra measured in open air of YSZ/CZO45 multilayers with $N = 10$ at the temperatures indicated. Also shown is the equivalent circuit used to fit the data (R_{YSZ} was a fixed value at each temperature).

Figure 24(a) shows Arrhenius plots of the electrical conductivity of YSZ/CeO_2 multilayers measured in air. The conductivity of a single layer YSZ thin film with thickness of ≈ 105 nm was also included for comparison. From the figure, we can see that the electrical conductivities for $N = 1$ and $N = 3$ have similar values compared to that of the YSZ thin film. The electrical conductivity for $N = 10$, however, was slightly reduced by a factor of ≈ 2. These results compare very well to those reported by Pergolesi et al.[69] on a similar study of multilayers composed of YSZ and CeO_2. In that study, the authors found no change in conductivity of YSZ even with individual layer thickness decreased to 5 nm. The slightly decreased conductivity for $N = 10$ in this work, similar to what was found in our previous study of YDC/CeO_2 multilayers, might be due to non-zero roughness at the interfaces.

Figure 24(b) and (c) show Arrhenius plots of electrical conductivity of the YSZ/CZO30 and YSZ/CZO45 multilayers, respectively. In both cases, as the individual layer thickness decreased from 35 nm ($N = 1$) to 5 nm ($N = 10$), the multilayers exhibit nearly identical conductivities as that of the YSZ single-layer thin film. The decreased interfacial lattice mismatch in these multilayers relative to the YSZ/CeO_2 multilayers seems to increase the interface quality for $N = 10$, resulting in similar conductivities with those of the $N = 1$ and $N = 3$ multilayers.

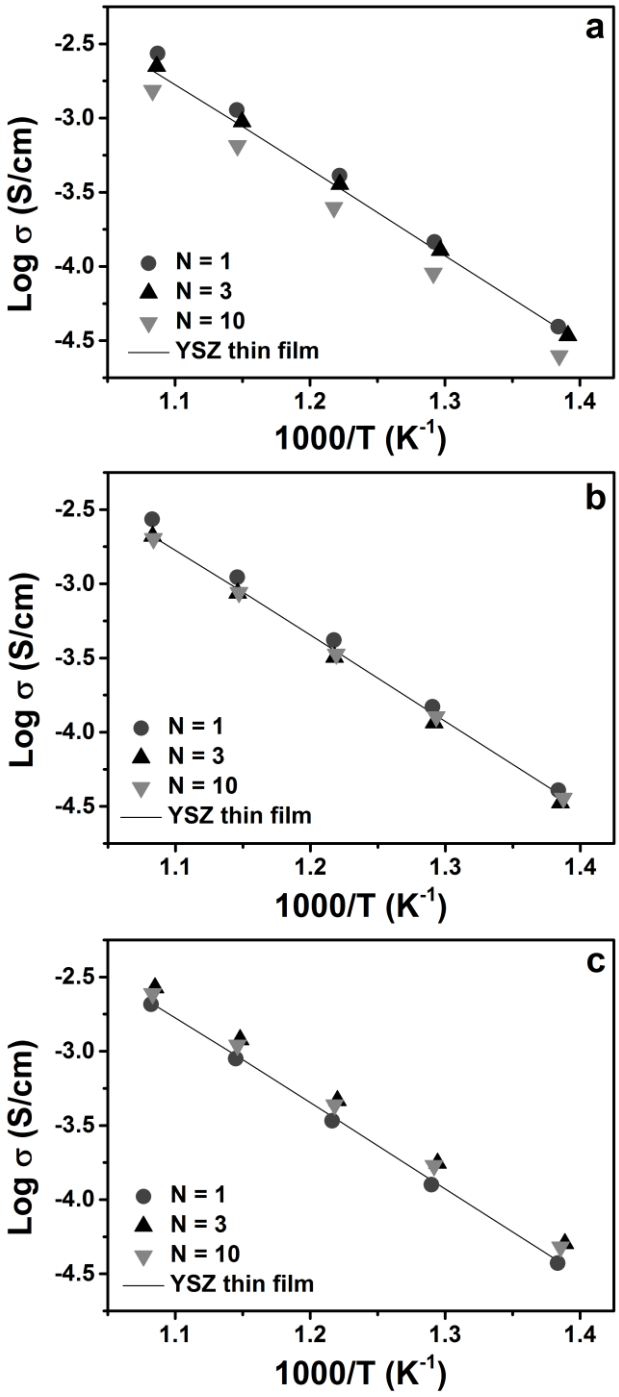

Figure 24 Arrhenius plots of the electrical conductivity of the YSZ layers in the (a) YSZ/CeO_2, (b) YSZ/CZO30, and (c) YSZ/CZO45 multilayers. Shown for comparison is the conductivity measured from a single-layer YSZ film with thickness of ≈ 105 nm.

3.4 Heterogeneously Doped CeO_2 Thin Films

The association between dopants and vacancies has been considered as one of the main reasons for the decreased conductivity at higher dopant concentration. In this work, we created a series of HEMT-like multilayered films and aimed to increase the overall conductivity by trapping oxygen vacancies into the highly-mobile space charge regions of the undoped layers. Heterogeneously doped $Ce_{0.95}Y_{0.05}O_{2-\delta}$ (YDC) films, as shown in Figure 25, were first fabricated to study the effects of interfacial defect redistribution on the oxygen ion conduction behavior. In these films, the Y-dopants were distributed homogeneously or were condensed into increasingly concentrated two-dimensional layers, to the limit of alternating layers of pure CeO_2 and pure Y_2O_3.

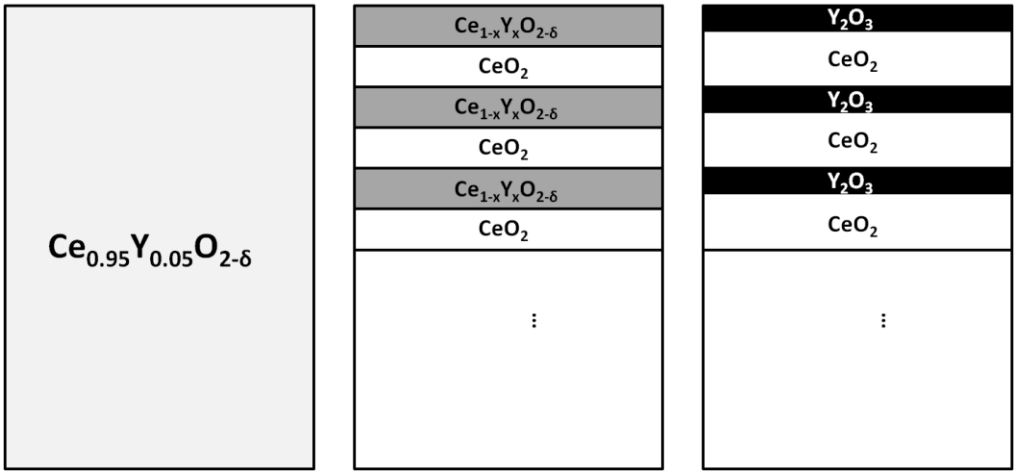

Figure 25 Schematic diagram of the structures of $Ce_{0.95}Y_{0.05}O_{2-\delta}$ films with modulated composition. The Y-dopant concentration z in $Ce_{1-z}Y_zO_{2-z/2}$ layers was gradually increased while keeping the net Y-dopant concentration of the whole film at a constant 5% by adjusting the relative thickness ratio between CeO_2 and Y-containing layers.

The use of CeO_2-based rather than ZrO_2-based materials here was to avoid any issues related to non-cubic phase formation. The total film thickness and the net Y-dopant content were kept constant of 5% so that only the distribution of the dopants within the film was altered. A study using molecular dynamics simulations reported that the activation energy of oxygen ion diffusion in similarly heterodoped YSZ [94] should increase to correspond to the dopant concentration in the doped layer. Structures at the limit of pure Y_2O_3 and pure ZrO_2 layers, where distinctly different behavior would be expected, were not examined.

The compositions of the YDC layers here were characterized by XPS. An example XPS survey spectrum is shown in Figure 26(a) for a YDC film deposited using 150 W for the Ce target and 50 W for the Y target. The only elements that were detected on the surface of film are Ce, Y, O, and C. Since the targets of Ce and Y used in the film deposition were of high purity (> 99.9%), the carbon contaminant was likely to be adventitious. The corresponding Ce3d and Y3d spectra collected at high resolution are shown in Figure 26(b) and (c), respectively. The six peaks located at binding energies of 917.7 eV, 908.8 eV, 902.2 eV, 899.5 eV, 889.9 eV, and 883.9 eV in the Ce3d spectrum are characteristic of tetravalent Ce (IV) [95]. No obvious peaks that characterize Ce (III) could be identified. The relative atomic ratio of Y to Ce was calculated to be about 1:10 based on the peak area under Ce3d and Y3d spectra and their sensitivity factors. Similar XPS spectra were also observed for other YDC films deposited with different sputtering powers of Ce and Y targets.

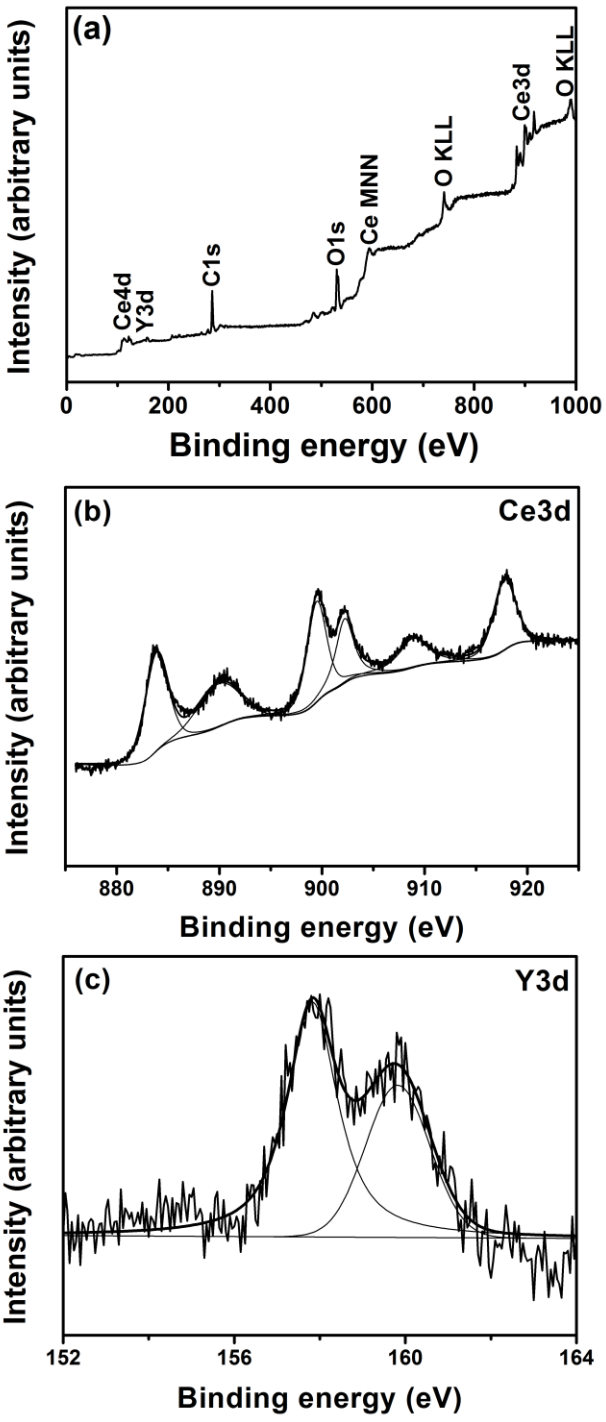

Figure 26 XPS spectra of YDC film sputtered at 150 W/50 W for Ce/Y targets: (a) survey-scan spectrum, (b) high resolution spectrum of Ce3d, and (c) high resolution spectrum of Y3d.

YDC films with the net Y-dopant concentration of 5% were deposited on Al_2O_3 (0001) substrates. The total film thickness of each sample was kept constant at ≈ 200 nm. The Y dopants were distributed either homogeneously or were condensed into increasing concentrated layers, as shown in Figure 25. The net dopant concentration of the whole films was always maintained at 5% by adjusting the relative thickness ratio between YDC and CeO_2 layers. Four different samples were prepared as summarized in Table 4. Sample A has a uniform composition through the thickness, with Ce and Y atoms randomly mixed on the cation sublattice. Sample D, at the other extreme, completely condenses Y dopants into parallel layers, leading to a film structure with ten bilayers (each 20 nm-thick) of alternating 1 nm of pure Y_2O_3 and 19 nm of pure CeO_2 layers. The required thickness ratio of Y_2O_3 to CeO_2 in sample D was derived from

$$\frac{z}{1-z} = 2 \times \frac{L_{Y_2O_3}}{L_{CeO_2}} \times \frac{\rho_{Y_2O_3}}{\rho_{CeO_2}} \times \frac{M_{CeO_2}}{M_{Y_2O_3}} \tag{13}$$

where z is the net Y-dopant concentration in the whole $Ce_{1-z}Y_zO_{2-z/2}$ film, L is the layer thickness, ρ is the density, and M is the molar mass. By substituting $z = 0.05$ and reference values for the densities of the bulk oxides, the thickness ratio between Y_2O_3 and CeO_2 that needs to be satisfied for 5% net dopant concentration was very close to 1:19. Samples of B and C possessed intermediate levels of dopant condensation. For simplicity, here we assume that at relatively lower dopant concentration, the molar volumes of $Ce_{0.90}Y_{0.10}O_{2-\delta}$ and $Ce_{0.80}Y_{0.20}O_{2-\delta}$ were the same as pure CeO_2. Thus, the thickness ratios between YSZ and CeO_2 layers in samples of B and C were considered to be the same as their molar ratios.

Table 4 Configuration of four samples with net composition of $Ce_{0.95}Y_{0.05}O_{2-\delta}$. Other than the homogeneous sample A, each film consists of 10 repeated bilayers of the Y-containing layer and pure CeO_2 layer.

Sample	Measured total film thickness (nm)	Composition of Y-containing layer	Y-containing layer nominal thickness (nm)	Pure CeO_2 layer nominal thickness (nm)
A	197	$Ce_{0.95}Y_{0.05}O_{2-\delta}$	20	0
B	193	$Ce_{0.90}Y_{0.10}O_{2-\delta}$	10	10
C	190	$Ce_{0.80}Y_{0.20}O_{2-\delta}$	5	15
D	196	Y_2O_3	1	19

Figure 27 shows the XRD patterns of samples of A to D deposited on Al_2O_3 (0001) substrates. Due to the large lattice mismatch between CeO_2-based material and the substrate, the films are all oriented along (100) and (111). The (111) and (100) peaks of samples of B and C are not shifted compared to the corresponding peaks of sample A, nor are they split into two peaks related to the lattice spacings for the doped and pure ceria layers. These factors indicate similar lattice parameters for $Ce_{0.95}Y_{0.05}O_{2-\delta}$, $Ce_{0.90}Y_{0.10}O_{2-\delta}$, $Ce_{0.80}Y_{0.20}O_{2-\delta}$, and CeO_2. This is expected, since the atomic radii of Ce^{4+} and Y^{3+} cations are similar to each other [86], resulting in little change in lattice parameter when Ce^{4+} is substituted by Y^{3+}. Pure Y_2O_3 exhibits the cubic bixbyite crystal structure, which can be described as a "pseudo-fluorite" structure with an ordered array of one of every four oxygen site unfilled [96, 97]. The lattice parameter of the bixbyite structure is roughly twice that of fluorite due to the reduced symmetry, but the actual bond lengths and geometry are highly similar. The lattice parameter of Y_2O_3 is ≈ 10.60 Å [97]. Thus, the fluorite-equivalent lattice parameter for Y_2O_3 is ≈ 5.30 Å. Although there is a difference in lattice parameters

between Y_2O_3 and CeO_2 (≈ 5.41 Å), there was also no obvious splitting at the (111) and (100) peaks in sample D. This observation may be attributed to the small amount of Y_2O_3 within sample D.

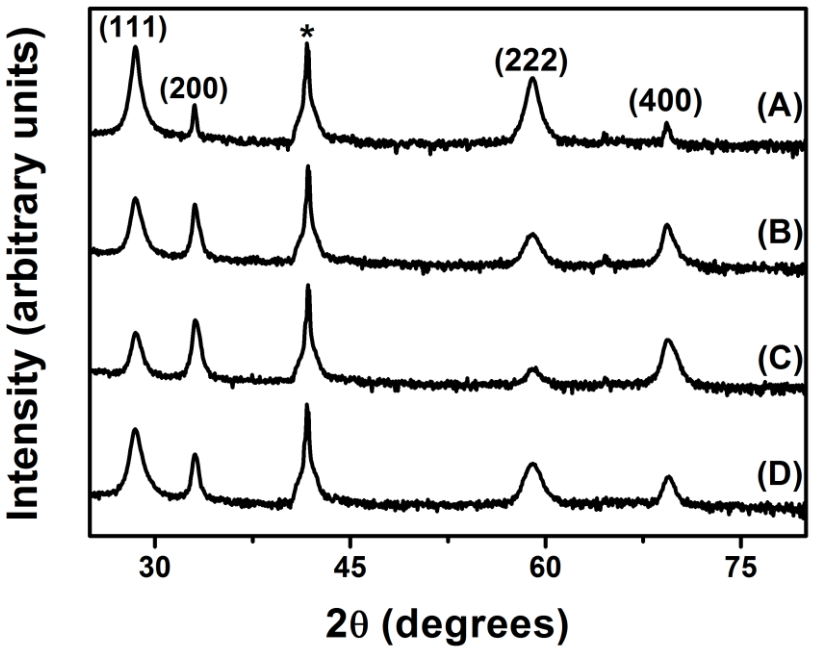

Figure 27 θ-2θ XRD patterns of samples of A to D grown on Al_2O_3 (0001) substrates. The asterisk indicates the substrate peak of Al_2O_3 (0006). Other peak locations were indicated by the Miller indices of the ceria lattice. Note that the intensity scale is logarithmic.

Figure 28 shows the depth dependence of the SIMS signal from the YO^+ fragment through the top three bilayers of samples B, C, and D. YO^+ was chosen since it provided the highest intensity compared to that of Y^+ or other Y-relevant secondary ions. From the figure, it can be seen that all three depth profiles oscillate over a similar period, confirming that the three samples possessed the same 20 nm bilayer thickness.

The widths of the YO^+ peaks narrow and their magnitudes increase from sample B to sample C, and they do so even more for sample D. This result confirms that the Y-dopants were increasingly concentrated within planar layers in these three samples. Still, the limited depth resolution of SIMS prevents certain determination of the confinement of Y_2O_3 to 1 nm layers in sample D.

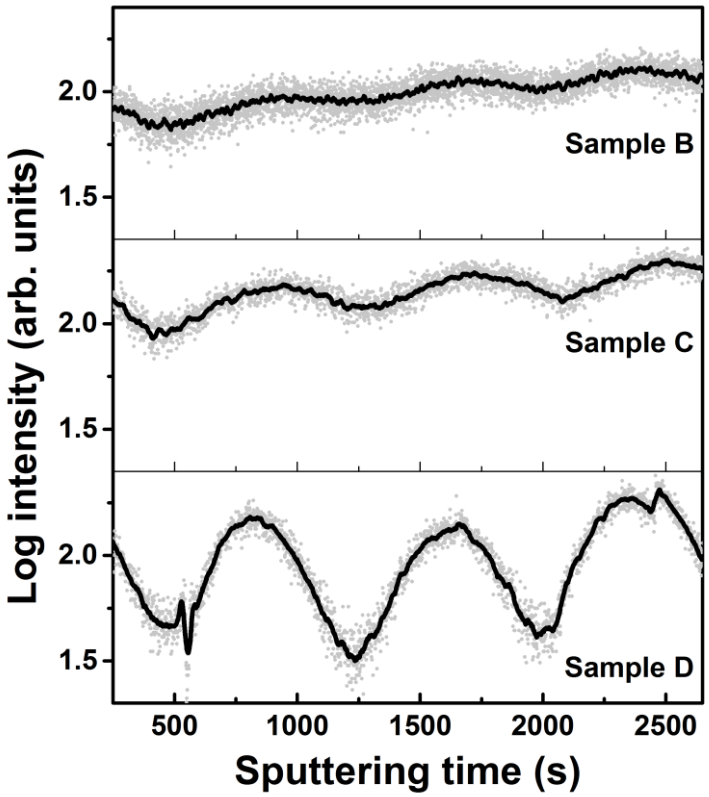

Figure 28 Depth profiles of the YO^+ obtained by TOF-SIMS through the top three bilayers of samples of B, C, and D. Grey points represent the original signal with black lines providing a 50-point moving average. Note that the intensity scale is logarithmic.

A detailed characterization of the compositional variation in sample D was further performed by TEM. Figure 29(a) presents the bright field TEM image of sample D. The thin film was found to be polycrystalline and adopted a columnar microstructure. The total film thickness was estimated to be about 200 nm, which is in good agreement with the previous measurement carried out by optical interferometer. The 10 compositional bilayers can be clearly distinguished within the film. In each bilayer, the thin, relatively bright regions indicate the Y_2O_3, while the thicker, darker areas indicate CeO_2. The thickness of each bilayer was measured to be ≈ 20 nm composed of ≈19 nm of CeO_2 and ≈1 nm of Y_2O_3. As evidenced by the misoriented grain in the right-central portion of the image, the bilayers follow the growth direction even where the growth was at a slight angle to the substrate interface. Other grains with as high of a misorientation angle could not be found during the microscopy. Nevertheless, any amount of misorientation provides further explanation for the relatively low depth resolution in the SIMS measurements. This result confirms that compositional modulation through the thickness at a single nanometer scale was achieved, albeit with a very small degree of non-planarity. Figure 29(b) shows high-resolution TEM (HR-TEM) of the same film. The (111) and (100) lattice planes (as determined by the previous XRD measurement) are roughly parallel with the substrate surface. The crystal structure is continuous across the compositional layers. Since the crystal structure of CeO_2 and Y_2O_3 are similar, the interfaces between the "layers" of this film were difficult to find and/or devoid of any distinguishing structure features, in particular because the layers were so thin.

Compositional modulations are likely to be metastable; however, the diffusion of Y dopants into neighboring undoped CeO_2 layers during film deposition and

subsequent conductivity measurement was highly unlikely to be an issue in this work. A calculation of the diffusion length of Y-cations in doped CeO_2 at 650 °C showed why this was so. Cation diffusion in fluorite-structured oxide ceramics at 650 °C is extremely slow with diffusion coefficients on the order of 10^{-26} m^2/s [98]. The total time for all film deposition and conductivity measurements was less than 35 hours, and for only a portion of this time were the samples at the maximum 650 °C. Nevertheless, we overestimated the diffusion length of Y-cations after 35 hours at 650 °C to be about 0.7 Å. Diffusion of the Y dopants through the films, therefore, were not a concern over the experimental time scales of this work.

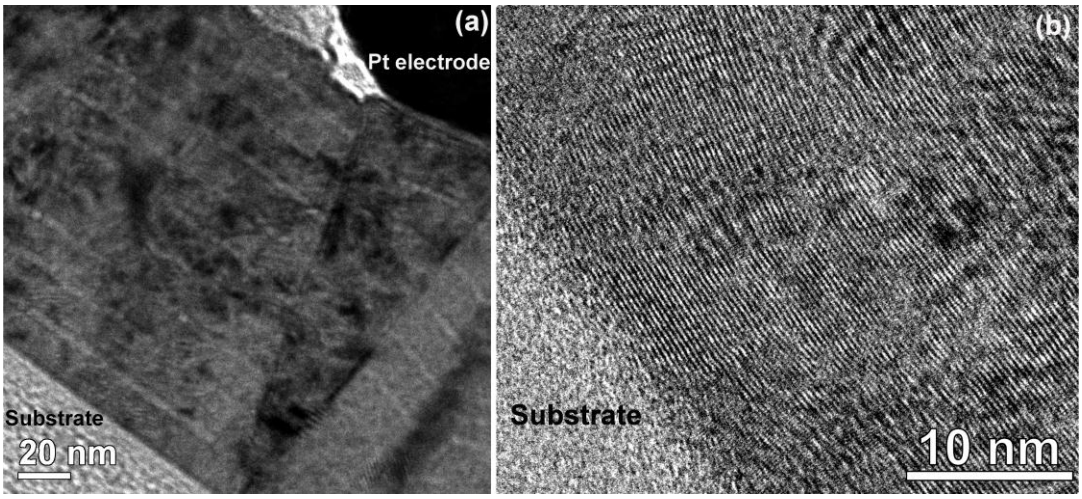

Figure 29 (a) Bright field TEM image of a cross section of sample D. In addition to the film, the substrate and platinum electrode are visible. (b) High resolution TEM of a near-substrate portion of the film cross section.

The impedance spectra of all the samples exhibited three main features, as shown in Figure 30. All the spectra consisted of a semicircle located at high frequency, a highly depressed semi-circular arc at intermediate frequency, and the first portion of

a semicircle at low frequency. Three R-CPE elements connected in series formed the equivalent circuit to fit the corresponding impedance spectrum. There was little overlap in frequency space between these features, and the equivalent capacitance values of the constant phase elements in the equivalent circuit differed by orders of magnitude. Thus, electrolytic resistance can be made from the high frequency as R1.

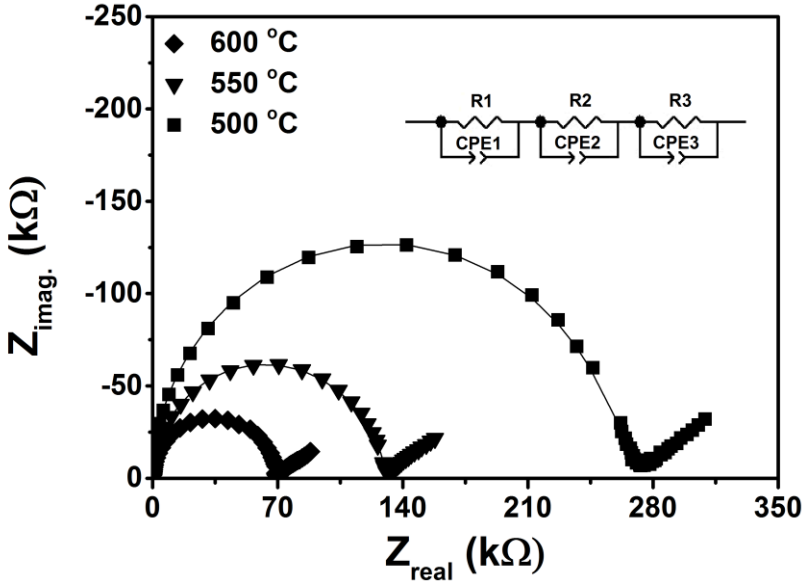

Figure 30 Impedance spectra of sample D at the temperatures indicated and the equivalent circuit used to fit the data

Figure 31(a) shows Arrhenius plots of the electrical conductivity measured for all samples in air. As can be seen from the figure, the conductivities of all four samples are relatively similar, especially at 650 °C. This result may be expected, since the total number of dopants was the same for every sample and only the distribution and mobility of the defects was changing. Below 650 °C, the samples with fully or

partially condensed dopant layers have conductivities lower than that of the homogeneously distributed sample.

Based on the dependence of *ln (σT)* on *1/T* shown in Equation (6), the corresponding activation energy for each sample was calculated. The activation energy for sample A was 0.76 eV, and the other three samples exhibit increased activation energy from 0.87 eV to 0.92 eV as the Y dopants were condensed into increasingly concentrated layers. A molecular dynamics study on YSZ showed a similar increased activation energy of oxygen ion diffusion from 0.68 eV to 0.90 eV when the randomly distributed Y-dopants condensed into a particular layer [94]. Figure 31(b) plots the activation energy as a function of the Y-dopant concentration in the Y-containing layer as well as similar data from conventionally fabricated YDC samples. The activation energies of samples A, B, and C compare well with measurements on conventionally prepared YDC when comparing against the dopant content of the doped layers in the multilayer samples [38]. This result indicates that most of the conduction in samples B and C was due to vacancies trapped in the doped ceria layers with little occurring in the pure ceria layers. This finding is quite similar when compared to multilayers composed of $Ce_{0.85}Sm_{0.15}O_{2-\delta}$ and CeO_2, in which the ionic defects in $Ce_{0.85}Sm_{0.15}O_{2-\delta}$ layers were also found to dominantly determine the overall electrical conductivity [99]. Sample D has much lower activation energy than pure Y_2O_3 (or highly doped CeO_2) and in fact has activation energy similar to nearly pure CeO_2. This result suggests that while conduction in samples A, B, and C occurred within predominantly the doped regions, most of the conduction in sample D occurred in the pure CeO_2 layers. The activation energy of sample D in Figure 31(b) was therefore plotted near pure CeO_2.

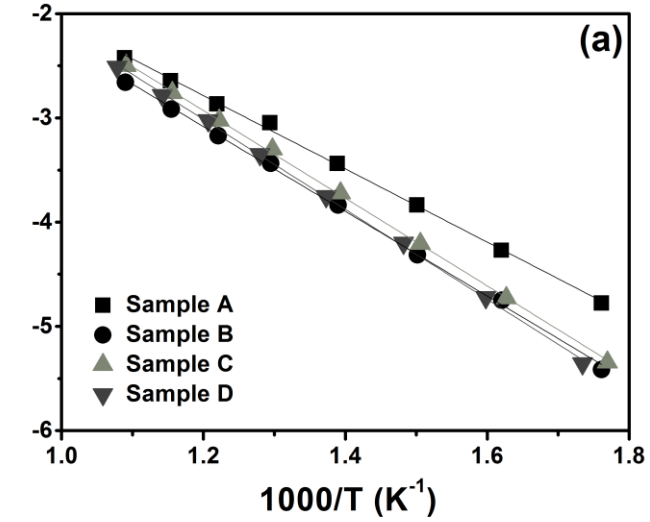
(a)
Sample A
Sample B
Sample C
Sample D
1000/T (K-1)

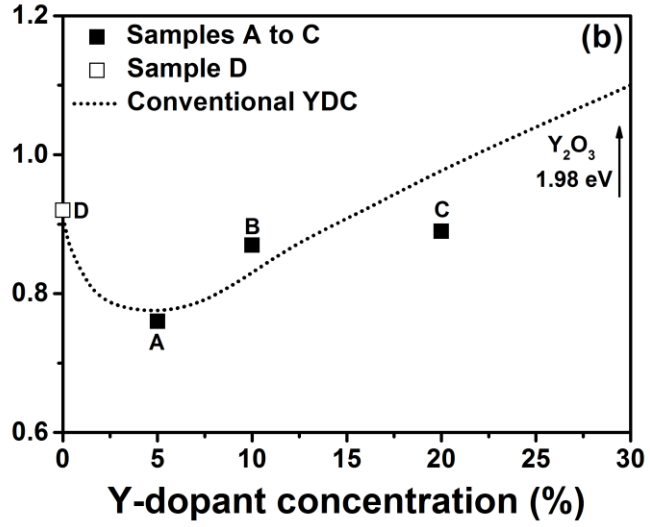
(b)
Samples A to C
Sample D
Conventional YDC
Y2O3
1.98 eV
D
B
C
A
Y-dopant concentration (%)

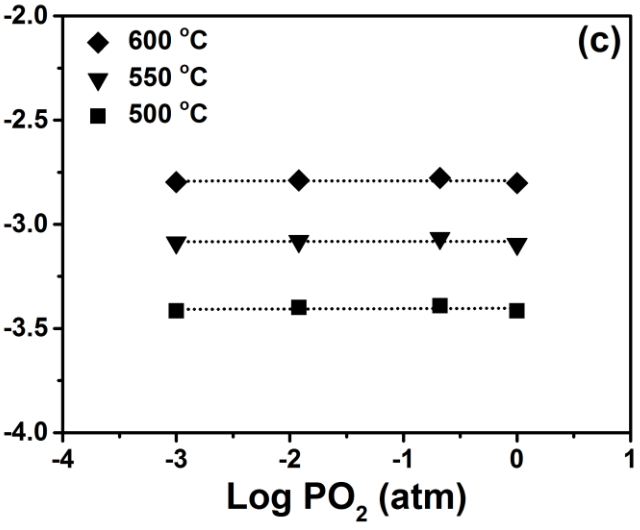
(c)
600 °C
550 °C
500 °C
Log PO2 (atm)

Figure 31 (a) Arrhenius plots of electrical conductivities measured for all samples, (b) the activation energy of the $\sigma \cdot T$ product of the samples as a function of the Y-dopant concentration in the Y-containing layer. Sample D is plotted at zero dopant concentration for reasons detailed in the following sections. Also shown for reference is the activation energy of conventionally fabricated YDC samples as reported in Ref. [38], and pure Y_2O_3, as calculated from oxygen diffusion measurements reported in Ref. [97]. (c) Electrical conductivity of sample D as a function of oxygen partial pressures at temperatures of 500 °C, 550 °C, and 600°C.

The electrical conductivity of sample D was also measured in 100 % O_2, 1.2 % O_2, and 0.1 % O_2, as shown in Figure 31(d). The conductivities at different oxygen partial pressures including air remained essentially constant, indicating that conduction was predominantly by ion vacancies in sample D. Electron conduction caused due to Ce^{4+}/Ce^{3+} polaron hopping was insignificant.

3.5 Beneficial Lattice Strain in Heterogeneously Doped CeO_2 Thin Films

The theory of heterogeneously doped electrolyte films was further developed by adjusting the net dopant content and the dopant identity. In RE_2O_3/CeO_2 films, increased dopant content was accomplished by varying the thickness of the pure CeO_2 layers from ≈ 19 nm to ≈ 4 nm. Since the total film thickness stayed ≈ 200 nm, the decreased CeO_2 layer thickness yielded an increased amount of dopant from 5% to 20% and the number of space charge regions. Dopant oxides examined here included Y_2O_3, Gd_2O_3, and La_2O_3. These three rare earth metal oxides adopt the same bixbyite crystal structure but with lattice parameters of 10.604 Å, 10.813 Å, and 11.327 Å, respectively [97, 100]. The fluorite-equivalent lattice parameters for Y_2O_3, Gd_2O_3, and La_2O_3 were estimated as 5.30 Å, 5.41 Å, and 5.66 Å, respectively. Compared with the lattice parameter of bulk CeO_2 (≈ 5.41 Å), these dopant oxides provided different

lattice mismatch at the interfaces. The lattice mismatch between Gd_2O_3 and CeO_2 can likely be neglected, but for films composed of CeO_2 with Y_2O_3 or La_2O_3, a biaxial compressive or tensile strain, respectively, was expected in the CeO_2 layers near the interfaces.

Three different sets of samples composed of alternating layers of CeO_2 with Y_2O_3, with Gd_2O_3, or with La_2O_3 were prepared, as summarized in Table 5. The total thickness of these samples was kept constant at ≈ 200 nm. Within each sample set, the individual layer thickness of RE_2O_3 was maintained at ≈ 1 nm, while the layer thickness of CeO_2 decreased from ≈ 19 nm to ≈ 4 nm to increase the number of heterogeneous dopant interfaces.

Table 5 Configuration of three different sets of heterogeneously doped CeO_2 films composed of alternating layers of RE_2O_3 and CeO_2. The total film thickness was maintained at ≈ 200 nm.

Samples	RE_2O_3 layer thickness (nm)	CeO_2 layer thickness (nm)	Number of bilayers
A	1	19	10
B	1	9	20
C	1	4	40

Similarly, a serious concern here could be the cation diffusion, with the dopants mixing with the neighboring undoped CeO_2 layers during film deposition and subsequent conductivity measurements. This concern, however, has been discussed in Y_2O_3/CeO_2 film and would be highly unlikely to become an issue due to the extremely low diffusion coefficients of cations in CeO_2 at temperatures below 650 °C. For films composed of CeO_2 with Gd_2O_3 and or with La_2O_3, compositional modulation through

the thickness at single nanometer resolution, however, was still not a problem. Rochenhäuser et al. investigated the cation interdiffusion between thin Gd_2O_3 films on CeO_2 substrates [101]. Based on that work, the Gd cation diffusion coefficient in CeO_2 could be estimated at about 2.8×10^{-27} m^2/s at 650 °C. A similar value between 10^{-26} $m^2/s \sim 10^{-27}$ m^2/s for the cation diffusion coefficient for La in CeO_2 at 650 °C could also be estimated from Ref. [102]. As mentioned before, the total time for sample preparation and conductivity measurement was less than 35 hours, of which only a small portion of the time were samples heated to the maximum of 650 °C. Ignoring that the diffusivity is greatly (exponentially) reduced at lower temperatures, the diffusion length for the dopants at 650 °C was calculated still to be less than 0.7 Å even after 35 hours.

Figure 32(a) shows the θ-2θ XRD patterns of the heterogeneously doped CeO_2 films with Y_2O_3. A single-layer, 105 nm thick CeO_2 film was also included for comparison. From the figure, we can see that the samples with 19 nm- and 9 nm-thick CeO_2 layers still exhibit orientations along both (111) and (100) directions. Although there is a difference in lattice parameters between CeO_2 and Y_2O_3, the CeO_2 (111) and (100) peaks are dominant in these two samples without any visible peaks corresponding to the Y_2O_3. This was similar compared to that of Figure 27. This finding can be attributed to the small amount of Y_2O_3 within the samples. For the sample with CeO_2 layer thickness of 4 nm, the CeO_2 (111) and (100) peaks are still dominant, but a small additional peak at $2\theta \approx 26.73°$ appears. This may be a satellite peak for the asymmetric superlattice formed in this film.

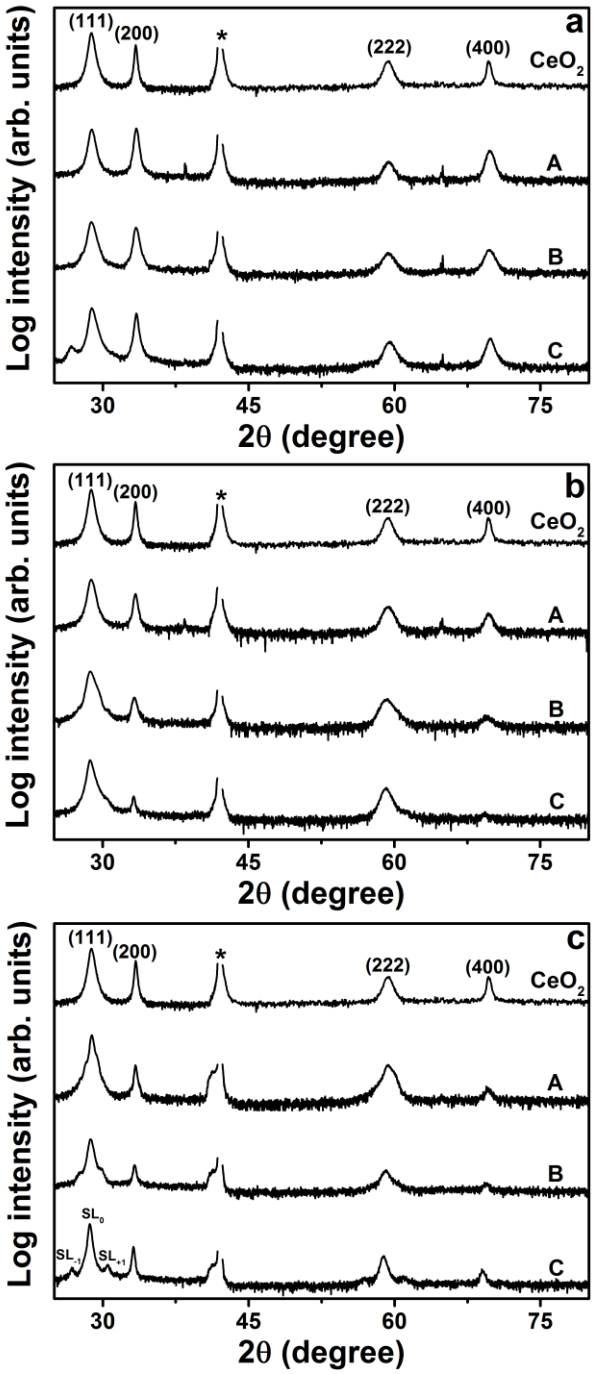

Figure 32 Typical θ-2θ XRD patterns of heterogeneously doped CeO_2 films composed of alternating layers of CeO_2 with (a) Y_2O_3, or with (b) Gd_2O_3, or with (c) La_2O_3 on Al_2O_3 (0001) substrates. A single layer CeO_2 film with thickness of ≈ 105 nm was also included for comparison.

Figure 32(b) shows the XRD patterns of the films composed of alternating layers of Gd_2O_3 and CeO_2. As with the Y_2O_3 samples, the films are all predominantly oriented along the CeO_2 (111) and (100) directions. As the layer thickness of CeO_2 decreased, an additional small peak begins to emerge on the right shoulder of the CeO_2 (111) peak. This small peak may also be a satellite superlattice peak, but since the fluorite-equivalent lattice parameter of Gd_2O_3 is very close to that of CeO_2, it was very difficult to distinguish. The XRD patterns of the films composed of alternating layers of La_2O_3 and CeO_2 are shown in Figure 32(c). Similar to the previous samples, no separate peaks corresponding to the diffraction planes of La_2O_3 were identified in the films with 19 nm- and 9 nm-thick CeO_2. As the layer thickness of CeO_2 decreased to 4 nm, a typical superlattice XRD pattern with an average structure peak SL_0 surrounded by two first-order satellite peaks, SL_{+1} and SL_{-1}, was observed for the (111) and (222) diffraction peaks. Similarly, the appearance of sharp, well-defined satellite peaks indicated the formation of high-quality interfaces between the adjacent layers [55].

Figure 33(a) shows typical impedance spectra from a film composed of 1 nm-thick Gd_2O_3 and 4-nm thick CeO_2. The spectra are almost the same compared to that of the Y_2O_3/CeO_2 film discussed in Figure 30(a). The resistance R1 was determined to be due to the ionic conduction through the electrolyte, while R2 and R3 were due to the electrode effects. Oxygen ion conductivity in the RE_2O_3 layers is expected to be exceedingly small. Ando et al. measured the oxygen self-diffusion coefficient in single crystal Y_2O_3 and found that the value was at least five orders of magnitude less than that of $Zr_{0.85}Ca_{0.15}O_{2-\delta}$ at 1100 °C [97]. Wirkus et al. observed that the electrical conductivity of Gd_2O_3 was on the order of 10^{-6} S/cm at 727 °C [103]. On the other hand, the electrical conductivity of pure CeO_2 at 650 °C is normally of order 10^{-3} S/cm

[91]. The contribution from the parallel RE_2O_3 layers to the total electrical conductivity of the heterogeneously doped CeO_2 films can thus likely be neglected. The electrical conductivity, therefore, was calculated based on the fitted resistance R1, the electrode geometry, and the total thickness of CeO_2 layers in each sample.

Figure 33(b) shows the Arrhenius plots of the electrical conductivity of the Y2O3/CeO_2 films in air. The conductivity of the sample with 9 nm-thick CeO_2 (20 bilayers) is somewhat increased compared to the sample with 19 nm-thick CeO_2 (10 bilayers). Further decreasing the layer thickness of CeO_2 to 4 nm (40 bilayers), however, yielded similar conductivity to the 20 bilayer sample. The homogeneously doped $Ce_{0.90}Y_{0.10}O_{2-\delta}$ single-layer film, however, exhibited larger conductivity by almost one order of magnitude compared to that of the heterodoped Y_2O_3/CeO_2 samples. Figure 33(c) and (d) show the conductivity of the Gd_2O_3/CeO_2 and La_2O_3/CeO_2 films. The conductivities of the single-layer homogenously doped $Ce_{0.80}Gd_{0.20}O_{2-\delta}$ (GDC), and $Ce_{0.85}La_{0.15}O_{2-\delta}$ (LDC) films are also included for comparison. At all temperatures, the conductivities of the Gd_2O_3/CeO_2 and La_2O_3/CeO_2 films monotonically increased as the layer thickness of CeO_2 decreased and the number of interfaces between RE_2O_3 and CeO_2 correspondingly increased. At the same time, the activation energy remained nearly constant. The conductivity of the heterodoped sample composed of 1 nm-thick La_2O_3 and 4 nm-thick CeO_2 approached that of the homogeneously doped LDC single-layer film with optimal 15% dopant concentration. The conductivities increase in order $La_2O_3>Gd_2O_3>Y_2O3$, which is notably not the behavior for these as homogeneously distributed dopants in ceria [104-106].

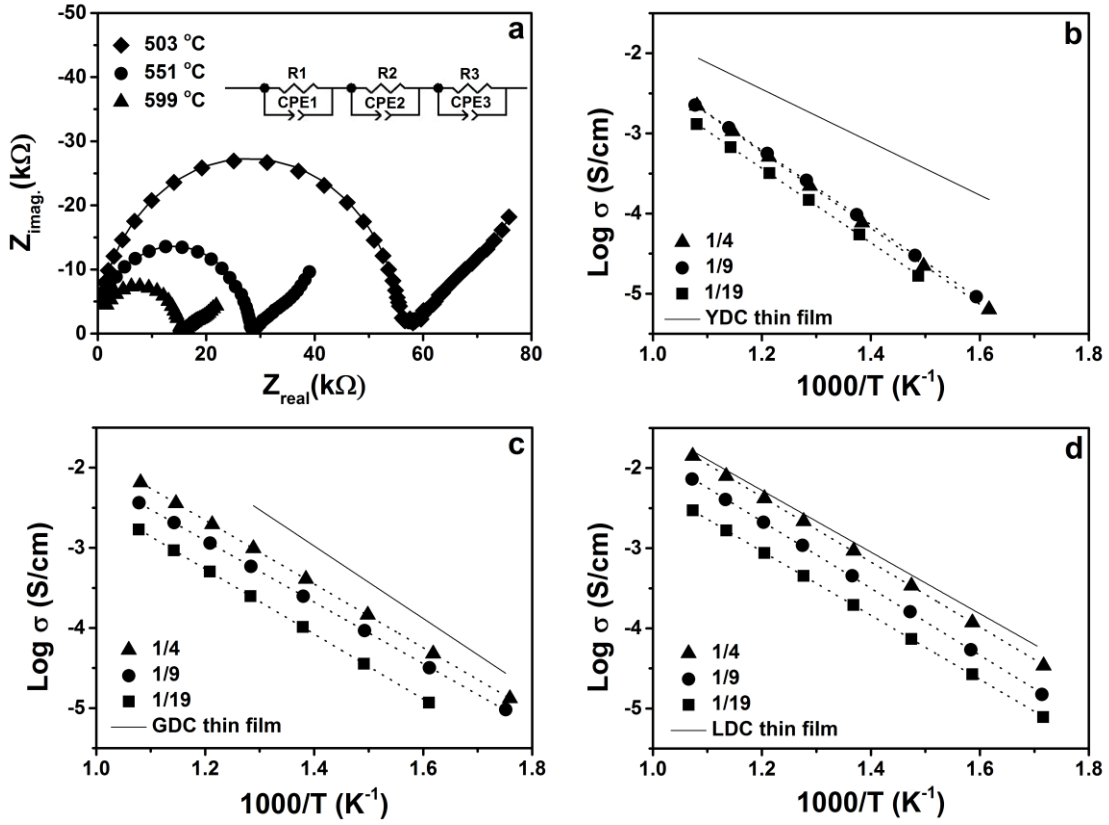

Figure 33 (a) Impedance spectra of a heterogeneously doped film composed of bilayers of 1 nm-thick Gd_2O_3 and 4-nm thick CeO_2 at the temperatures indicated. The equivalent circuit used to fit the data is inset. (b, c, d) Arrhenius plots of the electrical conductivity of heterogeneously doped films composed of CeO_2 with (b) Y_2O_3, (c) Gd_2O_3, or (d) La_2O_3. The symbols indicate whether the films consist of (*squares*) 10 bilayers of 1 nm RE_2O_3/19 nm CeO_2, (*circles*) 20 bilayers of 1 nm RE_2O_3/9 nm CeO_2, or (*triangles*) 40 bilayers of 1 nm RE_2O_3/4 nm CeO_2. The conductivities of single-layer $Ce_{0.90}Y_{0.10}O_{2-\delta}$ (YDC), $Ce_{0.80}Gd_{0.20}O_{2-\delta}$ (GDC), and $Ce_{0.85}La_{0.15}O_{2-\delta}$ (LDC) thin films with thicknesses of 192 nm, 173 nm, and 256 nm, respectively, were also included for comparison.

For the Gd_2O_3/CeO_2 and La_2O_3/CeO_2 samples, the conductivity scaled roughly linearly with the number of heterogeneous dopant interfaces. Figure 34 shows the

isothermal electrical conductivity of Y_2O_3/CeO_2, Gd_2O_3/CeO_2 and La_2O_3/CeO_2 films as a function of the number of the interfaces. For the films composed of Y_2O_3 and CeO_2, the conductivity has low dependence on the number of interfaces, but for the Gd_2O_3/CeO_2 and La_2O_3/CeO_2 samples, conductivity was roughly linearly dependent on the number of interfaces between RE_2O_3 and CeO_2.

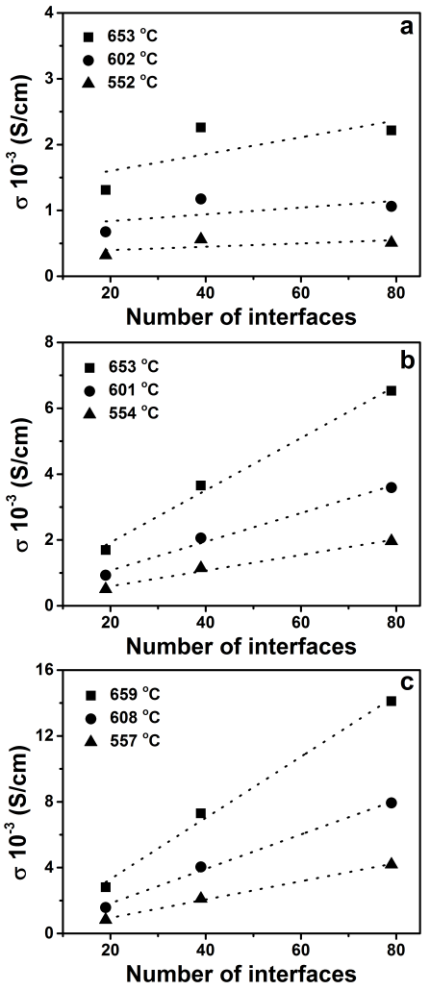

Figure 34 The isothermal electrical conductivity of the heterogeneously doped films composed of CeO_2 with (a) Y_2O_3, (b) Gd_2O_3, and (c) La_2O_3 as a function of the number of interfaces at three different temperatures, respectively. Note that average measurement temperatures for the three samples are given.

Chapter 4

DISCUSSION

4.1 Strain Effects on Oxygen Ion Conduction in Fluorite Materials

Multilayers composed of CZO with YDC or with YSZ have been fabricated in this work to symmetrically study the effects of compressive or tensile strain on oxygen ion conduction behavior in fluorite materials. We found that the compressive strain can significantly decrease the oxygen ion conductivity by at least one order of magnitude in YDC/CZO45 multilayers with lattice mismatch of -2.2%. Reduced lattice mismatch from -1.5% to near-zero for YDC/CZO30 to YDC/CeO_2 multilayers yielded conductivity near to the bulk YDC value, giving further confidence in the experimental results. One the other hand, very little conductivity change was found in the YSZ/CZO multilayers across the range of lattice mismatch between +2.9% and +5.2% and layer thickness between 5 nm and 35 nm, with values near to that of the bulk YSZ.

In order to better understand the conduction behavior of these multilayers with different lattice mismatches, the conduction paths through the YDC or YSZ layers were deconvoluted into two independent, parallel parts [70], as shown in Figure 35. The first part is conduction through the YDC or YSZ volume or bulk regions in which the oxygen ion conduction was assumed to be unaffected by the interfacial lattice strain. The second part is the conduction through the interfacial YDC or YSZ regions near the CZO. The relationship between the volume and interfacial conductivities has been discussed and derived in Ref. [70] as

$$\sigma_{tot} = \sigma_{vol} + 2\delta(\sigma_{\text{int}} - \sigma_{vol})\frac{1}{d} \tag{14}$$

in which σ_{tot} represents the total conductivity of the multilayers, σ_{int} and σ_{vol} denote the interfacial and volume (bulk) conductivity of YDC layers, respectively, δ is the thickness of the interfacial region, and d is the individual layer thickness of YDC or YSZ. Based on this equation, when $d \geq 2\delta$, the total conductivity σ_{tot} is linearly dependent on the reciprocal thickness of the YDC or YSZ layers with slope of 2δ (σ_{int} -σ_{vol}) and intercept of σ_{vol}, but for $d < 2\delta$, the total conductivity is only determined by the oxygen ion conduction through the interfacial regions. We used this model to further analyze the conduction behavior in YDC/CZO and YSZ/CZO multilayers in the following sections.

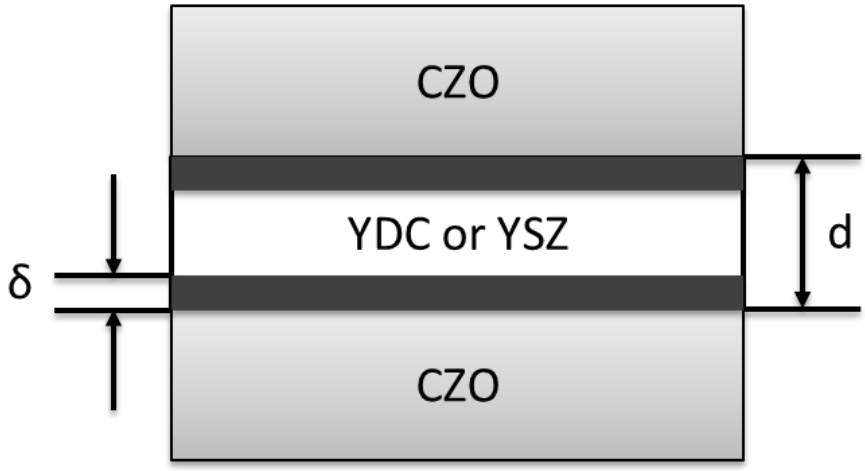

Figure 35 The two different conduction paths through the YDC or YSZ layers in YDC/CZO and YSZ/CZO multilayers. The black rectangular region represents the interfacial conduction path and the white region denotes the bulk conduction path.

Based on the Equation (14), a linear fit of the total conductivity as a function of $1/d$ allows us to calculate the volume and interfacial conductivities of the YDC or YSZ layers. The latter of these, σ_{int}, can be estimated from the slope if the thickness of the strained interfacial regions can be estimated. Figure 36 and Figure 37 show the total conductivities at 650 °C of the YDC/CZO and YSZ/CZO multilayered samples as a function of the reciprocal thickness of the layers, respectively. From the figure, we can clearly see that as the layer thickness decreased, the change of the total conductivity of the YDC/CZO multilayers was quite significant relative to that of the YSZ/CZO multilayers. The slope of the linear fit for YSZ/CZO multilayers almost approached zero, indicating little interfacial impacts on the overall oxygen ion conductivity in YSZ. Moreover, the conductivity of the three different types of YSZ/CZO multilayers exhibited very similar values, though the interfacial lattice mismatch was ranged between 2.9% and 5.2%.

As shown in Figure 36 and Figure 37, the intercept of the y-axis in the linear fit represents the volume conductivity of each multilayer. The thickness of the strained interfacial region in the multilayer is needed to be estimated, if we want to calculate the interfacial conductivity. Since the conductivity of each type of YDC/CZO multilayer continued to decrease even as the individual layer thickness became 5 nm, the thickness of the strained interfacial regions was believed to be ≤ 2.5 nm. We assumed here that the thickness of the strained interfacial regions was 2.5 nm for both YDC/CZO and YSZ/CZO multilayers, but it may be slightly smaller.

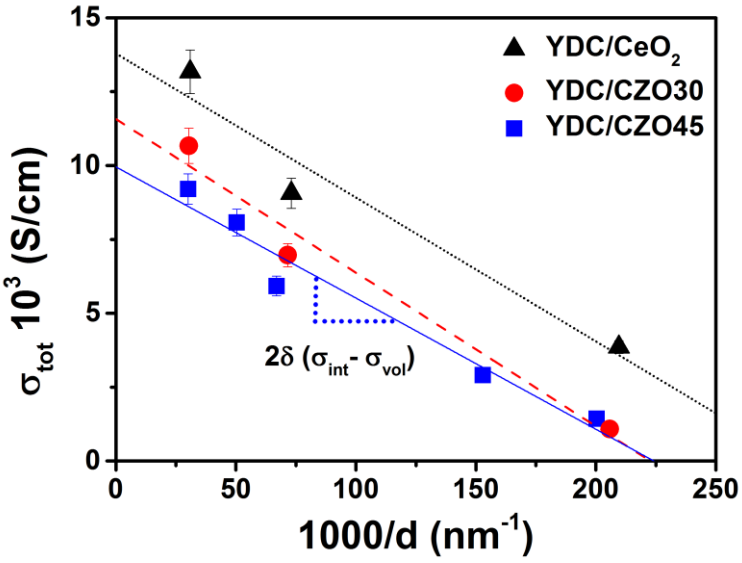

Figure 36 Conductivity isotherms at 650 °C of the three different types of multilayers as a function of the reciprocal thickness of the YDC layers, 1/*d*. The error bars represents estimated measurement uncertainty of a single sample.

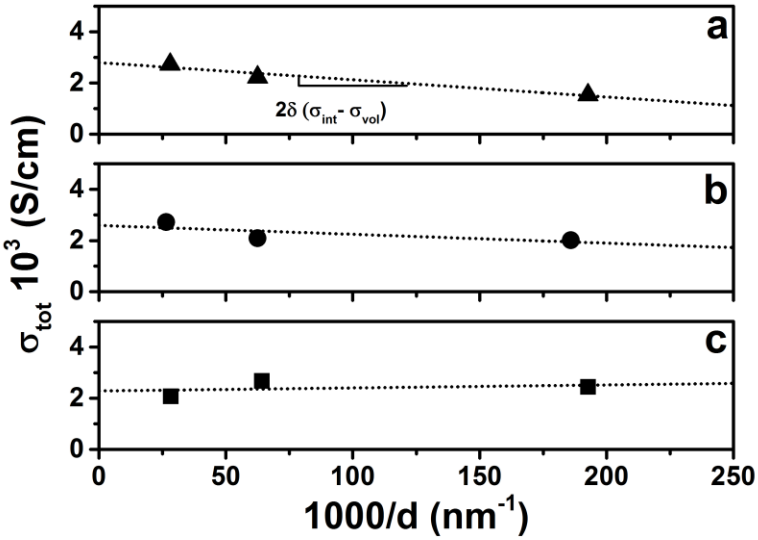

Figure 37 Conductivity isotherms at 650 °C of (a) YSZ/CeO_2, (b) YSZ/CZO30, and (c) YSZ/CZO45 multilayers as a function of the reciprocal thickness of the YSZ layers, 1/*d*.

Figure 38 and Figure 39 give the Arrhenius plots of the calculated volume (bulk) and interfacial conductivities of the three different types of YDC/CZO and YSZ/CZO multilayers, respectively, by assuming the thickness of the strained interfacial region δ = 2.5 nm. The volume conductivities in these two types of multilayers are all very similar to that of the YDC or YSZ single-layer films. This is expected, since the volume regions of the YDC or YSZ layers were assumed not to be affected by the interfacial strain.

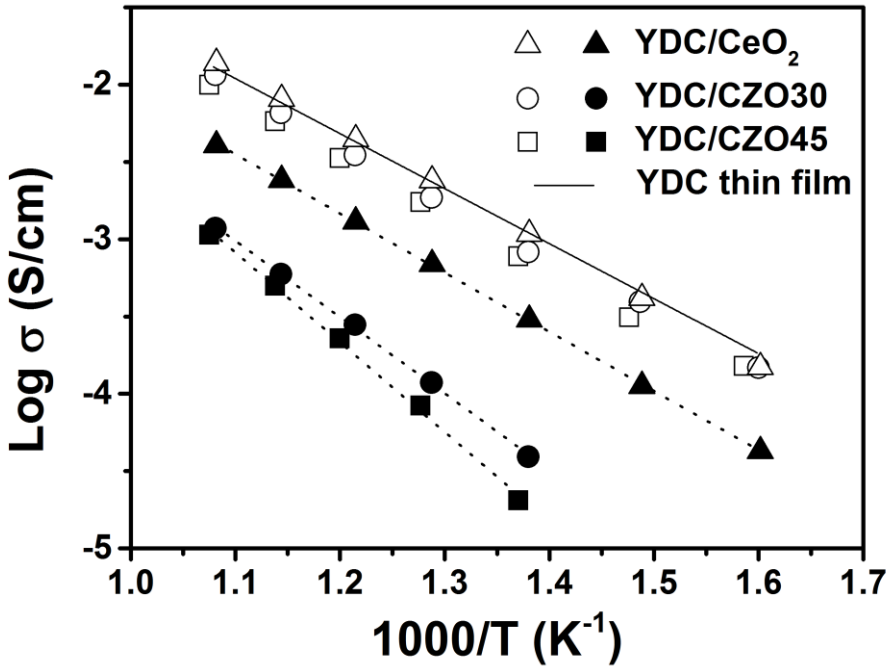

Figure 38 The calculated volume and interfacial conductivities for three different multilayers as a function of temperature. The YDC thin film data comes from measurements of a single layer film with thickness ≈ 195 nm. Note that the open symbols represent the volume conductivity and the solid symbols denote the interfacial conductivity.

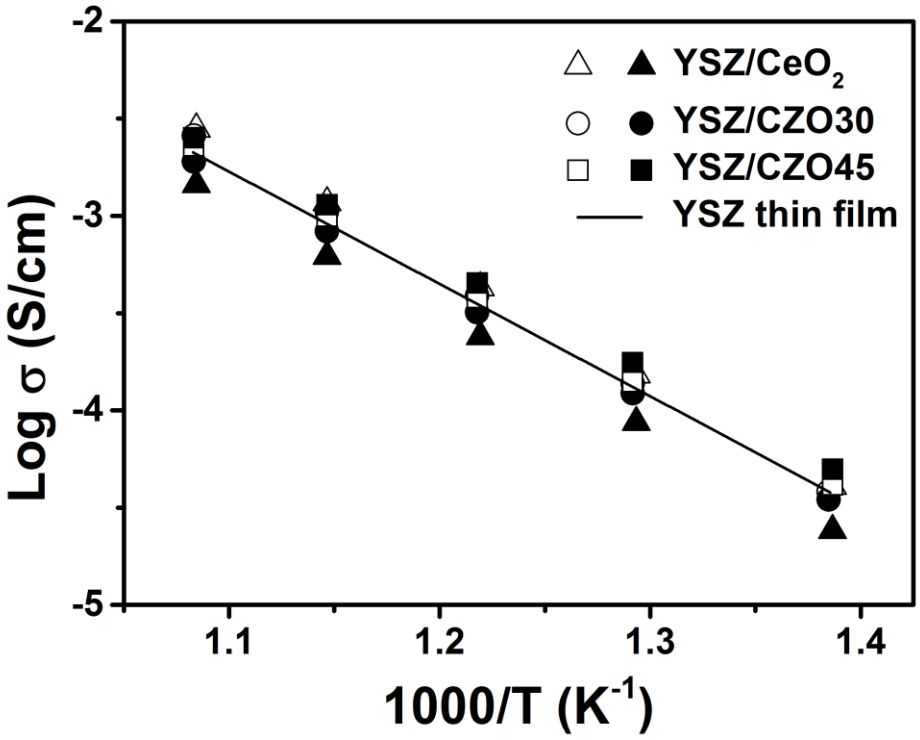

Figure 39 The calculated volume (bulk) and interfacial conductivities for three different types of multilayers of YSZ/CeO_2, YSZ/CZO30, and YSZ/CZO45 as a function of temperature. The YSZ thin film data comes from measurements of a single layer film with thickness of ≈ 105 nm. Note that the open symbols represent the volume conductivity and the solid symbols denote the interfacial conductivity.

From Figure 38, we can see that the interfacial conductivity for the YDC/CeO_2 multilayers is about half an order of magnitude less than that of the volume conductivity, though the interfacial lattice mismatch approached near-zero. This decreased conductivity may be due to the interfacial roughness or substrate-related effects. The conductivities of the YDC/CZO30 and YDC/CZO45 multilayers, however, are much smaller. The interfacial conductivity of the YDC/CZO30 multilayers is

slightly larger than that of the YDC/CZO45 multilayers due to the smaller interfacial lattice mismatch, but both of them are still much smaller than the volume conductivity by one order of magnitude at 650 °C and 1.5 orders of magnitude at 450 °C. Thus, the presence of compressive strain seems to significantly decrease the electrical conductivity of oxygen ion conductors.

Figure 39 compares the volume and interfacial conductivities in the YSZ/CZO multilayers. The interfacial conductivity of YSZ/CeO_2 multilayers was smaller by about a factor of ≈ 2 than that of the volume regions. This decreased conductivity may be due to interfacial roughness related to the very large lattice mismatch. The volume and interfacial conductivities of the YSZ/CZO30 and YSZ/CZO45 multilayers, however, were all nearly the same as the conductivity of a YSZ single-layer film. There is a correlation of increased interfacial conductivity as the zirconia content of the CZO layer is reduced (i.e., as the lattice mismatch with YSZ is reduced), though the changes are sufficiently small that this may be due to chance. The existence of tensile strain in YSZ seems to exhibit very little impacts on the overall oxygen ion transport properties.

Schichtel et al. reported on the effect of compressive strain on oxygen ion conductivity in YSZ/Sc_2O_3 multilayers with lattice mismatch of -4.28% [58]. The total conductivity was only decreased by a factor of ≈ 2 when the individual layer thickness decreased to 15 nm. This finding is similar to what is reported here for YDC/CZO45 multilayer with $N = 3$ (where the individual layer thickness was 15 nm), though the lattice mismatch at YSZ/Sc_2O_3 interface was nearly twice as large compared to that at the YDC/CZO45 interface. A large amount of interfacial strain seems to be released in YSZ/Sc_2O_3 multilayers since misfit dislocations were identified both at interfaces and

in the volume regions [58]. The reduction of the interfacial conductivity relative the volume region, however, was not discussed in YSZ/Sc_2O_3 multilayers due to the difficulty of estimation of δ. In order to better quantify the effect of compressive strain on conductivity in this work, Figure 40 shows the interfacial conductivity normalized to the volume conductivity as a function of the lattice mismatch in YDC/CZO multilayers. Data from a few different temperatures are shown. For near-zero lattice mismatch, the interfacial conductivity was reduced to about 30% of the volume conductivity. As mentioned before, the mechanism of this effect is either interfacial roughness or substrate-related effects. As the lattice mismatch compressive strain in YDC layers increased, the normalized conductivities decreased in a roughly log-linearly fashion. At 650 °C and 550 °C, the normalized conductivities at lattice mismatch of -1.5% and -2.2% were found to be relatively similar. This finding seems to indicate that at higher temperatures, the temperature plays a more important role on the oxygen vacancy mobility compared to that of lattice mismatch. The effect of compressive strain increased at lower temperatures, in accordance with prediction. From the linearized slops in Figure 40, each 1% increase in compressive strain in the YDC yielded a 1.6-fold reduction in interfacial conductivity at 650 °C and 3-fold reduction at 450 °C.

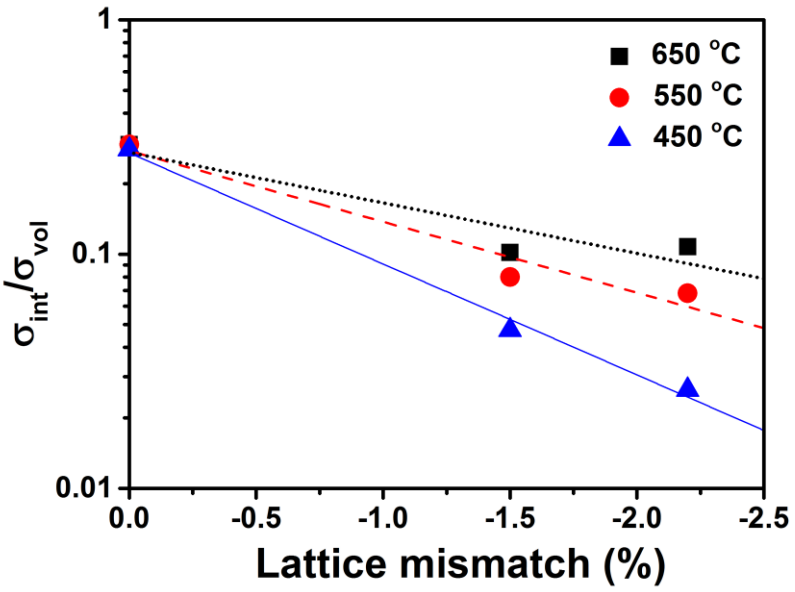

Figure 40 Normalized conductivity of the multilayers as a function of the lattice mismatch. Note that the y-axis scale is logarithmic.

The effects of tensile strain on oxygen ion conductivity have been extensively studied in literature. In Korte et al.'s investigation of multilayers composed of YSZ and Y_2O_3, interfacial lattice mismatch of ≈ +3% correlated to significant increases in conductivity [57]. The total conductivity gradually increased by a factor of ≈ 2 as the YSZ layer thickness decreased from 526 nm to 24 nm. At the same time, the activation energy decreased from 1.13 eV to 0.99 eV, suggesting that the strain was effectively increasing vacancy mobility. Li et al. studied multilayers composed of YSZ and $Gd_2Zr_2O_7$, which has a similar lattice mismatch of +3% compared to the YSZ/Y_2O_3 multilayers [56]. A key difference with this type of multilayers is that, unlike Y_2O_3, $Gd_2Zr_2O_7$ is an oxygen ion conductor. There is thus the risk of a convolution of lattice mismatch strain-based effects, with the conducting phase on one side of the interface

being compressed simultaneously with the conducting phase on the other side of the interface being expanded. Nevertheless, Li et al. reported that the +3% lattice mismatch caused the oxygen ion conductivity to increase by about 2 orders of magnitude relative to bulk YSZ when the layer thickness decreased to 5 nm. The increased conductivity was attributed to the coherent, dislocation-free interfaces between YSZ and $Gd_2Zr_2O_7$, imposing large tensile strain on YSZ layers.

The three different types of YSZ/CZO multilayers studied here indicate that tensile lattice mismatch caused very little effect on the oxygen ion transport properties. The XRD patterns shown in Figure 22 indicate that the out-of-plane lattice parameters for YSZ were essentially unaffected across the range of lattice mismatch magnitudes and layer thicknesses employed in this study. The > +5 % lattice mismatch between YSZ and pure CeO_2 makes it likely that the strain was released by the creation of non-coherent interfaces in these multilayers. It is not surprising then that, as in reference [69], no change in conductivity was measured.

The YSZ/CZO45 multilayers possess similar lattice mismatch as the YSZ/Y_2O_3 [57] and YSZ/$Gd_2Zr_2O_7$ [56] multilayers. It is more surprising that no change in conductivity was measured in the YSZ/CZO45 multilayers, since the references [56, 57] suggest that YSZ was capable of accommodating this magnitude of lattice mismatch strain. Thus, we conclude that lattice mismatch strains of ≈ +3 % are close to a maximum practically achievable limit for YSZ, with the creation of coherent interfaces dependent on processing details. Reports of significantly greater tensile strains being accommodated in YSZ, therefore, must be treated with caution. Results from multilayers composed of doped ZrO_2 and doped CeO_2 that have been reported in the literature [54, 55] (e.g., YSZ and $Ce_{0.8}Sm_2O_{2-\delta}$) suggested that significant increase

in conductivity can be derived due to > +5% lattice mismatch. It is difficult to believe that such large tensile strains could be accommodated in YSZ.

4.2 Space Charge Effects on Oxygen Ion Conduction in Fluorite Materials

Oxygen ion conduction in heterogeneously doped CeO_2 films composed of alternating layers of pure RE_2O_3 and pure CeO_2 has been investigated using different CeO_2 layer thickness and dopant identity. Figure 41 illustrates a schematic anion superlattice near the RE_2O_3/CeO_2 interface. The three RE_2O_3 including Y_2O_3, Gd_2O_3, and La_2O_3 all adopt the cubic bixbyite crystal structure, which can be described as a "pseudo-fluorite" structure with an ordered array of one of every four oxygen sites unfilled. Strictly speaking, the unfilled sites are interstitial locations, and the migration of an oxygen ion from the CeO_2 into one of these sites in the RE_2O_3 lattice can be described as

$$^{CeO_2}O_O + {}^{RE_2O_3}V_i \rightarrow {}^{CeO_2}V_O^{\bullet\bullet} + {}^{RE_2O_3}O_i'' \qquad (15)$$

where the text in superscript preceding each defect indicates the lattice in which the defect formally resides. This simple picture, though, is complicated by the fact that the interface has some chemical resemblance to a 50% doped ceria. Thus, this migration event may proceed to a greater extent than bulk measurements of defect formation energies in RE_2O_3 would suggest. The space charge regions created by the spatially dependent defect formation provide a counteracting Coulombic energy to limit the extent of the above reaction. Similar effects in La_2O_3/CeO_2 interfaces have been examined as a means to reduce oxygen vacancies in La_2O_3 gate dielectrics [107-110].

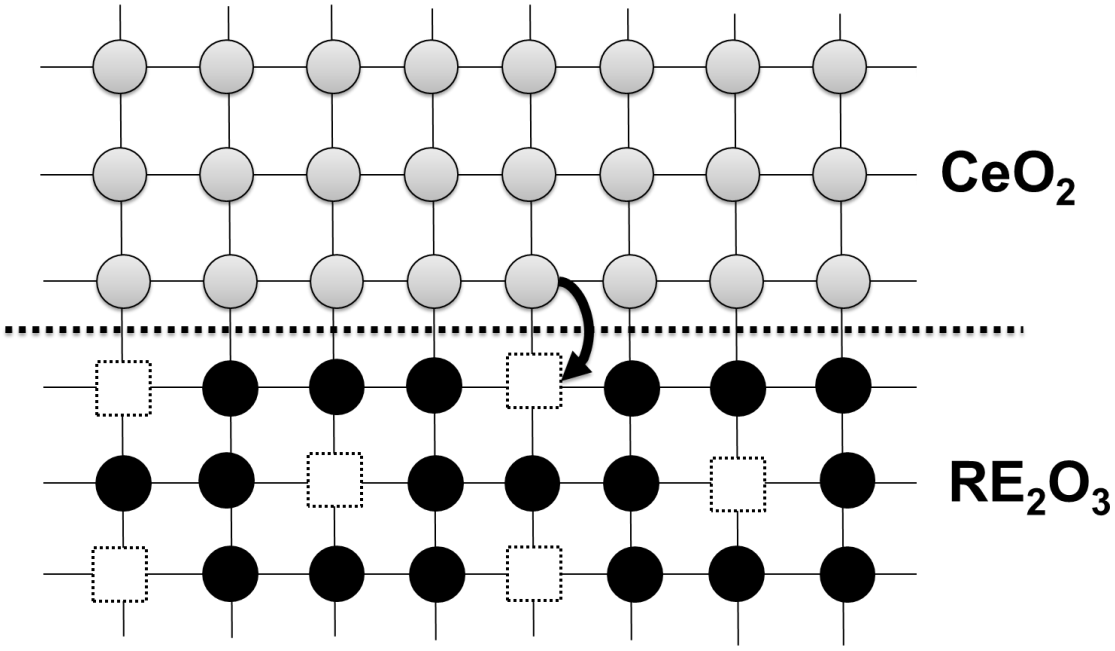

Figure 41 A schematic anion superlattice structure at RE_2O_3/CeO_2 interface. Grey circles represent oxygen in the CeO_2 lattice, while black circles represent oxygen in the RE_2O_3 lattice. The open squares represent unfilled sites in RE_2O_3. The arrow indicates the movement of an oxygen ion from CeO_2 into RE_2O_3, creating an oxygen ion interstitial at the previously unfilled site in RE_2O_3 and leaving behind an oxygen vacancy in CeO_2.

4.2.1 Gouy-Chapman Model for Space Charge Distribution

In order to better understand the conduction behavior of these heterogeneously doped CeO_2 films, the ionic conduction paths through the RE_2O_3 layers and the layers of CeO_2 were deconvoluted. As shown in Figure 41, some number of oxygen ions diffused from pure CeO_2 layers into the RE_2O_3 layer, creating a space charge region at the interface where oxygen vacancies were accumulated in CeO_2. Vacancies were correspondingly depleted in the RE_2O_3 layer.

The extension of the space charge region at the interface is on the order of Debye length λ, given by

$$\lambda = \sqrt{\frac{\varepsilon_r \varepsilon_o k_B T}{2 z_v^2 e^2 c_{v,\infty}}} \tag{16}$$

where ε_r is the relative dielectric constant ($\approx$ 23 for CeO_2 [111]) , ε_o is the permittivity of free space, k_B is the Boltzmann constant, T is the absolute temperature, z_v is the effective charge number of an oxygen vacancy, e is the elementary charge, and $c_{v,\infty}$ is the oxygen vacancy concentration in the bulk [53]. The bulk oxygen vacancy concentration in RE-doped CeO_2 is very large and determined by the amount of added dopants according to conventional defect chemical analysis. Bulk vacancy concentration of Y_2O_3 was calculated to be 1.34×10^{22} cm^{-3} (taking "pseudo fluorite" Y_2O_3 lattice parameter as 5.30 Å). In this calculation, we consider the Y_2O_3 lattice to be, essentially, fluorite with oxygen unfilled sites that are ordered yet able to diffuse into the neighboring CeO_2 lattice. Then, the Debye length in the Y_2O_3 was calculated to be less than 1 Å at our measurement temperatures. In such small space charge regions in RE_2O_3, the depletion of oxygen vacancies due to diffusion into a neighboring pure CeO_2 layer was thus not likely to affect the overall conductivity of a RE_2O_3 layer. For simplicity, the concentration of oxygen vacancies in each of the RE_2O_3 layers can be assumed constant through the layers at the values given above.

In the undoped, nominally pure CeO_2, the concentration of oxygen vacancies is low, introduced either by a background concentration of acceptor impurities or by an intrinsic reduction reaction. Kosacki et al. used Raman spectroscopy to study the oxygen vacancy concentration as a function of grain size in CeO_2 thin films [112]. The vacancy concentration at 27 °C for a sample with grain size of 30 nm was estimated to be 7×10^{17} cm^{-3} (rising from roughly 2×10^{17} cm^{-3} for samples with larger grains).

Göbel et al. and Hwang et al. utilized conductivity measurements to calculate the vacancy concentration in undoped CeO_2 [113, 114]. The values were reported to be 1×10^{18} cm^{-3} (700 °C, oxygen partial pressure = 0.987 atm) by Göbel et al. in an epitaxial CeO_2 film on Al_2O_3 and within the range 1.3×10^{18} cm^{-3} to 2.9×10^{18} cm^{-3} (551 °C, oxygen partial pressure = 0.0013 atm) by Hwang et al. in CeO_2 with a grain size of 15 nm. Increased oxygen vacancy concentration at higher temperature and lower oxygen partial pressure is expected, since more vacancies were generated in these conditions from the intrinsic reduction reaction. The vacancy concentration in the pure CeO_2 layers in this work was assumed to be at least 7×10^{17} cm^{-3} at 300 °C, resulting in a Debye length of at most 3 nm at our measurement temperatures.

The distribution of oxygen vacancies trapped in the CeO_2 space charge regions from the layers of RE_2O_3 can be characterized by a Gouy-Chapman model. At thermodynamic equilibrium, the concentration of oxygen vacancies needs to satisfy

$$\left(\frac{c_v(x)}{c_{v,\infty}}\right)^{\frac{1}{z_v}} = \exp\left(-\frac{e(\varphi(x)-\varphi_\infty)}{k_B T}\right) \tag{17}$$

where $c_v(x)$ represents the oxygen vacancy concentration at a distance x from the interface and $\phi(x)$ and $\phi(\infty)$ denote the electrical potential at x and in the bulk [53]. Based on the semi-infinite boundary conditions described in [115], Equation (17) can be solved as

$$\frac{c_v(x)}{c_{v,\infty}} = \left(\frac{1+\Theta\exp(-x/\lambda)}{1-\Theta\exp(-x/\lambda)}\right)^2 \tag{18}$$

with a parameter Θ defined as

$$\Theta = \frac{(\sqrt{c_v(0)/c_{v,\infty}}-1)}{(\sqrt{c_v(0)/c_{v,\infty}}+1)} \tag{19}$$

where c_v (0) represents the vacancy concentration at the interface of CeO_2 near RE_2O_3 ($x = 0$). Since the vacancy concentration in RE_2O_3 was assumed constant through the layers, the value of c_v (0) was set equal to the bulk vacancy concentration of the RE_2O_3 layer. Figure 42 shows the calculated distribution of oxygen vacancies in a bilayer composed of 19 nm-thick CeO_2 and 1 nm-thick Y_2O_3 at two different temperatures. For demonstration, the bulk vacancy concentration in the 19 nm-thick CeO_2 layer was assumed to be 7×10^{17} cm^{-3} at 27 °C (300 K) as in Ref. [112] and 2.9×10^{18} cm^{-3} at 551 °C (824 K) as in Ref.[114]. Based on these values, the Debye length in the pure CeO_2 layer was calculated to be 2.4 nm at 27 °C (300 K) and 2 nm at 551 °C (824 K).

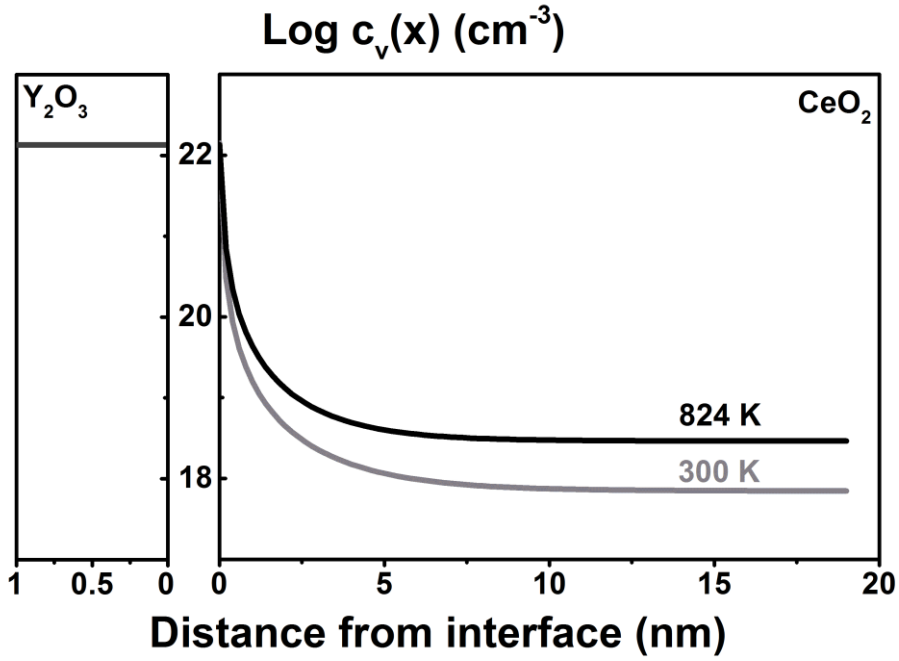

Figure 42 The distribution of oxygen vacancies in a bilayer composed of a 19 nm-thick CeO_2 layer in contact with a 1 nm-thick Y_2O_3 layer at the temperatures indicated.

The accumulation of oxygen vacancies in the space charge region leads to an increase of ionic conductivity in pure CeO_2 layer. Ionic conduction in the CeO_2 layer adjacent to the RE_2O_3 layer measured parallel to the interface arises from vacancies naturally present in the bulk and from those accumulated or trapped in the space charge region. The thickness-dependent parallel conductance was employed here to evaluate the contribution of space charge region to the overall ionic conduction of the multilayer. The total conductivity in the CeO_2 layer is calculated based on Equation (18) as

$$\sigma_{CeO_2} = \sigma_{v,\infty} + \frac{2\lambda}{L}\sigma_{v,\infty}\left(\frac{2\Theta}{1-\Theta}\right) \tag{20}$$

in which $\sigma_{v,\infty}$ represents the ionic conductivity of CeO_2 in the bulk [53], defined as

$$\sigma_{v,\infty} = z_v e \mu_v c_{v,\infty} \tag{21}$$

where μ_v denotes the vacancy mobility of CeO_2 in the bulk. By substituting the Debye length λ, Θ, and the bulk conductivity $\sigma_{v,\infty}$ from Equation (16), (19), and (21) into Equation (20), the total conductivity in CeO_2 layer can be further simplified to

$$\sigma_{CeO_2} = \sigma_{v,\infty} + \frac{1}{L}\mu_v\sqrt{2\varepsilon_0\varepsilon_r k_B T c_v(0)} \tag{22}$$

Then, the total parallel conductance of the CeO_2 layer can be derived from Equation (22) and the geometry of the electrodes that used in this work as

$$G_{CeO_2} = \sigma_{v,\infty} + \frac{1}{L}\mu_v\sqrt{2\varepsilon_0\varepsilon_r k_B T c_v(0)}\,\frac{t \times L}{w} \tag{23}$$

in which t and w represent the total perimeter length and separation distance, respectively, of the interdigitated Pt electrodes. The parallel conductance of bulk CeO_2 is

$$G_{CeO_2,\infty} = \sigma_{v,\infty} \frac{t \times L}{w} \tag{24}$$

and the difference between the total conductance of CeO_2 layer and the conductance of bulk CeO_2 is considered to be the conductance of space charge region:

$$G_{CeO_2,SC} = G_{CeO_2} - G_{CeO_2,\infty} = \mu_v \sqrt{2\varepsilon_0 \varepsilon_r k_B T c_v(0)} \frac{t}{w} \tag{25}$$

Interestingly, the excess or space charge conductance was not related to the Debye length or bulk vacancy concentration of pure CeO_2 and was only a function of vacancy mobility μ_v, temperature T, the vacancy concentration at the interface c_v (0), and the electrode geometry.

The mobility of oxygen vacancies in the space charge region was initially assumed to be equal to that in the bulk of CeO_2 layer, though this assumption may be invalid when significant lattice strain exists, as given in Ref. [116]:

$$\mu_v = 1.2 \exp\left(-\frac{0.87eV}{k_B T}\right) cm^2 V^{-1} s^{-1} \tag{26}$$

The total excess conductance of the space charge regions in a multilayer can be calculated by

$$G_{Total,SC} = (2n-1)\mu_v \sqrt{2\varepsilon_0 \varepsilon_r k_B T c_v(0)} \frac{t}{w} \tag{27}$$

in which n is the number of CeO_2 layers in the multilayer (= 10, 20 or 40 in this work). The factor ($2n$-1) is used, since each CeO_2 layer after the first one was in contact with RE_2O_3 layers on two sides, creating two space charge regions. The first layer has an interface with the substrate on one side.

The effect of the grain boundaries, as seen in Figure 29(a), on the total conductivity of these samples was not yet determined. Still, these films were prepared

to high purity using low temperature processing, and thus the segregation of dopants and impurities to the grain boundaries can likely be neglected. Further, the TEM shows that the layered dopant structure exists up to the grain boundaries as within the grains. For these reasons, the one-dimensional model of vacancy concentration distribution is still believed to remain valid. Our analysis did not discuss the origin of the mobility of vacancies or any deviations thereto, considering them to be the bulk value. If the mobility is reduced by the blocking effect of the grain boundaries [113], then the model requires only quantitative adjustment to this parameter.

Figure 43 compares the parallel conductances of the doped layer, the bulk of the pure CeO_2, and the space charge regions of the pure CeO_2 for sample composed of 1 nm-thick Y_2O_3 and 19 nm-thick CeO_2. Conductances, and not conductivities, were plotted since they can be directly compared and/or added for these samples, where these conduction paths exist in parallel through paths with differing thicknesses. In Y_2O_3/CeO_2 sample, the total thickness of all Y_2O_3 and CeO_2 layers are about 10 and 190 nm, respectively. The conductivity of bulk CeO_2 was obtained from Ref. [91] for a CeO_2 film with grain size of 30 nm deposited on Al_2O_3 substrate. The conductivity of Y_2O_3 was calculated based on Equation (21) in which the bulk vacancy concentration was assumed to be 1.34×10^{22} cm^{-3}, and the vacancy mobility in Y_2O_3 was calculated based on the reference data of oxygen self-diffusion coefficient through the Nernst-Einstein equation [97].

As shown in Figure 43, the parallel conductance of pure Y_2O_3 layers is extremely small, and can be neglected. The conductance of pure CeO_2 layers is still almost two orders of magnitude less than that of the whole sample. The oxygen ions, therefore, are not just individually migrating through the layers of Y_2O_3 and CeO_2. On

the other hand, the conductance of the space charge regions was found to be close to that of this Y_2O_3/CeO_2 sample and exceeds that of the CeO_2 bulk and the Y_2O_3, indicating that the vacancies that are accumulated or trapped in the space charge regions are dominant in ionic conduction. Still, the conductance of the sample exceeds expectations for conductance through the space charge regions. It is not yet clear why this is so, but suggests that more vacancies are being transferred from theY_2O_3 lattice to the CeO_2 than accounted for in the Gouy-Chapman model used above. Specifically, the assumption that the oxygen site occupancy in Y_2O_3 maintains bulk values through the thickness may be invalid, given that the vacant sites are uncharged. Reported vacancy mobility values in pure CeO_2 were also somewhat variable, so it may be that the vacancies in the space charge regions are more mobile than assumed.

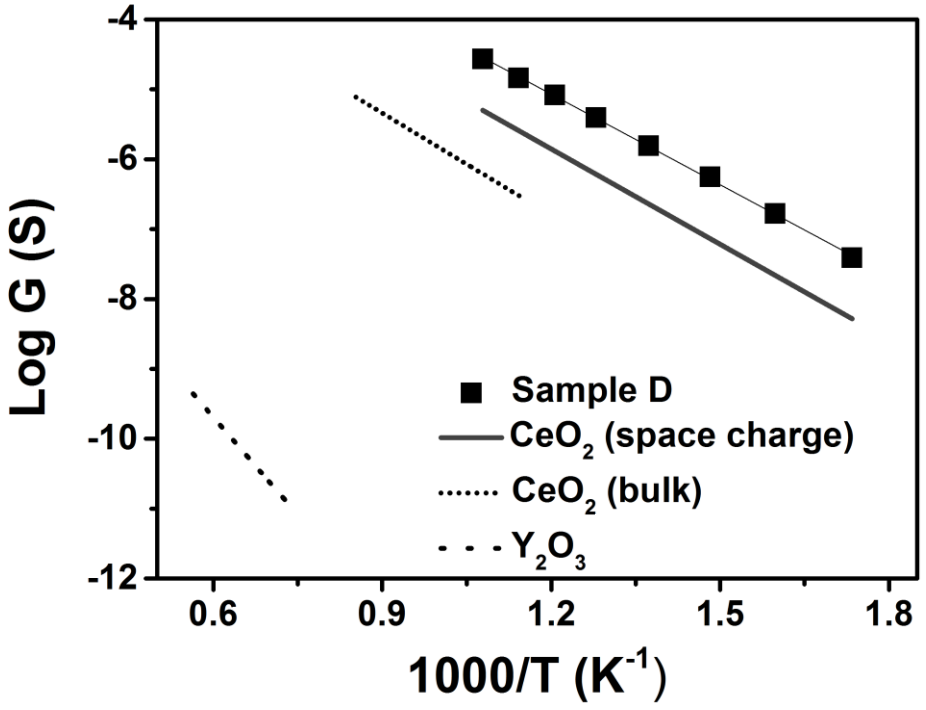

Figure 43 Comparison of parallel conductance of the sample composed of 1 nm-thick Y_2O_3 and 19 nm-thick CeO_2 to that of its doped layers of Y_2O, bulk of CeO_2, and space charge regions.

4.2.2 Effects of Lattice Strain on Space Charge Distribution

We used a Gouy-Chapman model to calculate the distribution of oxygen vacancies in the space charge regions of the CeO_2 layers and the excess conductance induced there by the accumulated or trapped vacancies. The value of excess conductance in space charge regions was found to be similar to that of the whole Y_2O_3/CeO_2 multilayer, indicating that the vacancies in the space charge regions of CeO_2 layers became dominant in the ionic conduction of the whole multilayer. The concept of heterogeneously doped electrolyte films was then expanded by using different net dopant content and the dopant identify (Y_2O_3, Gd_2O_3, and La_2O_3). For all

of the samples, the thickness of the entire structure and that of the individual dopant layers were kept constant. All of these three dopant oxides adopt the cubic bixbyite crystal structure with "pseudo-fluorite" lattice parameters that are, relative to CeO_2, smaller (Y_2O_3), larger (La_2O_3), and nearly equal (Gd_2O_3). The total conductivity of the films, as shown in Figure 34, was found to be increased with increasing lattice parameter of the dopant oxides.

Based on the Gouy-chapman model, as shown in Equation (27), the conductivity of heterogeneously doped films should be linearly dependent on the number of interfaces and the square root of interfacial vacancy concentration. The three different RE_2O_3 used in this work adopt the same cubic bixbyite crystal structure and, therefore, theoretically possessed the same concentration of vacant oxygen sites. Thus, a purely electrostatic model such as Gouy-Chapman cannot account for the finding here that heterogeneously doped films composed of CeO_2 with Y_2O_3, or with Gd_2O_3, or with La_2O_3 exhibited different conductivity values when they have the same number of interfaces. Moreover, the Gouy-Chapman model cannot explain why the films heterodoped with Y_2O_3 exhibited conductivity values that did not linearly scale as the number of interfaces increased.

The most obvious difference between these three dopant oxides examined here is their lattice parameter. The significant change in conductivity behavior across these three dopants suggested that lattice mismatch strain was influencing the oxygen ion conductivity in the space charge regions. The effect of lattice strain on oxygen ion conduction behavior has been extensively studied in nanometric multilayered systems using doped conductors [54-58, 69]. A number of studies—with notable exceptions—have found that biaxial tensile strain induced in zirconia or ceria based solid

electrolyte films increased the total oxygen ion conductivity, while compressive strain had the opposite effect. For systems involving highly doped conductors, the space charge regions are inconsequentially small and thus the concentration of oxygen vacancies was normally fixed by the dopant concentration. The increased conductivity was, therefore, attributed to increased vacancy mobility in tensile-strained regions due to the reduced migration energy.

A linear fit of $ln\ (\sigma \cdot T)$ as a function of $1/T$ allows the calculation of E_a. Figure 44 shows the activation energy of the $\sigma \cdot T$ product of each of the three different types of heterogeneously doped CeO_2 films. For each of the dopants, the activation energy is weakly and non-monotonically dependent on the concentration of dopants in the films (i.e., the number of heterodopant/CeO_2 interfaces). Specifically, the activation energy does *not* significantly increase as the net dopant concentration increases from 5 % to 25 %. This behavior is different from homogenously doped ceria [37]. For example, in homogeneously distributed YDC, the activation energy of a 5 % doped sample was 0.77 eV, whereas that of a 26 % doped sample was 1.1 eV[38]. The constancy of the activation energy over the large range of dopant content for the heterogeneously doped samples reported here indicates that increased dopant content does not lead to more deeply trapped vacancies. This result is as expected from the space charge model, where the mobile defects are in the pure ceria layers, many of them greater than one bond length's distance from the dopants. Any effects of dopant-vacancy association are thus reduced for these defects. A practical benefit of this effect may be that large total mobile defect concentration may be possible in solid electrolytes without coincident high activation energy using heterogeneous doping.

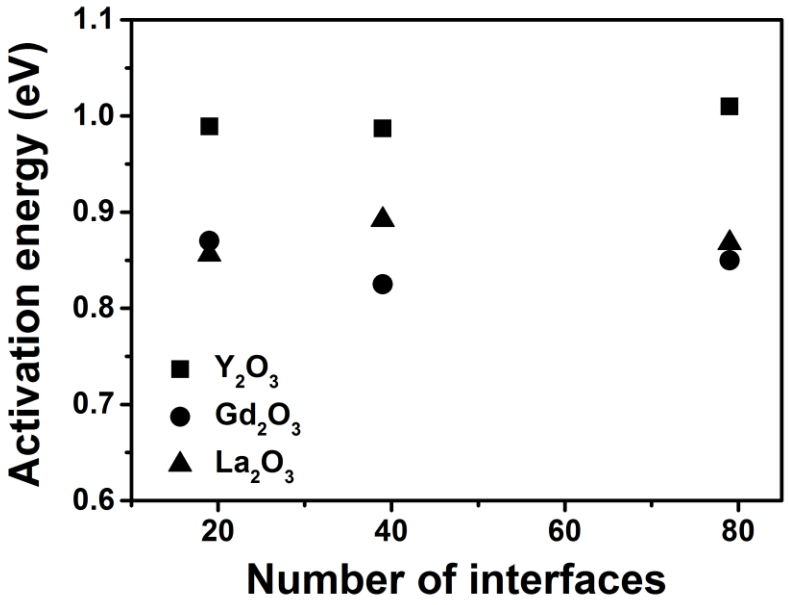

Figure 44 Activation energy of heterogeneously doped films composed of CeO_2 with Y_2O_3, Gd_2O_3, or La_2O_3 as a function of the number of interfaces

Figure 45 shows the activation energy of the three different types of heterogeneously doped CeO_2 films as a function of the lattice mismatch between RE_2O_3 and CeO_2. The activation energy of the Gd_2O_3/CeO_2 samples was about 0.85 eV, and the activation energy of the La_2O_3/CeO_2 samples was about 0.87 eV. The similarity in these activation energies with each other and with that of very lightly doped ceria (≈0.90 eV) [38], gives strong indication that either the lattice mismatch between La_2O_3 and CeO_2 is not creating a significant amount of tensile strain in the CeO_2, or alternatively, that the migration energy of vacancies in the space charge regions is not strongly affected by tensile strain. On the other hand, the activation energy of the Y_2O_3/CeO_2 samples was about 1.0 eV, significantly larger than that of the other dopants. Thus, the lattice mismatch in the yttria-doped samples seems to

have created biaxial compressive strain in the space charge zones and has significantly increased the migration energy of oxygen vacancies therein.

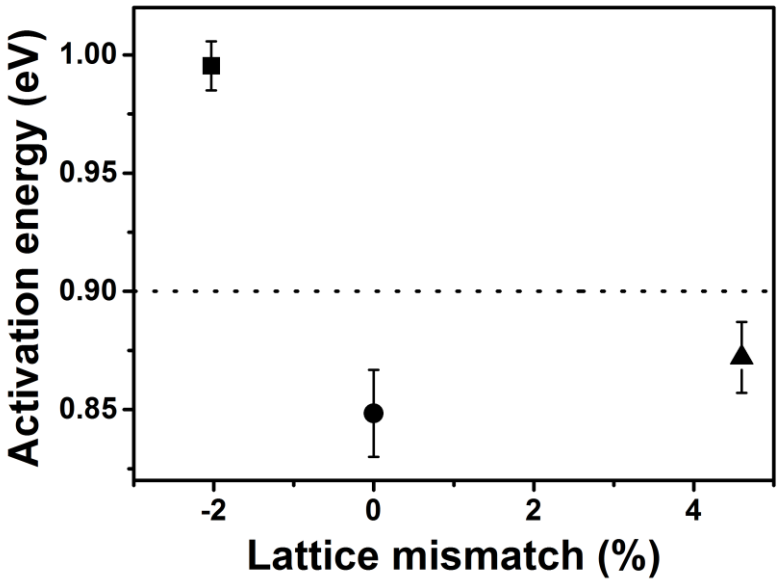

Figure 45 Activation energy of the $\sigma \cdot T$ product of the heterogeneously doped CeO_2 films as a function of the lattice parameter mismatch between the dopant and CeO_2. Note that the lattice mismatch is calculated based on the Equation (7) in which *a* represents the lattice parameter. The dotted line represents the activation energy of very lightly doped CeO_2 with 0.05 mol% Y_2O_3 [38].

Figure 46 shows the conductivity per interface of the three different types of heterogeneously doped CeO_2 films as a function of the temperature. The value of the conductivity per interface was obtained from the slope of the linear fit of the conductivity as a function of interfaces in Figure 34. From the figure, it can be clearly seen that the total conductivity increased from Y_2O_3 to Gd_2O_3 to La_2O_3. Based on the analysis of the activation energy in Figure 45, the migration energy and the mobility of the vacancies in space charge regions adjacent to Gd_2O_3 or La_2O_3 are likely to be

similar. The conductivities of La_2O_3/CeO_2 films, however, were consistently about 2 times larger relative to those of the Gd_2O_3/CeO_2 films. If these two types of films indeed possess the same vacancy mobility, then there must be ≈ 2 times more oxygen vacancies in the space charge regions adjacent to La_2O_3.

The actual mechanism behind an increased vacancy concentration in La_2O_3 space charge regions remains unclear. It may be that the migration of oxygen across the RE_2O_3/CeO_2 interface was more facile for La_2O_3 relative to Gd_2O_3. This may result from ion-ion interactions or lattice dynamical effects [41, 63]. Another clear difference between La_2O_3 and Gd_2O_3 is their lattice parameters. For Gd_2O_3/CeO_2 films, there is almost no lattice mismatch at the interfaces, but for La_2O_3/CeO_2, strain is expected: tensile in the CeO_2 and compressive in the La_2O_3. An increase in charge carrier concentration is possible to be due to greater strain gradient across the RE_2O_3/CeO_2 interfaces. It has been well established that the creation of a vacancy in fluorites yields an expansion of the lattice [64]. Therefore, a negative lattice strain gradient, with the RE_2O_3 under compression and CeO_2 under tension, provided driving force to transfer vacancies across the interface into the ceria. Since the CeO_2 layers were thicker than the 1 nm-thick RE_2O_3, the strain may be mostly borne by the RE_2O_3, pushing more oxygen vacancies from the highly compressive strained-La_2O_3 into the CeO_2 layers, increasing the vacancy concentration in space charge regions. A similar explanation was also proposed by Fronzi et al. in a numerical study of defect formation at ZrO_2-CeO_2 interfaces [62]. In that work, tensile strain in ZrO_2 significantly decreased the vacancy formation energy, while the compressive strain in CeO_2 significantly increased it. A similar change in vacancy formation energy here

would provide a driving force for the transfer of oxygen vacancies from the compressive-strained La_2O_3 into the tensile-strained CeO_2.

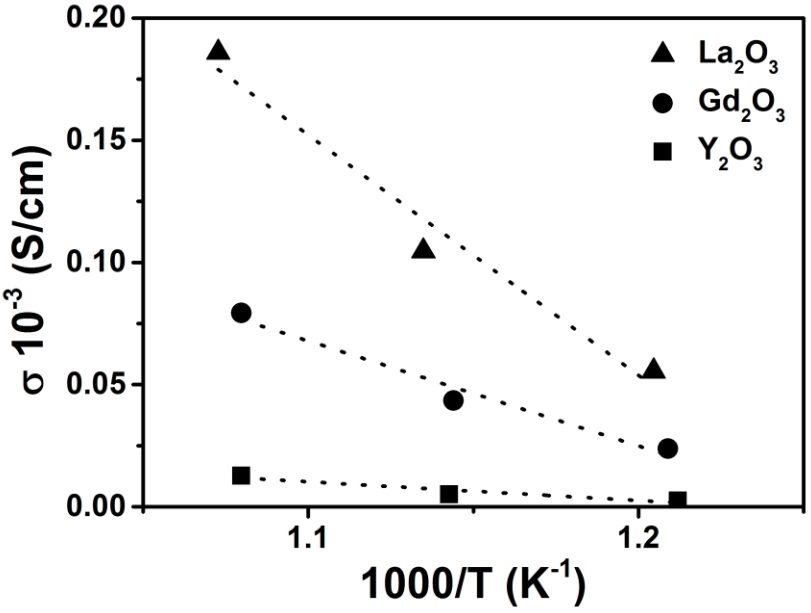

Figure 46 The conductivity per interface obtained from the slope of linear fit of the conductivity as a function of interfaces in Figure 34.

Chapter 5

CONCLUSIONS

5.1 Summary

We recently developed a novel thin film deposition method that allows the creation of metal oxide thin films within a solid solution space where the cation composition is controlled at the single nanometer level. This capability significantly expands the extension of the experimental space beyond what can be captured with the traditional models. In this dissertation, two different types of heterogeneous films fabricated by a sputtering technique were used to study (1) the effect of lattice mismatch strain and (2) the effects of vacancies being trapped within planar space charge regions on the oxygen ion conduction behavior in fluorite-structured materials.

Multilayers composed of YDC or YSZ with CZO45, CZO30, or CeO_2 have been prepared to systematically study the effects of compressive or tensile strains on oxygen ion conductivity. The existence of compressive strain in the YDC layers caused fairly drastic reductions in the ionic conductivity. The conductivity of YDC/CZO45 multilayers with lattice mismatch of -2.2% was monotonically decreased by at least one order of magnitude as the individual layer thickness approached interface sizes. As the lattice mismatch was decreased from -1.5% to near-zero for YDC/CZO30 to YDC/CeO_2 multilayers, the conductivity approached that of bulk YDC. Reduced compressive strain yielded conductivity near the bulk value, giving further confidence that it was the compressive strain that responsible for the decreased conductivity.

From a practical standpoint, the use of tensile strain to increase ionic conductivity is more useful. Multilayers consisting of YSZ and CZO provided means to study the effect of tensile strain on oxygen ion conductivity. By decreasing the individual layer thickness from 35 nm to 5 nm, very little conductivity change was found in the multilayers with lattice mismatch ranged between 2.9% and 5.2%, with the conductivity values near that of bulk YSZ. Based on the calculated out-of-plane YSZ lattice parameters and the strong superlattice peaks in the diffraction patterns, it is believed that the lattice mismatch strain in the multilayers has been relaxed by the creation of incoherent interface structures. For YSZ/CZO45 multilayers, the lattice mismatch of +2.9%, was very similar as that of previously reported YSZ/Y_2O_3 multilayers, suggesting that biaxial strains of this magnitude represent a rough upper practical limit. The energetic tradeoff between maintenance of mismatch strain and the nucleation of stress-relieving dislocations is likely to play a large role in determining the efficacy of using lattice mismatch to induce atomic strain and, thereby affect the ionic conductivity.

The effects of heterogeneous doping on the oxygen ion conductivity have been extensively studied using CeO_2-based thin films. The activation energies were found to be consistent with conduction entirely within the doped layers until the dopants were entirely condensed into layers of RE_2O_3 within layers of pure CeO_2. A Gouy-Chapman model was applied to calculate the distribution of oxygen vacancies in the space charge regions of the CeO_2 layers and the excess conductance induced there by the accumulated or trapped vacancies. The value of excess conductance in space charge regions was found to be similar to that of the whole multilayer, indicating that

the vacancies in the space charge regions of CeO_2 layers became dominant in the ionic conduction of the whole multilayer.

The effects of lattice mismatch strain on the heterogeneously doped CeO_2 films were further studied by using films with alternating layers of CeO_2 with 1 nm thick dopant oxides of Y_2O_3, Gd_2O_3, or La_2O_3. At the same number of RE_2O_3/CeO_2 interfaces, the total oxygen ion conductivity of these films was increased in the order $La_2O_3>Gd_2O_3>Y_2O_3$. The previously-used Gouy-Chapman model was no longer sufficient to fully explain the ion conduction behavior of heterodoped films. Two effects of the lattice mismatch were suggested. First, compressive strain in CeO_2 decreases the oxygen vacancy mobility in Y_2O_3/CeO_2 films, as evidenced by an increased activation energy of conduction. The decreased conductivity due to the presence of compressive strain was also observed in the multilayers composed of YDC and CZO. Second, strain gradients at the interfaces are suggested to cause more oxygen vacancies to be transferred into the CeO_2 space charge regions in the La_2O_3/CeO_2 films. More work is needed to clarify the mechanism(s) behind the conductivity increase in CeO_2 heterodoped with La_2O_3 relative to Gd_2O_3 and to see whether further increases in the conductivity of heterogeneously doped CeO_2 are possible. Such investigations are merited by the fact that the conductivity of these heterogeneously doped systems is already approaching the conductivity of optimal, homogenously doped systems. Taking advantage of strain gradients and high net dopant content in heterogeneously doped materials may indicate a route to significantly increase solid electrolyte conductivity over what is achievable with traditional doping strategies.

5.2 Recommendations for Future Work

There are some questions raised in this dissertation, however, still not answered due to the time limitation. Some research directions for the further study are suggested as follows:

(1) The presence of compressive strain in YDC layers can significantly decrease the oxygen ion conductivity, but at the same time, little change of oxygen ion conductivity was observed in YSZ/CZO multilayers with different lattice mismatches and different layer thicknesses. The calculated out-of-plane lattice parameters of YSZ from the XRD patterns shown in Figure 22 indicated that the interfacial strain in YSZ layers might be relaxed into misfit dislocations. In order to verify this assumption, we need to use TEM to visualize the cross-section of the YDC/CZO and YSZ/CZO multilayered samples. By comparing the interfacial structures between these two different types of multilayers, it would be much more helpful to further correlate the interfacial effects with the measured oxygen ion conductivity in this work.

(2) The effects of tensile strain on the oxygen ion conductivity in YSZ, however, still remain unclear in this work. The smallest lattice mismatch used here was about +2.9% for YSZ/CZO45 multilayers, but the interfacial strain might be still considered to be relaxed due to the large lattice mismatch. In order to further study the effects of tensile strain, we need to further decrease the interfacial lattice mismatch, creating coherent interfaces. One of the possible means is to further increase the Zr content in the CZO solid solution to decrease its lattice parameter. One of the main problems of using CZO with higher Zr concentration is that the crystal structure of CZO will be gradually changed from cubic to tetragonal, and to monoclinic, which may complicate the explanation of the experimental results. One of the most promising means is to use multilayers composed of $Ce_{1-x-z}Zr_xD_zO_{2-z/2}$ (D = Y, or Gd, or

La) and $Ce_{0.50}Zr_{0.50}O_2$ (CZO50) to study the effects of tensile strain on oxygen ion conductivity. The addition of dopants in the CeO_2-ZrO_2 solid solutions can stabilize the cubic phase into the room temperature. By fixing the dopant content, *z*, in the $Ce_{1-x-z}Zr_xD_zO_{2-z/2}$ at constant, the lattice mismatch at $Ce_{1-x-z}Zr_xD_zO_{2-z/2}$/CZO50 interfaces can be varied by adjusting the Ce/Zr atomic ratio. The lattice mismatch at interfaces can be changed from about -2.5 to +2.5 by varying *x* from 0 to 1.

(3) As shown in Figure 29, the Y_2O_3/CeO_2 heterodoped film adopted columnar crystal structure. The existence of the grain boundaries was found not to interrupt the 1 nm-thick Y_2O_3. We assumed that the model remained valid and the grain boundaries would only affect the vacancy mobility in the space charge regions when they crossed the grain boundaries. In order to verify this assumption, we need to create epitaxial heterodoped films eliminating the existence of grain boundaries. One means is to use a different substrate other than Al_2O_3. The MgO substrate deposited with a very thin $SrTiO_3$ buffer layer has been reported to have a good lattice mismatch with CeO_2, creating epitaxial multilayered films [55].

(4) Figure 33(d) compares the conductivity of CeO_2 heterodoped with La_2O_3 where the net dopant content was varied by keeping the thickness of La_2O_3 layers at 1 nm but decreasing the CeO_2 layer thickness from 19 nm to4 nm. The net dopant content is 5% (bilayers of 1 nm La_2O_3, 19 nm CeO_2), 10% (bilayers of 1 nm La_2O_3, 9 nm CeO_2), or 20% (bilayers of 1 nm La_2O_3, 4 nm CeO_2). Though the net dopant content increased significantly, the action energy of conduction did not change from ≈ 0.9 eV. The conductivity scales linearly with the dopant content. The conductivity of the 20% heterodoped sample was nearly the same as a homogeneously doped film with optimal dopant content: $Ce_{0.85}La_{0.15}O_\delta$. Higher conductivity may be achieved by

further decreasing the layer thickness of CeO_2 to increase the number of RE_2O_3/CeO_2 interfaces but before the action energy of conduction increases significantly. Moreover, choosing another RE_2O_3 with larger lattice parameter compared to that of La_2O_3 may also be helpful to further increase the oxygen ion conductivity.

REFERENCES

1. Radler, M. and L. Bell, *Economic growth boosting US, global energy demand.* Oil & Gas Journal, 2007. **105**(25): p. 18-27.
2. Snedden, R., *Energy from fossil fuels*. Rev. and updated. ed. Essential energy. 2006, Chicago, Ill.: Heinemann Library.
3. Andres, R.J., et al., *Carbon dioxide emissions from fossil-fuel use, 1751-1950.* Tellus Series B-Chemical and Physical Meteorology, 1999. **51**(4): p. 759-765.
4. Hameed, S. and J. Dignon, *Global Emissions of Nitrogen and Sulfur-Oxides in Fossil-Fuel Combustion 1970-1986.* Journal of the Air & Waste Management Association, 1992. **42**(2): p. 159-163.
5. Brunekreef, B. and S.T. Holgate, *Air pollution and health.* The Lancet, 2002. **360**(9341): p. 1233-1242.
6. Joos, F., et al., *Global warming and marine carbon cycle feedbacks an future atmospheric CO2.* Science, 1999. **284**(5413): p. 464-467.
7. Wuebbles, D.J. and A.K. Jain, *Concerns about climate change and the role of fossil fuel use.* Fuel Processing Technology, 2001. **71**(1-3): p. 99-119.
8. http://en.wikipedia.org/wiki/Great_Smog.
9. Shafiee, S. and E. Topal, *When will fossil fuel reserves be diminished?* Energy Policy, 2009. **37**(1): p. 181-189.
10. Chapman, I., *The end of Peak Oil? Why this topic is still relevant despite recent denials.* Energy Policy, 2014. **64**: p. 93-101.
11. Dresselhaus, M.S. and I.L. Thomas, *Alternative energy technologies.* Nature, 2001. **414**(6861): p. 332-337.
12. Goldemberg, J., *The promise of clean energy.* Energy Policy, 2006. **34**(15): p. 2185-2190.
13. http://www.eia.gov/forecasts/aeo/er/early_fuel.cfm.
14. Lutsey, N., *A technical analysis of model year 2011 US automobile efficiency.* Transportation Research Part D-Transport and Environment, 2012. **17**(5): p. 361-369.
15. Grove, W.R., *XXIV. On voltaic series and the combination of gases by platinum.* Philosophical Magazine Series 3, 1839. **14**(86): p. 127-130.
16. Carrette, L., K.A. Friedrich, and U. Stimming, *Fuel Cells: Principles, Types, Fuels, and Applications.* ChemPhysChem, 2000. **1**(4): p. 162-193.
17. Stambouli, A.B. and E. Traversa, *Fuel cells, an alternative to standard sources of energy.* Renewable & Sustainable Energy Reviews, 2002. **6**(3): p. 295-304.

18. Steele, B.C.H. and A. Heinzel, *Materials for fuel-cell technologies.* Nature, 2001. **414**(6861): p. 345-352.
19. Ellis, M.W., M.R. Von Spakovsky, and D.J. Nelson, *Fuel cell systems: Efficient, flexible energy conversion for the 21st century.* Proceedings of the Ieee, 2001. **89**(12): p. 1808-1818.
20. Minh, N.Q., *Ceramic Fuel-Cells.* Journal of the American Ceramic Society, 1993. **76**(3): p. 563-588.
21. Fabbri, E., D. Pergolesi, and E. Traversa, *Materials challenges toward proton-conducting oxide fuel cells: a critical review.* Chemical Society Reviews, 2010. **39**(11): p. 4355-4369.
22. Nernst, W., *On the electrolytic conduction of solid bodies at high temperatures.* Z. Electrochem, 1899. **6**(2): p. 41-43.
23. Nernst, W., *Glower for electric lamps*. 1901, Google Patents.
24. Möbius, H.-H., *On the history of solid electrolyte fuel cells.* Journal of Solid State Electrochemistry, 1997. **1**(1): p. 2-16.
25. Zhu, W.Z. and S.C. Deevi, *A review on the status of anode materials for solid oxide fuel cells.* Materials Science and Engineering a-Structural Materials Properties Microstructure and Processing, 2003. **362**(1-2): p. 228-239.
26. Mogensen, M. and K. Kammer, *Conversion of hydrocarbons in solid oxide fuel cells.* Annual Review of Materials Research, 2003. **33**: p. 321-331.
27. Li, H., et al., *A review of water flooding issues in the proton exchange membrane fuel cell.* Journal of Power Sources, 2008. **178**(1): p. 103-117.
28. Wachsman, E.D., C.A. Marlowe, and K.T. Lee, *Role of solid oxide fuel cells in a balanced energy strategy.* Energy & Environmental Science, 2012. **5**(2): p. 5498-5509.
29. Brett, D.J.L., et al., *Intermediate temperature solid oxide fuel cells.* Chemical Society Reviews, 2008. **37**(8): p. 1568-1578.
30. Wachsman, E.D. and K.T. Lee, *Lowering the Temperature of Solid Oxide Fuel Cells.* Science, 2011. **334**(6058): p. 935-939.
31. Doshi, R., et al., *Development of solid-oxide fuel cells that operate at 500 degrees C.* Journal of the Electrochemical Society, 1999. **146**(4): p. 1273-1278.
32. Arachi, Y., et al., *Electrical conductivity of the ZrO2–Ln2O3 (Ln=lanthanides) system.* Solid State Ionics, 1999. **121**(1–4): p. 133-139.
33. Figueiredo, F.M.L. and F.M.B. Marques, *Electrolytes for solid oxide fuel cells.* Wiley Interdisciplinary Reviews: Energy and Environment, 2013. **2**(1): p. 52-72.
34. Scott, H.G., *Phase-Relationships in the Magnesia-Yttria-Zirconia System.* Journal of the Australasian Ceramic Society, 1981. **17**(1): p. 16-20.
35. Singhal, S.C. and K. Kendall, *High-temperature solid oxide fuel cells : fundamentals, design, and applicatons*. 2003, New York: Elsevier Advanced Technology.
36. Kilner, J.A., *Fast oxygen transport in acceptor doped oxides.* Solid State Ionics, 2000. **129**(1-4): p. 13-23.

37. Inaba, H. and H. Tagawa, *Ceria-based solid electrolytes.* Solid State Ionics, 1996. **83**(1–2): p. 1-16.
38. Wang, D.Y., et al., *Oxygen-Ion Conductivity and Defect Interactions in Yttria-Doped Ceria.* Solid State Ionics, 1981. **2**(2): p. 95-105.
39. Adler, S.B. and J.W. Smith, *Effects of Long-Range Forces on Oxygen-Transport in Yttria-Doped Ceria - Simulation and Theory.* Journal of the Chemical Society-Faraday Transactions, 1993. **89**(16): p. 3123-3128.
40. Rushton, M.J.D., et al., *Effect of strain on the oxygen diffusion in yttria and gadolinia co-doped ceria.* Solid State Ionics, 2013. **230**: p. 37-42.
41. Burbano, M., et al., *Oxygen Vacancy Ordering and the Conductivity Maximum in Y2O3-Doped CeO2.* Chemistry of Materials, 2012. **24**(1): p. 222-229.
42. Yamamoto, O., *Solid oxide fuel cells: fundamental aspects and prospects.* Electrochimica Acta, 2000. **45**(15-16): p. 2423-2435.
43. Zhang, Y.W., et al., *Sol-gel fabrication and electrical property of nanocrystalline (RE2O3)(0.08)(ZrO2)(0.92) (RE = Sc, Y) thin films.* Chemistry of Materials, 2001. **13**(2): p. 372-378.
44. Tuller, H.L., *Ionic conduction in nanocrystalline materials.* Solid State Ionics, 2000. **131**(1-2): p. 143-157.
45. Maier, J., *Nanoionics: ion transport and electrochemical storage in confined systems.* Nature Materials, 2005. **4**(11): p. 805-815.
46. Ramanathan, S., *Interface-mediated ultrafast carrier conduction in oxide thin films and superlattices for energy.* Journal of Vacuum Science & Technology A, 2009. **27**(5): p. 1126-1134.
47. Guo, X.X. and J. Maier, *Ionically Conducting Two-Dimensional Heterostructures.* Advanced Materials, 2009. **21**(25-26): p. 2619-2631.
48. Garcia-Barriocanal, J., et al., *Tailoring Disorder and Dimensionality: Strategies for Improved Solid Oxide Fuel Cell Electrolytes.* ChemPhysChem, 2009. **10**(7): p. 1003-1011.
49. Fabbri, E., D. Pergolesi, and E. Traversa, *Ionic conductivity in oxide heterostructures: the role of interfaces.* Science and Technology of Advanced Materials, 2010. **11**(5).
50. Guo, X., *Can we achieve significantly higher ionic conductivity in nanostructured zirconia?* Scripta Materialia, 2011. **65**(2): p. 96-101.
51. Sata, N., et al., *Mesoscopic fast ion conduction in nanometre-scale planar heterostructures.* Nature, 2000. **408**(6815): p. 946-949.
52. Guo, X.X. and J. Maier, *Comprehensive Modeling of Ion Conduction of Nanosized CaF2/BaF2 Multilayer Heterostructures.* Advanced Functional Materials, 2009. **19**(1): p. 96-101.
53. Guo, X.X., et al., *Defect chemical modeling of mesoscopic ion conduction in nanosized CaF2/BaF2 multilayer heterostructures.* Physical Review B, 2007. **76**(12).

54. Azad, S., et al., *Nanoscale effects on ion conductance of layer-by-layer structures of gadolinia-doped ceria and zirconia.* Applied Physics Letters, 2005. **86**(13).
55. Sanna, S., et al., *Enhancement of Ionic Conductivity in Sm-Doped Ceria/Yttria-Stabilized Zirconia Heteroepitaxial Structures.* Small, 2010. **6**(17): p. 1863-1867.
56. Li, B., et al., *Multilayered YSZ/GZO films with greatly enhanced ionic conduction for low temperature solid oxide fuel cells.* Physical Chemistry Chemical Physics, 2013. **15**(4): p. 1296-1301.
57. Korte, C., et al., *Ionic conductivity and activation energy for oxygen ion transport in superlattices - the semicoherent multilayer system YSZ (ZrO(2)+9.5 mol% Y(2)O(3))/Y(2)O(3).* Physical Chemistry Chemical Physics, 2008. **10**(31): p. 4623-4635.
58. Schichtel, N., et al., *On the influence of strain on ion transport: microstructure and ionic conductivity of nanoscale YSZ vertical bar Sc2O3 multilayers.* Physical Chemistry Chemical Physics, 2010. **12**(43): p. 14596-14608.
59. Korte, C., et al., *Influence of interface structure on mass transport in phase boundaries between different ionic materials Experimental studies and formal considerations.* Monatshefte Fur Chemie, 2009. **140**(9): p. 1069-1080.
60. Schichtel, N., et al., *Elastic strain at interfaces and its influence on ionic conductivity in nanoscaled solid electrolyte thin films-theoretical considerations and experimental studies.* Physical Chemistry Chemical Physics, 2009. **11**(17): p. 3043-3048.
61. Kushima, A. and B. Yildiz, *Oxygen ion diffusivity in strained yttria stabilized zirconia: where is the fastest strain?* Journal of Materials Chemistry, 2010. **20**(23): p. 4809-4819.
62. Fronzi, M., et al., *Ab initio investigation of defect formation at ZrO2-CeO2 interfaces.* Physical Review B, 2012. **86**(8).
63. Buckeridge, J., et al., *Dynamical response and instability in ceria under lattice expansion.* Physical Review B, 2013. **87**(21).
64. Marrocchelli, D., et al., *Understanding Chemical Expansion in Non-Stoichiometric Oxides: Ceria and Zirconia Case Studies.* Advanced Functional Materials, 2012. **22**(9): p. 1958-1965.
65. Garcia-Barriocanal, J., et al., *Colossal ionic conductivity at interfaces of epitaxial ZrO2 : Y2O3/SrTiO3 heterostructures.* Science, 2008. **321**(5889): p. 676-680.
66. Guo, X., *Comment on "Colossal Ionic Conductivity at Interfaces of Epitaxial ZrO2:Y2O3/SrTiO3 Heterostructures".* Science, 2009. **324**(5926).
67. Cavallaro, A., et al., *Electronic nature of the enhanced conductivity in YSZ-STO multilayers deposited by PLD.* Solid State Ionics, 2010. **181**(13-14): p. 592-601.

68. Garcia-Barriocanal, J., et al., *Response to Comment on "Colossal Ionic Conductivity at Interfaces of Epitaxial ZrO2:Y2O3/SrTiO3 Heterostructures".* Science, 2009. **324**(5926).
69. Pergolesi, D., et al., *Tensile Lattice Distortion Does Not Affect Oxygen Transport in Yttria-Stabilized Zirconia-CeO2 Heterointerfaces.* Acs Nano, 2012. **6**(12): p. 10524-10534.
70. Peters, A., et al., *Ionic conductivity and activation energy for oxygen ion transport in superlattices - The multilayer system CSZ (ZrO2+CaO)/Al2O3.* Solid State Ionics, 2007. **178**(1-2): p. 67-76.
71. Jiang, J., W.D. Shen, and J.L. Hertz, *Fabrication of epitaxial zirconia and ceria thin films with arbitrary dopant and host atom composition.* Thin Solid Films, 2012. **522**: p. 66-70.
72. Rao, G.R. and H.R. Sahu, *XRD and UV-Vis diffuse reflectance analysis of CeO2-ZrO2 solid solutions synthesized by combustion method.* Proceedings of the Indian Academy of Sciences-Chemical Sciences, 2001. **113**(5-6): p. 651-658.
73. Lau, K.C., C.H. Turner, and B.I. Dunlap, *Kinetic Monte Carlo simulation of the Yttria Stabilized Zirconia (YSZ) fuel cell cathode.* Solid State Ionics, 2008. **179**(33–34): p. 1912-1920.
74. Bhuiyan, M.S., et al., *MOD approach for the growth of epitaxial CeO2 buffer layers on biaxially textured Ni-W substrates for YBCO coated conductors.* Superconductor Science & Technology, 2003. **16**(11): p. 1305-1309.
75. Kuhn, M., et al., *Structural characterization and oxygen nonstoichiometry of ceria-zirconia (Ce1-xZrxO2-delta) solid solutions.* Acta Materialia, 2013. **61**(11): p. 4277-4288.
76. Meneghesso, G., et al., *Evidence of interface trap creation by hot-electrons in AlGaAs/GaAs high electron mobility transistors.* Applied Physics Letters, 1996. **69**(10): p. 1411-1413.
77. Briggs, D., *Surface analysis of polymers by XPS and static SIMS*. Digitally printed 1st pbk. ed. Cambridge solid state science series. 2005, Cambridge ; New York: Cambridge University Press. xiv, 198 p.
78. Chen, L., et al., *Electrical properties of a highly oriented, textured thin film of the ionic conductor Gd:CeO2−δ on (001) MgO.* Applied Physics Letters, 2003. **83**(23): p. 4737-4739.
79. Tuller, H.L., S.J. Litzelman, and W. Jung, *Micro-ionics: next generation power sources.* Physical Chemistry Chemical Physics, 2009. **11**(17): p. 3023-3034.
80. Jorcin, J.B., et al., *CPE analysis by local electrochemical impedance spectroscopy.* Electrochimica Acta, 2006. **51**(8-9): p. 1473-1479.
81. Zoltowski, P., *On the electrical capacitance of interfaces exhibiting constant phase element behaviour.* Journal of Electroanalytical Chemistry, 1998. **443**(1): p. 149-154.

82. Irvine, J.T.S., D.C. Sinclair, and A.R. West, *Electroceramics: Characterization by Impedance Spectroscopy.* Advanced Materials, 1990. **2**(3): p. 132-138.
83. Zhang, F., et al., *Phases in ceria-zirconia binary oxide (1-x)CeO2-xZrO(2) nanoparticles: The effect of particle size.* Journal of the American Ceramic Society, 2006. **89**(3): p. 1028-1036.
84. Hori, C.E., et al., *Thermal stability of oxygen storage properties in a mixed CeO2-ZrO2 system.* Applied Catalysis B: Environmental, 1998. **16**(2): p. 105-117.
85. Fu, Y.P., S.H. Hu, and B.L. Liu, *Structure characterization and mechanical properties of CeO2-ZrO2 solid solution system.* Ceramics International, 2009. **35**(8): p. 3005-3011.
86. Inaba, H. and H. Tagawa, *Ceria-based solid electrolytes - Review.* Solid State Ionics, 1996. **83**(1-2): p. 1-16.
87. Hayashi, H., et al., *Molecular dynamics calculations on ceria-based solid electrolytes with different radius dopants.* Solid State Ionics, 2000. **131**(3-4): p. 281-290.
88. Kosacki, I., et al., *Electrical conductivity of nanocrystalline ceria and zirconia thin films.* Solid State Ionics, 2000. **136**: p. 1225-1233.
89. Suzuki, T., I. Kosacki, and H.U. Anderson, *Microstructure-electrical conductivity relationships in nanocrystalline ceria thin films.* Solid State Ionics, 2002. **151**(1-4): p. 111-121.
90. Jiang, J., et al., *Improved ionic conductivity in strained yttria-stabilized zirconia thin films.* Applied Physics Letters, 2013. **102**(14).
91. Kosacki, I. and H.U. Anderson, *Microstructure - Property Relationships in Nanocrystalline Oxide Thin Films.* Ionics, 2000. **6**(3-4): p. 294-311.
92. Rührup, V. and H.-D. Wiemhöfer, *Ionic Conductivity of Gd-and Y-Doped Ceria-Zirconia Solid Solutions.* Verlag der Zeitschrift für Naturforschung, 2006, **61b**: p. 916-922.
93. Atkinson, A. and A. Selcuk, *Mechanical behaviour of ceramic oxygen ion-conducting membranes.* Solid State Ionics, 2000. **134**(1-2): p. 59-66.
94. Tarancon, A., et al., *A Molecular Dynamics Study on the Oxygen Diffusion in Doped Fluorites: The Effect of the Dopant Distribution.* Fuel Cells, 2011. **11**(1): p. 26-37.
95. Beche, E., et al., *Ce 3d XPS investigation of cerium oxides and mixed cerium oxide (CexTiyOz).* Surface and Interface Analysis, 2008. **40**(3-4): p. 264-267.
96. Hanic, F., et al., *Real structure of undoped Y2O3 single crystals.* Acta Crystallographica Section B, 1984. **40**(2): p. 76-82.
97. Ando, K., et al., *Oxygen Self-Diffusion in Single-Crystal Y2o3.* Journal of the American Ceramic Society, 1983. **66**(12): p. C222-C223.
98. Gonzalez-Romero, R.L., et al., *Cation diffusion in yttria-zirconia by molecular dynamics.* Solid State Ionics, 2011. **204**: p. 1-6.

99. Perkins, J.M., et al., *Anomalous Oxidation States in Multilayers for Fuel Cell Applications.* Advanced Functional Materials, 2010. **20**(16): p. 2664-2674.
100. Paranthaman, M., et al., *Growth of biaxially textured buffer layers on rolled-Ni substrates by electron beam evaporation.* Physica C: Superconductivity, 1997. **275**(3–4): p. 266-272.
101. Rockenhäuser, C., et al., *Microstructure evolution and cation interdiffusion in thin Gd2O3 films on CeO2 substrates.* Journal of the European Ceramic Society, 2014. **34**(5): p. 1235-1242.
102. Izuki, M., et al., *Interfacial stability and cation diffusion across the LSCF/GDC interface.* Journal of Power Sources, 2011. **196**(17): p. 7232-7236.
103. Wirkus, C.D., M.F. Berard, and D.R. Wilder, *Oxygen Diffusion in Gd2O3.* Journal of the American Ceramic Society, 1969. **52**(8): p. 456-456.
104. Gerhardt-Anderson, R. and A.S. Nowick, *Ionic conductivity of CeO2 with trivalent dopants of different ionic radii.* Solid State Ionics, 1981. **5**(0): p. 547-550.
105. Yoshida, H., et al., *Investigation of the relationship between the ionic conductivity and the local structures of singly and doubly doped ceria compounds using EXAFS measurement.* Solid State Ionics, 2001. **140**(3–4): p. 191-199.
106. Omar, S., et al., *Crystal Structure–Ionic Conductivity Relationships in Doped Ceria Systems.* Journal of the American Ceramic Society, 2009. **92**(11): p. 2674-2681.
107. Kouda, M., et al., *Charged defects reduction in gate insulator with multivalent materials.* 2009 Symposium on Vlsi Technology, Digest of Technical Papers, 2009: p. 200-201.
108. Wong, H., et al., *XPS Study of the Bonding Properties of Lanthanum Oxide/Silicon Interface with a Trace Amount of Nitrogen Incorporation.* Journal of the Electrochemical Society, 2010. **157**(2): p. G49-G52.
109. Wong, H., et al., *Subthreshold Characteristics of MOS Transistors With CeO2/La2O3 Stacked Gate Dielectric.* Ieee Electron Device Letters, 2011. **32**(8): p. 1002-1004.
110. Wong, H., et al., *Current conduction and stability of CeO2/La2O3 stacked gate dielectric.* Applied Physics Letters, 2012. **101**(23).
111. Sebastian, M.T., et al., *Microwave dielectric properties of (1−x)CeO2–xCaTiO3 and (1−x)CeO2–xSm2O3 ceramics.* Journal of the European Ceramic Society, 2004. **24**(9): p. 2583-2589.
112. Kosacki, I., et al., *Raman spectroscopy of nanocrystalline ceria and zirconia thin films.* Journal of the American Ceramic Society, 2002. **85**(11): p. 2646-2650.
113. Gobel, M.C., et al., *Boundary effects on the electrical conductivity of pure and doped cerium oxide thin films.* Physical Chemistry Chemical Physics, 2010. **12**(42): p. 14351-14361.

114. Hwang, J.H. and T.O. Mason, *Defect chemistry and transport properties of nanocrystalline cerium oxide.* Zeitschrift Fur Physikalische Chemie-International Journal of Research in Physical Chemistry & Chemical Physics, 1998. **207**: p. 21-38.
115. Maier, J., *Space-Charge Regions in Solid 2-Phase Systems and Their Conduction Contribution .3. Defect Chemistry and Ionic-Conductivity in Thin-Films.* Solid State Ionics, 1987. **23**(1-2): p. 59-67.
116. Tuller, H.L., *Mixed Ionic Electronic Conduction in a Number of Fluorite and Pyrochlore Compounds.* Solid State Ionics, 1992. **52**(1-3): p. 135-146.

Appendix A

REPRINT PERMISSION LETTERS

Permission letters for reprinting of figures 3, 4, 5, 6, 7, 8, 9, 10, 13, 14, and 16 were listed below.

Figure 3

ELSEVIER LICENSE
TERMS AND CONDITIONS

Jul 17, 201

This is a License Agreement between Weida Shen ("You") and Elsevier ("Elsevier") provided by Copyright Clearance Center ("CCC"). The license consists of your order details, the terms and conditions provided by Elsevier, and the payment terms and conditions.

All payments must be made in full to CCC. For payment instructions, please see information listed at the bottom of this form.

Supplier	Elsevier Limited The Boulevard,Langford Lane Kidlington,Oxford,OX5 1GB,UK
Registered Company Number	1982084
Customer name	Weida Shen
Customer address	126 Spencer Lab NEWARK, DE 19711
License number	3431420199549
License date	Jul 17, 2014
Licensed content publisher	Elsevier
Licensed content publication	Solid State Ionics
Licensed content title	Electrical conductivity of the ZrO2–Ln2O3(Ln=lanthanides) system
Licensed content author	Y. Arachi,H. Sakai,O. Yamamoto,Y. Takeda,N. Imanishai
Licensed content date	June 1999
Licensed content volume number	121
Licensed content issue number	1–4
Number of pages	7
Start Page	133
End Page	139
Type of Use	reuse in a thesis/dissertation
Intended publisher of new work	other
Portion	figures/tables/illustrations
Number of figures/tables/illustrations	1
Format	both print and electronic
Are you the author of this Elsevier article?	No
Will you be translating?	No
Title of your thesis/dissertation	STRAIN EFFECTS ON ION CONDUCTION IN HETEROGENEOUS OXIDE ELECTROLYTES
Expected completion date	Aug 2014
Estimated size (number of pages)	119
Elsevier VAT number	GB 494 6272 12
Permissions price	0.00 USD
VAT/Local Sales Tax	0.00 USD / 0.00 GBP
Total	0.00 USD
Terms and Conditions	

Figure 4

ELSEVIER LICENSE
TERMS AND CONDITIONS

Jul 17, 2014

This is a License Agreement between Weida Shen ("You") and Elsevier ("Elsevier") provided by Copyright Clearance Center ("CCC"). The license consists of your order details, the terms and conditions provided by Elsevier, and the payment terms and conditions.

All payments must be made in full to CCC. For payment instructions, please see information listed at the bottom of this form.

Supplier	Elsevier Limited The Boulevard,Langford Lane Kidlington,Oxford,OX5 1GB,UK
Registered Company Number	1982084
Customer name	Weida Shen
Customer address	126 Spencer Lab NEWARK, DE 19711
License number	3431420730922
License date	Jul 17, 2014
Licensed content publisher	Elsevier
Licensed content publication	Electrochimica Acta
Licensed content title	Solid oxide fuel cells: fundamental aspects and prospects
Licensed content author	Osamu Yamamoto
Licensed content date	3 May 2000
Licensed content volume number	45
Licensed content issue number	15–16
Number of pages	13
Start Page	2423
End Page	2435
Type of Use	reuse in a thesis/dissertation
Intended publisher of new work	other
Portion	figures/tables/illustrations
Number of figures/tables/illustrations	1
Format	both print and electronic
Are you the author of this Elsevier article?	No
Will you be translating?	No
Title of your thesis/dissertation	STRAIN EFFECTS ON ION CONDUCTION IN HETEROGENEOUS OXIDE ELECTROLYTES
Expected completion date	Aug 2014
Estimated size (number of pages)	119
Elsevier VAT number	GB 494 6272 12
Permissions price	0.00 USD
VAT/Local Sales Tax	0.00 USD / 0.00 GBP
Total	0.00 USD
Terms and Conditions	

Figure 5

NATURE PUBLISHING GROUP LICENSE TERMS AND CONDITIONS

Jul 17, 2014

This is a License Agreement between Weida Shen ("You") and Nature Publishing Group ("Nature Publishing Group") provided by Copyright Clearance Center ("CCC"). The license consists of your order details, the terms and conditions provided by Nature Publishing Group, and the payment terms and conditions.

All payments must be made in full to CCC. For payment instructions, please see information listed at the bottom of this form.

License Number	3431421113528
License date	Jul 17, 2014
Licensed content publisher	Nature Publishing Group
Licensed content publication	Nature
Licensed content title	Mesoscopic fast ion conduction in nanometre-scale planar heterostructures
Licensed content author	N. Sata, K. Eberman, K. Eberl and J. Maier
Licensed content date	Dec 21, 2000
Volume number	408
Issue number	6815
Type of Use	reuse in a dissertation / thesis
Requestor type	academic/educational
Format	print and electronic
Portion	figures/tables/illustrations
Number of figures/tables/illustrations	2
Figures	Figure 1 Figure 4
Author of this NPG article	no
Your reference number	None
Title of your thesis / dissertation	STRAIN EFFECTS ON ION CONDUCTION IN HETEROGENEOUS OXIDE ELECTROLYTES
Expected completion date	Aug 2014
Estimated size (number of pages)	119
Total	0.00 USD
Terms and Conditions	

JOHN WILEY AND SONS LICENSE TERMS AND CONDITIONS

Jul 17, 2014

This is a License Agreement between Weida Shen ("You") and John Wiley and Sons ("John Wiley and Sons") provided by Copyright Clearance Center ("CCC"). The license consists of your order details, the terms and conditions provided by John Wiley and Sons, and the payment terms and conditions.

All payments must be made in full to CCC. For payment instructions, please see information listed at the bottom of this form.

License Number	3431421365634
License date	Jul 17, 2014
Licensed content publisher	John Wiley and Sons
Licensed content publication	Advanced Functional Materials
Licensed content title	Comprehensive Modeling of Ion Conduction of Nanosized CaF2/BaF2 Multilayer Heterostructures
Licensed copyright line	Copyright © 2009 WILEY-VCH Verlag GmbH & Co. KGaA, Weinheim
Licensed content author	Xiangxin Guo,Joachim Maier
Licensed content date	Dec 8, 2008
Start page	96
End page	101
Type of use	Dissertation/Thesis
Requestor type	University/Academic
Format	Print and electronic
Portion	Figure/table
Number of figures/tables	1
Original Wiley figure/table number(s)	Figure 5
Will you be translating?	No
Title of your thesis / dissertation	STRAIN EFFECTS ON ION CONDUCTION IN HETEROGENEOUS OXIDE ELECTROLYTES
Expected completion date	Aug 2014
Expected size (number of pages)	119
Total	0.00 USD

Terms and Conditions

Figure 6

AIP PUBLISHING LLC LICENSE TERMS AND CONDITIONS

Jul 17, 2014

All payments must be made in full to CCC. For payment instructions, please see information listed at the bottom of this form.

License Number	3424340374984
Order Date	Jul 08, 2014
Publisher	AIP Publishing LLC
Publication	Applied Physics Letters
Article Title	Nanoscale effects on ion conductance of layer-by-layer structures of gadolinia-doped ceria and zirconia
Author	S. Azad,O. A. Marina,C. M. Wang, et al.
Online Publication Date	Mar 21, 2005
Volume number	86
Issue number	13
Type of Use	Thesis/Dissertation
Requestor type	Student
Format	Print and electronic
Portion	Figure/Table
Number of figures/tables	1
Title of your thesis / dissertation	STRAIN EFFECTS ON ION CONDUCTION IN HETEROGENEOUS OXIDE ELECTROLYTES
Expected completion date	Aug 2014
Estimated size (number of pages)	119
Total	0.00 USD

Terms and Conditions

Figure 7, Figure 8

ROYAL SOCIETY OF CHEMISTRY
LICENSE
TERMS AND CONDITIONS
Jul 17, 2014

This is a License Agreement between Weida Shen ("You") and Royal Society of Chemistry ("Royal Society of Chemistry") provided by Copyright Clearance Center ("CCC"). The license consists of your order details, the terms and conditions provided by Royal Society of Chemistry, and the payment terms and conditions.

All payments must be made in full to CCC. For payment instructions, please see information listed at the bottom of this form.

License Number	3431430691052
License date	Jul 17, 2014
Licensed content publisher	Royal Society of Chemistry
Licensed content publication	Physical Chemistry Chemical Physics
Licensed content title	Ionic conductivity and activation energy for oxygen ion transport in superlattices—the semicoherent multilayer system YSZ (ZrO2 + 9.5 mol% Y2O3)/Y2O3
Licensed content author	C. Korte,A. Peters,J. Janek,D. Hesse,N. Zakharov
Licensed content date	Jun 20, 2008
Volume number	10
Issue number	31
Type of Use	Thesis/Dissertation
Requestor type	academic/educational
Portion	figures/tables/images
Number of figures/tables/images	2
Format	print and electronic
Distribution quantity	10
Will you be translating?	no
Order reference number	None
Title of the thesis/dissertation	STRAIN EFFECTS ON ION CONDUCTION IN HETEROGENEOUS OXIDE ELECTROLYTES
Expected completion date	Aug 2014
Estimated size	119
Total	0.00 USD
Terms and Conditions	

Figure 9

ROYAL SOCIETY OF CHEMISTRY
LICENSE
TERMS AND CONDITIONS
Jul 17, 2014

This is a License Agreement between Weida Shen ("You") and Royal Society of Chemistry ("Royal Society of Chemistry") provided by Copyright Clearance Center ("CCC"). The license consists of your order details, the terms and conditions provided by Royal Society of Chemistry, and the payment terms and conditions.

All payments must be made in full to CCC. For payment instructions, please see information listed at the bottom of this form.

License Number	3431430998584
License date	Jul 17, 2014
Licensed content publisher	Royal Society of Chemistry
Licensed content publication	Physical Chemistry Chemical Physics
Licensed content title	Elastic strain at interfaces and its influence on ionic conductivity in nanoscaled solid electrolyte thin films—theoretical considerations and experimental studies
Licensed content author	N. Schichtel,C. Korte,D. Hesse,J. Janek
Licensed content date	Mar 20, 2009
Volume number	11
Issue number	17
Type of Use	Thesis/Dissertation
Requestor type	academic/educational
Portion	figures/tables/images
Number of figures/tables/images	1
Format	print and electronic
Distribution quantity	10
Will you be translating?	no
Order reference number	None
Title of the thesis/dissertation	STRAIN EFFECTS ON ION CONDUCTION IN HETEROGENEOUS OXIDE ELECTROLYTES
Expected completion date	Aug 2014
Estimated size	119
Total	0.00 USD
Terms and Conditions	

Figure 10

ROYAL SOCIETY OF CHEMISTRY
LICENSE
TERMS AND CONDITIONS
Jul 17, 2014

This is a License Agreement between Weida Shen ("You") and Royal Society of Chemistry ("Royal Society of Chemistry") provided by Copyright Clearance Center ("CCC"). The license consists of your order details, the terms and conditions provided by Royal Society of Chemistry, and the payment terms and conditions.

All payments must be made in full to CCC. For payment instructions, please see information listed at the bottom of this form.

License Number	3431431325417
License date	Jul 17, 2014
Licensed content publisher	Royal Society of Chemistry
Licensed content publication	Journal of Materials Chemistry
Licensed content title	Oxygen ion diffusivity in strained yttria stabilized zirconia: where is the fastest strain?
Licensed content author	Akihiro Kushima,Bilge Yildiz
Licensed content date	Apr 29, 2010
Volume number	20
Issue number	23
Type of Use	Thesis/Dissertation
Requestor type	academic/educational
Portion	figures/tables/images
Number of figures/tables/images	1
Format	print and electronic
Distribution quantity	10
Will you be translating?	no
Order reference number	None
Title of the thesis/dissertation	STRAIN EFFECTS ON ION CONDUCTION IN HETEROGENEOUS OXIDE ELECTROLYTES
Expected completion date	Aug 2014
Estimated size	119
Total	0.00 USD
Terms and Conditions	

Figure 13, Figure 14

ELSEVIER LICENSE
TERMS AND CONDITIONS

Jul 17, 2014

This is a License Agreement between Weida Shen ("You") and Elsevier ("Elsevier") provided by Copyright Clearance Center ("CCC"). The license consists of your order details, the terms and conditions provided by Elsevier, and the payment terms and conditions.

All payments must be made in full to CCC. For payment instructions, please see information listed at the bottom of this form.

Supplier	Elsevier Limited The Boulevard,Langford Lane Kidlington,Oxford,OX5 1GB,UK
Registered Company Number	1982084
Customer name	Weida Shen
Customer address	126 Spencer Lab NEWARK, DE 19711
License number	3431440001620
License date	Jul 17, 2014
Licensed content publisher	Elsevier
Licensed content publication	Thin Solid Films
Licensed content title	Fabrication of epitaxial zirconia and ceria thin films with arbitrary dopant and host atom composition
Licensed content author	Jun Jiang,Weida Shen,Joshua L. Hertz
Licensed content date	1 November 2012
Licensed content volume number	522
Licensed content issue number	None
Number of pages	5
Start Page	66
End Page	70
Type of Use	reuse in a thesis/dissertation
Intended publisher of new work	other
Portion	figures/tables/illustrations
Number of figures/tables/illustrations	2
Format	both print and electronic
Are you the author of this Elsevier article?	Yes
Will you be translating?	No
Title of your thesis/dissertation	STRAIN EFFECTS ON ION CONDUCTION IN HETEROGENEOUS OXIDE ELECTROLYTES
Expected completion date	Aug 2014
Estimated size (number of pages)	119
Elsevier VAT number	GB 494 6272 12
Permissions price	0.00 USD
VAT/Local Sales Tax	0.00 USD / 0.00 GBP
Total	0.00 USD
Terms and Conditions	

Figure 16

ROYAL SOCIETY OF CHEMISTRY
LICENSE
TERMS AND CONDITIONS
Jul 17, 2014

This is a License Agreement between Weida Shen ("You") and Royal Society of Chemistry ("Royal Society of Chemistry") provided by Copyright Clearance Center ("CCC"). The license consists of your order details, the terms and conditions provided by Royal Society of Chemistry, and the payment terms and conditions.

All payments must be made in full to CCC. For payment instructions, please see information listed at the bottom of this form.

License Number	3431450729381
License date	Jul 17, 2014
Licensed content publisher	Royal Society of Chemistry
Licensed content publication	Physical Chemistry Chemical Physics
Licensed content title	Micro-ionics: next generation power sources
Licensed content author	Harry L. Tuller,Scott J. Litzelman,WooChul Jung
Licensed content date	Mar 25, 2009
Volume number	11
Issue number	17
Type of Use	Thesis/Dissertation
Requestor type	academic/educational
Portion	figures/tables/images
Number of figures/tables/images	1
Format	print and electronic
Distribution quantity	10
Will you be translating?	no
Order reference number	None
Title of the thesis/dissertation	STRAIN EFFECTS ON ION CONDUCTION IN HETEROGENEOUS OXIDE ELECTROLYTES
Expected completion date	Aug 2014
Estimated size	119
Total	0.00 USD
Terms and Conditions	